Diss. ETH no. 26482

Effects of oxidation on the spin-orbit torques and skyrmionic textures in ultrathin Pt/Co/AlO_x heterostructures

A thesis submitted to attain the degree of
Doctor of Sciences ETH Zurich
(Dr. sc. ETH Zurich)

presented by
Junxiao Feng
M.Sc. Materials Science, Shandong University
Born on August 10th, 1988
Citizen of China

accepted on the recommendation of

Prof. Dr. Pietro Gambardella (ETH Zurich), examiner
Dr. Gilles Gaudin (SPINTEC), co-examiner
Prof. Dr. Laura Heyderman (ETH Zurich, Paul Scherrer Institute), co-examiner

2019

Abstract

Reading and writing digital information can be performed in a faster and more energy-efficient compared to present-day computer memories. Spintronics, by exploiting the spin degree of freedom to carry and store information, offers multiple approaches to this problem. One promising application under development is to use spin-orbit torques (SOTs) in magnetic random access memories (MRAMs) for controlling the magnetic state of the memory units. Recently, these torques have emerged as a powerful tool for switching the magnetization of perpendicular magnetized layers, owing to very low error rates and fast dynamics, opening the possibility to either improve or complement the performance of MRAMs operated by spin-transfer torques. Moreover, topologically non-trivial domain textures, such as chiral domain walls and skyrmions, can be manipulated by SOTs and are promising candidates for the development of racetrack memories. In such devices, the information is encoded in nanoscale domain walls or skrymionic textures, which can be driven by current pulses at low current-density.

Study of the oxidation effects of the magnetic heterostructures is interesting from both a fundamental and an applied perspective as it strongly influences the properties of the magnetic layers employed in spintronic devices. Recent studies have shown that oxidation effects can influence the magnetic properties, such as magnetic anisotropy, Dzyaloshinskii-Moriya interaction, SOTs, current-induced switching and domain textures. Therefore, in this thesis, we explore the oxidation effects on SOTs and skyrmionic textures in ultrathin Pt/Co/AlO_x heterostructures.

First, we study the effect of oxidation on the structural, electrical, and magnetic properties of Pt/Co/AlO_x, Pt/CoO_x/Co/AlO_x, and PtO_x/Co/AlO_x layers. We show how the saturation magnetization, perpendicular magnetic anisotropy, and anomalous Hall resistance are systematically affected by the degree of oxidation of both the Pt/Co and Co/Al interfaces. Further, we study the effect of oxidation on the SOT efficiency, namely the conversion ratio between the spin current absorbed by Co and the charge current that generates it. Oxidation of the Co/Al interface results in a 21% and 42% variation of the damping-like and field-like SOT efficiencies, which peak at 0.14 and 0.07, respectively. The insertion of a paramagnetic CoO_x layer between Pt and Co maintains a very strong perpendicular magnetic anisotropy and improves the damping-like and field-like SOT efficiencies, up to 0.26 and 0.20, respectively. In contrast with recent re-

ports, we do not find that the oxidation of Pt leads to a significant enhancement of the torques. Rather, we find that oxygen migrates from Pt to the Co and Al layers, leading to a time-dependent oxidation profile and an effective spin Hall conductivity that decreases with increasing oxygen concentration. Finally, we study current-induced switching in $Pt/Co/AlO_x$ with different degrees of oxidation and find a linear relationship between the critical switching current and the effective magnetic anisotropy controlled by the oxidation of Al. These results highlight the importance of interfaces and oxidation effects on the spin-orbit torques and magnetotransport properties of heavy metal/ferromagnet/oxide trilayers, and provide information on how to improve the SOT and magnetic switching characteristics of these systems.

Second, we investigate the domain textures of the $Pt/Co/AlO_x$ heterostructure at room temperature determined by different degrees of oxidation of the Co/Al interface. We study the magnetic field-induced domain nucleation and propagation of overoxidized, optimized and underoxidized $Pt/Co/AlO_x$. Underoxidized $Pt/Co/AlO_x$ supports the formation of skyrmion bubbles at zero field. We find that the strong pinning and disorder effects heavily influence the skyrmions and their dynamics. In the presence of strong pinning, skyrmion bubbles driven by SOTs elongate while remaining pinned at one side. We investigate the directional expansion of the bubbles in analogy with the skyrmion Hall effect and show that it strongly depends on current density, pulse width and out-of-plane field. Moreover, by reversing the current polarity, we find that the expansion and pinning of the skyrmion bubbles invert their position with respect to the bubble axis. This effect is attributed to the dependence of the SOT on the direction of the internal domain wall magnetization, which results in asymmetric forces on opposite sides of a bubble. Lastly, we show that repeated current pulsing of underoxidized $Pt/Co/AlO_x$, leads to a demagnetized state rather than a fully saturated magnetic state.These results shed light on the oxidation effects on the domain textures as well as the current-induced skyrmion dynamics in the presence of strong pinning in ultrathin heterostructures.

Zusammenfassung

Das Lesen und Schreiben digitaler Information könnte schneller und energieeffizienter durchgeführt werden, als es in momentan herkömmlichen Computerspeichern geschieht. Das Gebiet der Spintronik nutzt den Spin-Freiheitsgrad, um Informationen zu transportieren und zu speichern und bietet so verschiedene Ansätze zur Verbesserung von Datenspeichern. Eine vielversprechende Anwendung findet sich in der Entwicklung von magnetischen Arbeitsspeichern, wobei sogenannte Spin-Bahn-Drehmomente (spin-orbit torques, SOTs) zur Kontrolle des magnetischen Zustands der Speicherzellen verwendet werden. In den vergangenen Jahren sind diese SOTs als nützliches Instrument zur Schaltung von senkrecht magnetisierten Dünnfilmen in Erscheinung getreten. Vor allem die sehr kleine Schreib- und Lesefehlerrate und schnelle Dynamik des Schaltens würde eine starke Verbesserung bestehender magnetischer Arbeitsspeicher auf Basis von Spin-Transfer Drehmomenten ermöglichen. Des Weiteren können nicht-triviale Domänentexturen, wie etwa chirale Domänenwände oder Skyrmionen, mit SOTs manipuliert werden und sind somit ideale Systeme für die Entwicklung von Racetrack-Speichern. In den genannten Probensystemen wird die zu speichernde und übertragende Information in im Nanobereich liegenden Domänenwänden und Skyrmionentexturen gespeichert, welche dann mit Strompulsen bei sehr kleinen Stromdichten bewegt werden können.

Die Erforschung von Oxidationseffekten auf magnetische Heterostrukturen ist von grossem theoretischem sowie praktischem Interesse, da die Oxidation der Dünnfilme direkt die magnetischen Eigenschaften beeinflusst. Die aktuelle Literatur vermochte die Tragweite der Änderung von Eigenschaften aufzeigen. Unter anderem werden die magnetische Anisotropie, die Dzyaloshinskii-Moriya Wechselwirkung, SOTs, Strom-induzierte Schaltung sowie die Domänentextur direkt beeinflusst. In dieser Doktorarbeit untersuchen wir den Einfluss von Oxidation auf SOTs und Skyrmion-Texturen in ultradünnen $Pt/Co/AlO_x$ Heterostrukturen.

Im ersten Teil untersuchen wir den Effekt der Oxidation auf die strukturellen, elektrischen und magnetischen Eigenschaften von $Pt/Co/AlO_x$, $Pt/CoO_x/Co/AlO_x$, und $PtO_x/Co/AlO_x$ Schichtsystemen. Wir zeigen, wie die Sättigungsmagnetisierung, die senkrechte magnetische Anisotropie und der anomale Hallwiderstand systematisch durch die Oxidation der Grenzflächen zwischen Pt/Co sowie Co/Al geändert werden. Die SOT Effizienz, gegeben als das Verhältnis zwischen ab-

sorbiertem Spin-Strom in der Co-Schicht zum angelegten Ladungsstrom, wird untersucht. Wir finden, dass die Oxidation der Co/Al Grenzfläche zu einer Variation von 21% und 42% der gedämpften sowie feld-ähnlichen SOTs führt, wobei die Effizienz ein Maximum von 0.14 und 0.07 für die jeweiligen Drehmomente erreicht. Durch das Einfügen einer paramagnetischen CoO_x Schicht zwischen Pt und Co kann die Effizienz auf 0.26 respektive 0.20 erhöht werden, wobei eine sehr starke senkrechte magnetische Anisotropie beibehalten wird. Im Gegensatz zu kürzlich veröffentlichten Publikationen finden wir keine signifikante Steigerung der Drehmomente durch die Oxidation von Pt. Vielmehr sehen wir, dass Sauerstoff von Pt zu den Co und Al Schichten migriert, was zu einem zeitabhängigen Oxidationsprofil führt, was die effektive Spin-Hall Leitfähigkeit mit erhöhter Sauerstoffkonzentration senkt. Schliesslich untersuchen wir das strominduzierte Schalten in $Pt/Co/AlO_x$ Strukturen, die unterschiedlich stark oxidiert wurden. Wir finden eine lineare Abhängigkeit zwischen dem kritischen Schaltstrom und der effektiven magnetischen Anisotropie, welche durch die Oxidation von Al kontrolliert wird. Diese Ergebnisse unterstreichen die Wichtigkeit von Grenzflächen und Oxidationseffekten auf SOTs und magnetische Transporteigenschaften von Schwermetall/Ferromagnet/Oxid Dreifachschichten und bilden die Informationsgrundlage zur Verbesserung von SOT Charakteristika und magnetischen Schalteigenschaften der untersuchten Systeme.

Im zweiten Teil untersuchen wir die Domänentexturen von $Pt/Co/AlO_x$ Heterostrukturen bei Raumtemperatur, welche durch unterschiedliche Stärke der Oxidation der Co/Al Grenzfläche variiert werden können. Wir legen speziellen Fokus auf die magnetfeldinduzierte Domänen-Nukleation und anschliessende Ausbreitung von überoxidierten, optimierten und unteroxidierten $Pt/Co/AlO_x$ Schichtsystemen. Unteroxidiertes $Pt/Co/AlO_x$ unterstützt die Bildung von Skyrmionblasen ohne externes Magnetfeld. Die Skyrmionen und deren Dynamik werden stark durch Verankerungs- und Unordnungseffekte beeinflusst. Beim Vorhandensein von Verankerungseffekten dehnen sich Skyrmionblasen beim Anlegen von Strompulsen auf Grund von SOTs aus, während die Blasen am Defekt haften bleiben. Die Untersuchung der Richtungsabhängigkeit dieser Ausdehnung ergibt, dass diese stark von der Stromstärke, der Pulslänge und dem Feld senkrecht zur Probenebene abhängt, was wir in Analogie zum Skyrmion Hall Effekt erörtern. Die Umkehrung der Stromrichtung zeigt des Weiteren, dass die Ausdehnung sowie die Verankerung der Skyrmionenblasen ihre Position im Bezug auf die Blasenachse invertieren. Wir erklären dieses Verhalten mit der Abhängigkeit der SOTs auf die Richtung der internen Domänenwandmagnetisierung, was zu asym-

metrischen Kräften auf die Domänenwände auf gegenüberliegenden Seiten der Blase führt. Durch wiederholtes Pulsen von unteroxidiertem $Pt/Co/AlO_x$ wird dieses demagnetisiert, was im Kontrast zur Erwartung steht, dass dieses komplett saturieren sollte. Die untersuchten Strukturen führen zu einem besseren Verständnis der Oxidation von Domänentexturen sowie der strominduzierten Skyrmionendynamik in ultradünnen Heterostrukturen, welche starke Verankerungseffekte der Domänenwände aufzeigen.

Acknowledgements

I have spent the best four years of my life until now in ETH Zurich, most importantly due to the lovely people I met here. Firstly, I would like to thank *Prof. Dr. Pietro Gambardella* for the precious opportunity to join the Group of Magnetism and Interface Physics for my PhD studies. I always feel so lucky that I could obtain the chance to have such a great supervisor in ETH, not only due to his professionalism in science exploration and academic supervision, but also his nice personality and enthusiasm.

Furthermore, I thank *Prof. Dr. Laura Heyderman*, *Dr. Gilles Gaudin* and *Prof. Dr. Jan Vermant* for agreeing to serve as co-examiners. I am grateful to *Mihai Gabureac*, who supported me in the sputtering laboratory work and clean room supervision at the beginning of my PhD studies. I regard *Eva Grimaldi* as my sister, she always gave me helpful advice in both my academic and daily life. I enjoy every discussion with *Can Avci* and *Saul Velez*, they are quite talented and helpful to give me their priceless suggestions. I also want to thank my colleagues in the Room HPP N25, *Johannes, Manuel, Phonsi, Christoph, Toni, Giacomo, Gunasheel, Viola*, whenever I have questions, I just immediately ask and they always explain me with patience in a very friendly way. Besides, I also want to thank my former and current group members *Rina, Santos, Christian, Kevin, Abhijit, Corneliu, Luca, Martin, Federico, Benjamin, Ales and Charles* as well as the STM group members *Sebastian, Tom, Wei and Stepan* for the amazing working atmosphere. I also need to thank *Prof. Dr. Hans J. Hug* and *Yaoxuan* for the very professional cooperation.

Finally, I want to express my sincere gratitude to my family, without their support, I can not take the challenge to study abroad. I also want to thank my Chinese friends in ETH Zurich, especially *Teng, Haijian, Jianhua, Zhaochu, Jizhai, Yang and Lei*. Thank you for sharing some challenges of a growing up scientific researcher and for making the time at ETH a period that I will gladly remember.

Thanks! Danke! Grazie! Merci!

Junxiao Feng
Zurich, autumn 2019

Contents

List of abbreviations

AFM	atomic force microscopy
AHE	anomalous Hall effect
AMR	anisotropic magnetoresistance
DL	damping-like (torque)
DMI	Dzyaloshinskii-Moriya interaction
DW	domain wall
EBSD	electron back scatter diffraction
FL	field-like (torque)
FM	ferromagnet(ic)
FMR	ferromagnetic resonance
GMR	giant magnetoresistance
HM	heavy metal
IMA	in-plane magnetic anisotropy
IP	in-plane
O_x	metal oxide
MFM	magnetic force microscopy
MOKE	magneto-optic Kerr effect microscopy
MRAM	magnetic random-access memory
MTJ	magnetic tunnel junction
NM	non-magnetic (metal)
OOP	out-of-plane
PEEM	photoemission electron microscopy
PHE	planar Hall effect
PMA	perpendicular magnetic anisotropy
RMS	root mean square
SOC	spin-orbit coupling
SOT	spin-orbit torque
SQUID	superconducting quantum interference device
STT	spin-transfer torque
STXM	scanning transmission x-ray microscopy
TKD	transmission Kikuchi diffraction
TMR	tunneling magnetoresistance
XPS	x-ray photoemission microscopy

1 Introduction

Over the past 60 years, semiconductor chips have become smaller, cheaper, and more powerful. However, Moore's law comes to the end. Reducing the size of devices to enhance the system performance is not a valid strategy any more as the size of the devices is approaching the atomic limit. Therefore, more-than-Moore approaches are being actively pursued in order to augment the performances of microelectronic devices. The discovery of the tunneling magnetoresistance (TMR) by Michel Julliere[1] in 1975, and the giant magnetoresistance (GMR) effect by Peter Grünberg[2,3] and Albert Fert[4] in 1988 opened the door to spintronics, a new field in which the spin degree of freedom is included in conventional charge-based microelectronic devices to complement charge with spin functionalities[5–7]. Spintronics has several advantages over conventional electronics. For example, spintronics is non-volatile, offering a strong reduction of the power consumption relative to volatile memories, and holds great promise for logic devices[7].

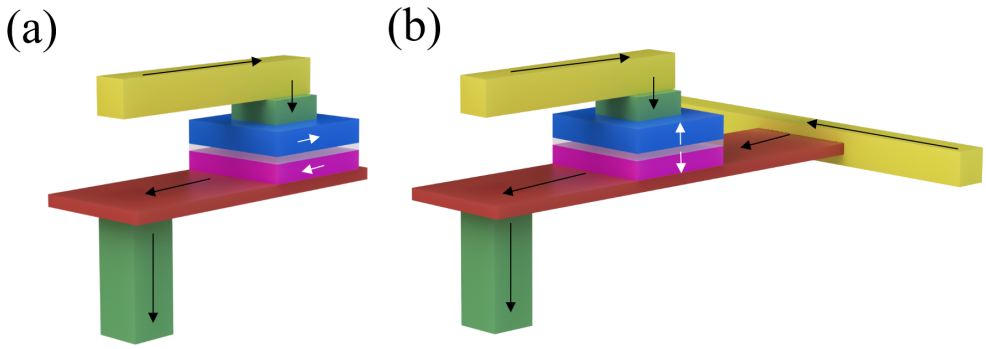

Figure 1.1 | (a) STT-MRAMs and (b) SOT-MRAMs device configurations. The blue layer is the magnetic fixed layer, the white one is the insulating layer, the layer in purple is the magnetic free layer. The white arrows indicate the magnetization directions, the black ones show the direction of the current. Figures adapted from Ref. 8.

Magnetic random access memories (MRAMs) based on magnetic tunnel junctions (MTJs)[9] are promising candidates for data storage due to their nonvolatility, high endurance, and low energy consumption[7,10]. An MTJ consists of two ferromagnetic layers separated by a thin insulating layer. Passing a current through an MTJ results in the TMR, which depends on the relative orientation between the ferromagnetic layers. This effect can be used to encode information

in digital computing. The TMR of an MTJ is low (high) when the magnetizations of these two magnetic layers are parallel (antiparallel) to each other, which correspond to 1 (0) as memory bits. Further, when injecting current into an MTJ, spin angular momentum is transferred from the reference magnetic layer, which is fixed by coupling to an additional antiferromagnetic layer, to the free magnetic layer, which allows themodification of the magnetization of the free layer. This is called spin transfer torque (STT)[10–13].

MRAMs based on the STT writing mechanism provides great advantages in scalability and integration[14]. However, STT-MRAMs (Fig. 1.1) have some disadvantages that are difficult to overcome. For instance, in order to have larger STT switching efficiencies, a thinner tunnel barrier is preferred as more spin angular momentum can be transferred through it. However, a thinner tunnel barrier leads to a smaller TMR, thus making more difficult to read the magnetization state. Therefore, as the reading and writing current share the same path, it is difficult to balance these two factors. Moreover, for the STT reversal process, a large current density needs to be applied to thermally activate the switching process, which may damage the tunnel barrier

The recently discovered spin-orbit torques (SOT) enabled MRAMs with a different geometry and writing mechanism [Fig. 1.1 (b)]. SOTs might open a new path to the operation of MRAMs[15] as the fast-switching can be accomplished, no current goes through the tunnel barrier, and reading and writing lines are separated [Fig. 1.1(b)]. SOTs resulting from charge current have been observed recently by Miron et al.[16,17] in ferromagnets (FM) lacking structural inversion symmetry[18]. SOTs have emerged as a powerful tool to switch the magnetization in the heavy metal/ferromagnet/oxide (HM/FM/O_x) trilayers with structural inversion asymmetry. These systems are considered to be very useful in spintronics[9,10,15,17–19] due to the perpendicular magnetic anisotropy (PMA) and high Curie temperature afforded by HM/FM/O_x stacks, such as Pt/Co/AlO_x [Figure 1.2(a)] and Ta/CoFeB/MgO[17–21].[7,22].

The mechanisms upon which the SOTs rely are charge-to-spin conversion due to the spin Hall effect (SHE) from the bulk of a heavy metal or the Rashba-type interfacial effect, which allows generating a non-equilibrium spin accumulation near the FM interfaces[24], which then transfers spin angular momentum onto the local magnetization of the ferromagnet due to the s-d exchange interaction. Spin-orbit coupling is the interaction between the spins and the magnetic field generated by the electron orbital motion and vice versa. This interaction makes the spin degree of freedom respond to its orbital environment[25]. When injecting

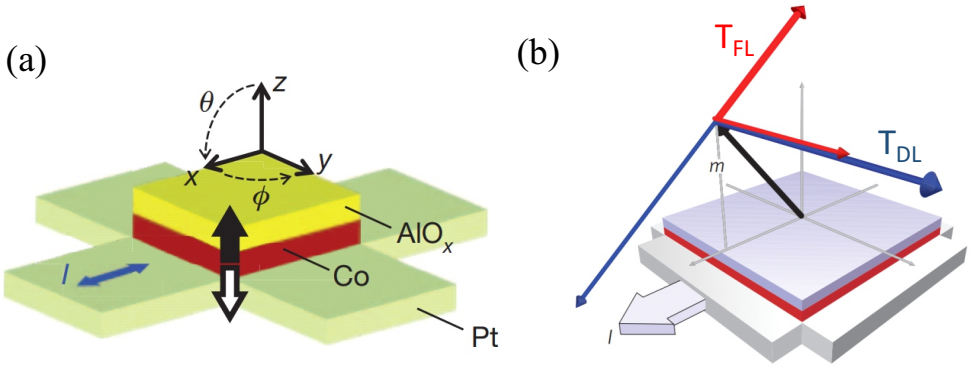

Figure 1.2 | (a) Ultrathin Pt/Co/AlO$_x$ heterostructure with perpendicular magnetic anisotropy. (b) Schematics of SOT, thick blue arrow indicates the DL torque and thick red for the FL torque. Figures adapted from Refs. 17, 23.

a charge current through a heavy metal, due to spin-orbit coupling, electrons with opposite spin scatter in opposite directions, thus generating a spin current and spin accumulation at the surfaces of the heavy metal. This effect is called the spin Hall effect. The Rashba effect refers to the phenomenon in which a spin current is generated at the interface of the heterostructures due to the presence of an electric field, which can be intrinsic to the material or extrinsic[18,26]. These two sources of spin accumulation allow for two types of torques by symmetry, namely the damping-like (DL) and field-like (FL) SOTs (Fig. 1.2). Despite extensive efforts, the relative contributions of the above mentioned bulk and interface-induced effects on the SOTs remain elusive[17–20,23,27,28].

Oxide layers play a two-fold role in HM/FM/O$_x$ trilayers. Apart from being often used as tunnel and gate barriers, they can also induce PMA. The role of interface oxidation of the ferromagnetic layer on different properties such as the PMA and the saturation magnetization has been extensively investigated in the past years [Fig. 1.3(a)][29–34]. Recently, the focus has shifted towards using oxidation as a tool for modifying not only the anisotropy but also the SOTs, their magnitudes and switching characteristics by either engineering the oxidation during layer growth or post-growth dynamic modification by applying a gate voltage [Fig. 1.3(b) and (c)][35–47]. However, the role of the oxidation on SOTs is still not fully clear. All these studies are focused on one specific aspect of the oxidation, either the FM/O$_x$ interface or the HM layer, whereas a systematic investigation of the effect of oxidation on both interfaces of the same system has not been reported yet.

Additionally, it has been found that oxidation can tune the Dzyaloshinskii-

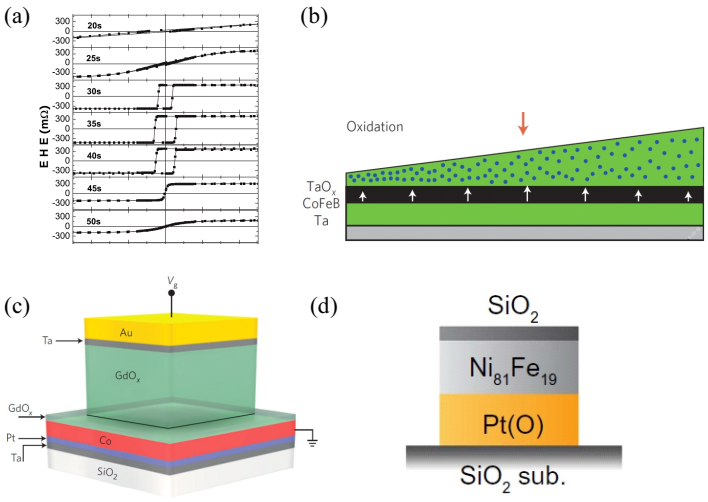

Figure 1.3 | (a) Change the magnetization of a magnetic layer in a heterostructure by tuning the oxidation time (extraordinary Hall resistance versus out-of-plane magnetic field). (b) Non-uniform oxidation through a Ta wedge layer. (c) Gating voltage control in a heterostructure. Oxygen moves in between the oxide and magnetic layer by reversing the gating voltage. (d) Trilayer with oxidized Pt for which a strong enhancement of the SOT efficiency has been claimed. Figures adapted from Refs. 32, 36, 38, 46.

Moriya interaction (DMI)[48,49], which is responsible for the formation of chiral magnetic textures, such as Néel chiral walls, spin spirals, and skyrmions. Magnetic skyrmions named after the British physicist Skyrme, are topologically protected chiral spin textures with a continuous swirling spin configuration[50,51]. Skyrmions [Fig. 1.4(a)] can be manipulated by SOTs and are promising candidates for the development of a racetrack memory [Fig. 1.4(b)] and logic devices[52–54]. Magnetic bubble domains are intrinsically unstable and only arise due to dipolar fields and the tension of ordinary domain walls as an effect of the shape of a magnetized body[55,56]. Contrary to bubble domains, magnetic skyrmions may exist even in very high fields forming extremely small spin textures, which are stabilized against collapse by the DMI. In skyrmion-based memories, the information is encoded in ultra-small topologically protected skrymion textures, which can be driven by current pulses of relatively low current-density, allowing for the development of high-density storage and low-power memory devices.

Skyrmions or skyrmion bubbles can be imaged and detected by means of the magneto-optic Kerr microscopy (MOKE), magnetic force microscopy (MFM), scanning NV center magnetometry, photoemission electron microscopy (PEEM), scanning transmission x-ray microscopy (STXM) and Hall resistance methods[57–66].

Recently, skyrmion nucleation, annihilation and dynamics have been studied under current pulses or external field[54,58,60–62,66–69]. Additionally, the skyrmion Hall effect has emerged as an interesting phenomenon, in which transport and topology effects appear to be linked to each other[57–60,62,66,69–73].

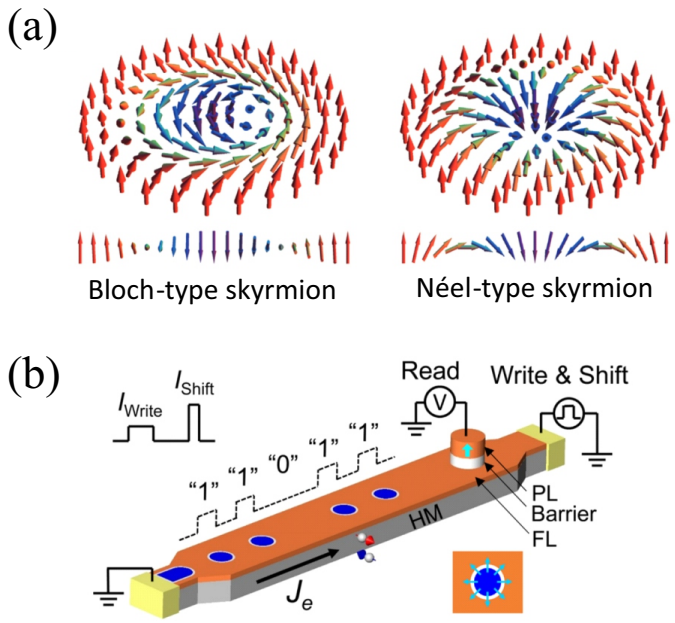

Figure 1.4 | (a) Spin configurations of the Bloch-type and Néel-type skyrmions. The cross-sections of both skyrmions are depicted underneath. (b) Schematics of the skyrmion racetrack memory. Skyrmions are injected by applying a write current I_{write} and driven along the racetrack by the shift current I_{shift}. An MTJ could be used to read the signal when skyrmions pass underneath the MTJ. A typical MTJ consists magnetic pinned layer (PL), insulating barrier and magnetic free layer (FL). Figures adapted from Refs. 54, 74.

Pinning and disorder have recently been identified as one of the key ingredients that determine the skyrmion dynamics. Initially pinning was considered to be negligible for skyrmions, as simulations showed that skyrmions may avoid pinning sites easily[51]. However, recent experiments and simulations showed that skyrmions can be generated or annihilated at pinning sites, while their motion is distorted or even completely blocked by pinning[61,66,69,73,75], making the exploration of pinning effects important for controlling skyrmions motion in electronic devices. The study of the effect of tuning the oxidation of HM/FM/O_x trilayers for skyrmion stabilization and dynamics in the presence of strong pinning has not been reported in detail so far.

In this thesis, we present two studies:

- In the first part, we present a systematic study of the oxidation effects on the magnetic and SOTs properties of $Pt/Co/AlO_x$ heterostructures.
- In the second part, we study the role of oxidation on the skyrmion formation and dynamics with strong pinning.

This thesis is organized as follows. In Chapter 2, I summarize the relevant magnetic interactions and give basic information on SOTs, magnetic domain walls, and skyrmions. Sample fabrication details as well as the structural characterization are given in Chapter 3. In Chapter 4, I describe the experimental techniques employed for the characterization of SOT by the harmonic Hall voltage method and of the domain textures using a magnetic-optical Kerr effect microscope (MOKE) and high resolution MFM. Chapter 5 reports the systematic investigation of the oxidation effects on the electrical and magnetic properties of $Pt/Co/AlO_x$ heterostructures. The SOTs and current-induced switching properties are presented in Chapter 6. The domain texture properties as a function of oxidation, external magnetic field and current pulses are presented in Chapter 7. In Chapter 8, I present the current-induced motion properties of skyrmions in the presence of pinning, followed by the summary and outlook in Chapter 9.

2 Background

2.1 Basic magnetic interactions

In this section, I will introduce the basic magnetic interactions occurring in ferromagnetic materials that are relevant for understanding the effects studied in this thesis.

2.1.1 Exchange interaction

The following Hamiltonian describes the exchange interaction between two neighbouring spins in a magnetic material, which results from the Pauli principle and Coulomb interaction:

$$\hat{\mathcal{H}}_{ex} = -\sum_{ij} J_{ij} \mathbf{S}_i \cdot \mathbf{S}_j, \tag{2.1}$$

here, J_{ij} is a constant quantifying the exchange interaction between the i^{th} ($\mathbf{S}_i$) and j^{th} ($\mathbf{S}_j$) spins. For ferromagnetic materials the exchange constant $J_{ij} > 0$, favouring the parallel alignment of the adjacent spins. For ferrimagnetic and antiferromagnetic materials, the constant is negative, meaning the antiparallel alignment is preferred.

2.1.2 Dzyaloshinskii-Moriya interaction

The normal exchange interaction described above favors the alignment of two adjacent spins (anti)parallel to each other. The DMI, on the other hand, is the antisymmetric counterpart of the exchange interaction, which favours a perpendicular configuration for adjacent spins. The Hamiltonian that describes the DMI interaction can be written as follows[76]:

$$\hat{\mathcal{H}}_{DMI} = \sum_{ij} \mathbf{D}_{ij} \cdot \mathbf{S}_i \times \mathbf{S}_j. \tag{2.2}$$

where $\mathbf{D}_{ij} = D(\mathbf{z} \times \mathbf{u}_{ij})$ is the DMI vector. D is the DMI strength factor, $\mathbf{z}$ is the unit vector pointing along z axis (out-of-plane), and $\mathbf{u_{ij}}$ is the vector connecting the two spins.

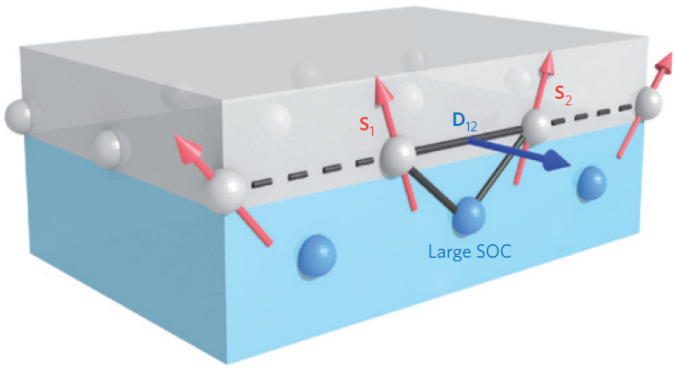

Figure 2.1 | Schematic diagram representing the DMI interaction of a classical HM/FM system. The large spin-orbit coupling mediates the DMI from HM. $\mathbf{S}_1$ and $\mathbf{S}_2$ represent two adjacent spins and D_{12} is the DMI vector associated to those two spins. Figure adapted from Ref. 51.

The strength of the DMI to the first approximation is linked to the strength of spin-orbit coupling (SOC), therefore, large DMI is typically found in materials and heterostructures involving heavy elements, in which the strength of SOC is enhanced. Compared with the exchange interaction, the strength of the DMI field is orders of magnitude smaller, ranging from hundreds (Ta based) to thousands (Pt based) of Oersted[77]. Unlike the bulk DMI in the noncentrosymmetric crystal structures, the interfacial DMI arises from the structural inversion asymmetry (Fig. 2.1). Interface engineering has been developed for introducing chiral structures in heterostructures. Strong DMI has been observed in heterostructures such as Pt/Co and Pt/CoFeB[58,69,78–80]due to the symmetry breaking at the interface and the strong SOC from the HM. The DMI can be manipulated to stabilize domain textures, such as chiral magnetic domain walls and magnetic skyrmions in magnetic ultra thin multilayers[81].

2.1.3 Zeeman energy

The energy density of a magnetic material upon applying the external field is given by the Zeeman energy equation:

$$E_{\mathrm{Z}} = -\mathbf{M} \cdot \mathbf{B}_{\mathrm{ext}}, \tag{2.3}$$

Here, $\mathbf{M}$ is the magnetization, $\mathbf{B}_{\mathrm{ext}}$ is the external field. Based on Eq. 2.3, we can easily tell that, when $\mathbf{M}$ is parallel to $\mathbf{B}_{\mathrm{ext}}$, E_{Z} is minimized, which means that the magnetization always prefers to align with the field direction. In order

to understand the motion of the magnetization, we can regard the effects of the external field as a magnetic torque (Zeeman torque) acting on the magnetization ($\mathbf{T}_Z = \mathbf{M} \times \mathbf{B}_{\text{ext}}$), which tries to push the magnetization towards the direction of the external field.

2.1.4 Magnetic anisotropy

Magnetic anisotropy means that the ferromagnetic or antiferromagnetic axis of a sample prefers to be along some fixed direction(s) [82]. There are two main sources for magnetic anisotropy: dipolar interactions and magnetocrystalline anisotropy. The effective magnetic anisotropy field $B_{\text{K}}^{\text{eff}}$ is the net effective field considering both sources. We can use $B_{\text{K}}^{\text{eff}}$ to describe the energy which tries to push the magnetization towards the energy-favorable easy-axis. $B_{\text{K}}^{\text{eff}}$ consists of the demagnetizing field B_{dem} and anisotropy field B_{K} including the magnetocrystalline anisotropy, interface anisotropy and induced anisotropy.

Demagnetizing field

The demagnetizing field comes from the uncompensated surface magnetic charges due to the discontinuity in the magnetization. These magnetic charges produce a stray field outside the magnet, and a demagnetizing field which opposites the magnetization. Based on the Ampere-Maxwell's law, we call the magnetic field which is related to the B_{dem} but outside the magnet as the stray or dipolar field. Both of these fields result in energy terms which are associated with the sample shape, therefore we call the effect of the associated B_{dem} shape anisotropy as well. For an ellipsoidal ferromagnet whose magnetization is uniform and $\mathbf{M}$ is along one of the principal axes, B_{dem} can be simply written as:

$$B_{\text{dem}} = -\mu_0 N \mathbf{M} = \mu_0 \begin{pmatrix} N_{\text{xx}} & 0 & 0 \\ 0 & N_{\text{yy}} & 0 \\ 0 & 0 & N_{\text{zz}} \end{pmatrix} \mathbf{M}. \tag{2.4}$$

Here μ_0 is the permeability of free space, N is the demagnetizing tensor with $N_{\text{xx}}+N_{\text{yy}}+N_{\text{zz}} = 1$. For an ultrathin magnetic layer with infinite dimensions and normal z, $N_{\text{xx}} = N_{\text{yy}} = 0$, N_{zz}=1. If the magnetization of the layer is in-plane, B_{dem} is zero as the z axis magnetization component $M_{\text{z}} = 0$. To understand this more vividly, we can regard B_{dem} as an effective field which leads to an energetic saving for keeping the magnetization in the plane of the film.

Magnetocrystalline and interface anisotropies

In bcc Fe, the magnetic field needed to magnetize the Fe to saturation is smaller in the [100] direction than in the [111] direction, while the case is just the opposite in fcc Ni. These two totally different properties in Fe and Ni crystals are attributed to the magnetocrystalline anisotropy. Magnetocrystalline anisotropy arises as a result of the crystal structure, leading to a preferential set of directions along which the energy of the system is minimized and hence where the magnetization lies. For uniaxial materials, the magnetocrystalline anisotropy energy are written as follows:

$$E_{\mathrm{K}} = E_{\mathrm{K1}} \sin^2 \theta + E_{\mathrm{K2}} \sin^4 \theta + ... \tag{2.5}$$

$\mathrm{E_{K1}}$ and $\mathrm{E_{K2}}$ are the anisotropy constants and θ is the angle between the magnetization and the easy axis. As the constants are positive, $\mathrm{E_K}$ is minimized when $\theta = 0$. The physical origin of this anisotropy is mainly due to spin-orbit coupling and orbit-lattice coupling[83].

For hcp Co, the easy axis is in the [001] direction, the hard axis is in the [100] direction. While the magnetocrystalline anisotropy of the ultrathin Co layer is zero due to its polycrystalline structure.

Interface anisotropy arises due to structure symmetry breaking at the interface between two materials. At the interface, along the out-of-plane direction, the electronic wave functions are significantly modified by the presence of a different element, resulting in the interface anisotropy. As the physical origin of interface anisotropy is structural, it is often convenient to consider it as part of the magnetocrystalline anisotropy.

In ultra-thin $\mathrm{Pt/Co/AlO_x}$ layers, the easy axis is perpendicular to the sample plane, whereas, owing to the polycrystalline structure, there is no favoured in-plane direction. Thus, in our coordinate system, the easy axis is along z, whereas the xy plane is a hard plane. The PMA of $\mathrm{Pt/Co/AlO_x}$ is promoted by two effects: the first one is the strong interfacial hybridization between Co and Pt d-states, which leads to a weakening of the in-plane component of the orbital magnetic moment relative to the out-of-plane component. Through the spin-orbit interaction, the largest out-of-plane orbital moment determines the easy axis of the system. The second effect is a similar enhancement of the out-of-plane orbital moment due to the oxidation of the top Co interface. In this case, the axial Co-O ligand field lowers the energy of the d-states with out-of-plane orbital moment, leading to an additional contribution to the PMA.

In films which have an out-of-plane easy axis, the anisotropy that energetically favors the spins to be perpendicular to the plane of the film is called PMA. PMA is the interfacial effect due to the uniaxial magnetic anisotropy in Pt/Co layers and is enhanced by the oxidation of the Co layer[30,32].

Effective anisotropy

The effective anisotropy field (B_{K}) is the net anisotropy field after considering both B_{K} and B_{dem}. For the studied samples with uniaxial anisotropy in this thesis, the effective anisotropy field B_{K}^{eff} is given by

$$B_{\mathrm{K}}^{eff} = B_{\mathrm{K}} + B_{dem} = \frac{2K}{\mu_0 M} - \mu_0 N M. \tag{2.6}$$

B_{K} is the anisotropy field, K is the anisotropy constant, including the effects of the magnetocrystalline, interface and induced anisotropies. As a result, when the sample has PMA, $B_{\mathrm{K}}^{eff} > 0$, while for the sample with in-plane magnetic anisotropy (IMA), $B_{\mathrm{K}}^{eff} < 0$.

2.2 Spin-orbit torques

We can use the current-induced SOT to tilt or even switch the magnetization. In the following section I will introduce their origin, symmetry and switching properties.

2.2.1 Origin of SOTs

SOTs arise from the conversion of a charge current into a spin current, which is made possible by spin-orbit coupling. The flow directions of the charge and spin currents are orthogonal, which allows for injecting spins, and therefore angular momentum, into virtually any type of magnetic material placed next to a HM conductor. The interaction between the spin current and the local magnetization is then exemplified as a "spin torque". Generally speaking, two different effects are regarded as sources of the spin polarization. The bulk SHE [Fig. 2.2(a)] is usually considered as the origin of damping-like torque, whereas field-like torque is thought to originate from the interfacial Rashba-Edelstein effect [Fig. 2.2(b)]. However, both the damping-like torque and field-like torque can originate from either effect. These two torques are called SOTs as both of them result from the spin accumulation at the HM/FM interfaces due to the SOC. As different heavy

metals show different signs of the spin-orbit coupling, the signs of the SOTs are different as well.

The SHE relies on extrinsic and intrinsic spin-dependent scattering of electrons when electrical charge current passes through a material, leading to opposite spin polarization at opposite edges of the conductor[84–86], this spin polarization decays exponentially away from the edges as shown by Fig. 2.2 (a). The spin accumulation at the HM/FM interface then diffuses and is absorbed by the FM, inducing a torque on the magnetization with direction parallel to the spin polarization. Usually the large spin Hall effect is strong in HM, such as Pt, Ta and W, due to the strong spin-orbit of the HM elements coupling.

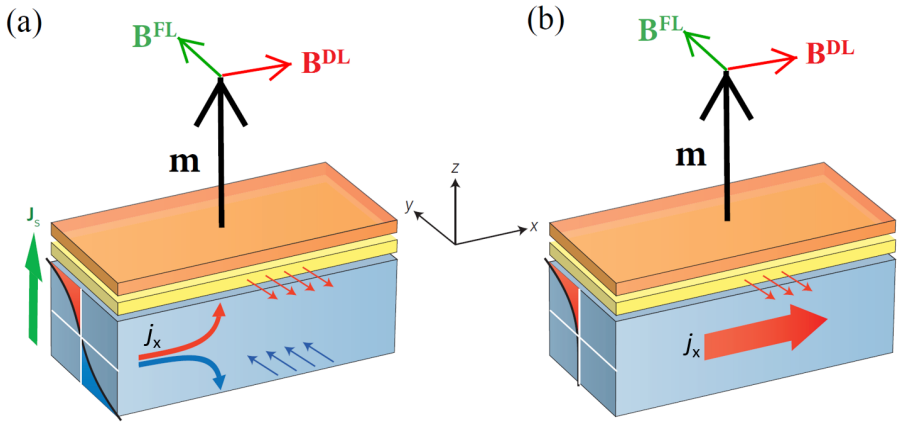

Figure 2.2 | (a) The spin current induced by the spin Hall effect in a magnetic bilayer (where the ferromagnet is shown in yellow, the heavy metal in blue and the capping layer in orange): the spin Hall effect separates flowing spins aligned parallel (blue arrows) and antiparallel (red arrows) to the transverse y axis, producing a spin current J_s (green arrow) flowing along z and polarized along the y axis. (b) When the inversion symmetry is broken at the interface between the ferromagnet and the heavy metal, the spin accumulation is created along the transverse direction due to the Rashba-Edelstein effect. The effective damping-like and field-like fields are shown in red and green, respectively. Figures adapted from Ref. 87.

Different from the SHE, the Rashba-Edelstein effect is a purely interfacial effect[26,88]. At the FM/HM interface, due to the structural symmetry breaking, the electronic configurations of FM/HM are different along the normal direction, leading to a nonzero electric field at the interface. Due to the Lorentz transformation, when electrons are moving with relativistic speed in this electric field, they experience an effective magnetic field. This effective magnetic field, which is perpendicular to both the electron motion and electric field directions

is called the Rashba-Edelstein field. The Rashba-Edelstein field induces a non-equilibrium spin accumulation at the interface as shown in Fig. 2.2(b)[87]. Similar to the SHE, this spin accumulation results in a torque as well.

Based on recent studies, the oxide layers between the HM and the FM interface[46,47], or on top of the FM[89] can be an additional source of SOT. Therefore in this thesis, we performed three systematic studies of the oxidation effects on the SOT properties of the Pt/Co/AlO_x heterostructures in order to clarify the sources of the SOTs.

2.2.2 Symmetries of SOTs

We define the current direction as the x axis, the transverse in-plane direction as the y axis, and the direction normal to surface as the z axis (Fig. 2.2). With current injection along x, spins polarize along y. To the lowest order in the unitary magnetization $\mathbf{m} = \mathbf{M}/M_s$, the SOTs are given by[7,23,23]:

$$\mathbf{T} = T^{DL}\mathbf{m} \times (\mathbf{m} \times \mathbf{y}) + T^{FL}\mathbf{m} \times \mathbf{y} \tag{2.7}$$

Here, $\mathbf{T}^{DL}$ is the damping-like torque, $\mathbf{T}^{FL}$ is the field-like torque, and $\mathbf{m}$ is the magnetization. In order to have a better understanding of SOTs, we usually define effective fields which are related to SOT to show how these torques act on the magnetization:

$$\mathbf{B}^{DL} = \mathbf{T}^{DL} \times \mathbf{m} = B^{DL}(\mathbf{m} \times \mathbf{y}), \tag{2.8}$$

$$\mathbf{B}^{FL} = \mathbf{T}^{FL} \times \mathbf{m} = B^{FL}\mathbf{y} \tag{2.9}$$

Here, $\mathbf{B}^{DL}$ is the damping-like effective field, and $\mathbf{B}^{FL}$ is the field-like effective field. The advantage of the effective field formulation is that their action on the magnetization can be directly measured and compared to that of an external field of known magnitude and direction, which allows for the quantification of B^{DL} and B^{FL} by means of a variety of techniques[7]. Here we measure B^{DL} and B^{FL} using the harmonic Hall voltage method[20,23,90,91], as described in the following section.

Based on Eq. 2.9, for both magnetic systems with in-plane and out-of-plane magnetization, $\mathbf{B}^{FL}$ is always along the y axis. For samples with PMA, when $\mathbf{m}$ is along the z axis, the damping-like effective field $\mathbf{B}^{DL}$ is along the x axis. The related schematic diagrams of these two effective fields are shown in Fig. 2.2.

2.2.3 Current-induced switching

Magnetic materials with large coercivity and strong perpendicular anisotropy are preferred as they are more stable and allow for high data storage density. However, writing the magnetic state becomes increasing difficult for such materials. Miron et al.[17] found that, injecting an in-plane current into HM/FM bilayers, with the help of an external in-plane magnetic field B_{ext}, the current-induced SOT can switch the magnetization of PMA samples with structural inversion asymmetry.

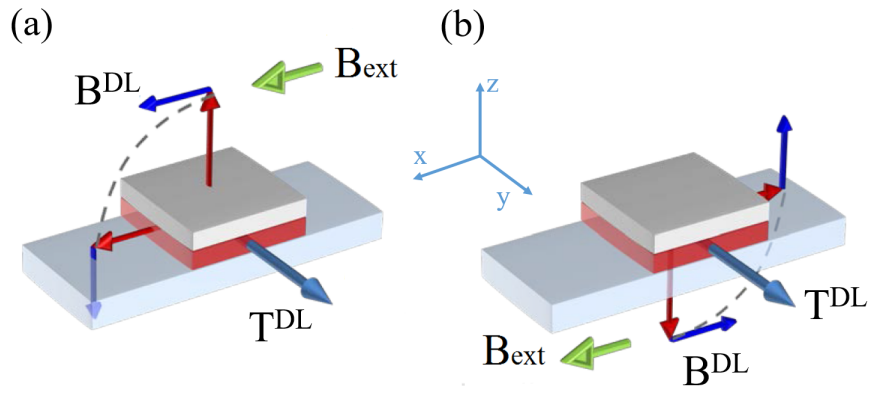

Figure 2.3 | (a) Nonequilibrium state with the magnetization up and (b) Equilibrium state with the magnetization down. B_{ext} is the external in-plane field which is along the current direction, B^{DL} and B^{FL} are the effective damping-like and field-like fields, respectively. Figures adapted from Ref. 92.

In the macrospin approximation, a single spin is used to describe the whole magnetic system as the magnetization is considered to be homogeneous. Under this approximation, $\mathbf{B}^{DL}$ leads to the rotation of the magnetization. Fig. 2.3 shows the schematic diagram of a PMA sample in the macrospin approximation. Suppose the initial magnetization to be up [Fig. 2.3(a)], with the injection of a positive current along +x axis, a $\mathbf{B}^{DL}$ is generated. This state is a nonequilibrium state as shown by Fig. 2.3 (a). With an external in-plane field ($\mathbf{B}_{\text{ext}}$) along the +x axis, if the $\mathbf{B}^{DL}$ is large enough, the magnetization will be switched from the +z down to the -z direction. At this moment, as $\mathbf{B}^{DL}$ is antisymmetric relative to the inversion of the magnetization, the direction of $\mathbf{B}^{DL}$ will be along the -x axis. Now the directions of $\mathbf{B}^{DL}$ and external in-plane field are antiparallel to each other, leading to a new equilibrium state of the magnetization shown by Fig. 2.3(b). The SOT switching properties, such as switching probability as a function of pulse amplitude, duration, and the related magnetization reversal

mechanism have been reported in previous work[17,19,80].

In a real magnetic system, the switching situation is more complicated compared to the macrospin picture presented above. In systems with dimensions exceeding the width of domain walls, magnetism reversal occurs via domain nucleation and propagation (more details will be given in Chapter 6)[80]. Therefore, in the next section, we are going to introduce the magnetic domain walls that separate the domains.

2.3 Domain walls

A magnetic domain wall (DW) defines the boundary between adjacent magnetic domains. The formation of magnetic domains results from the balance of the demagnetizing energy field and the energy cost associated with the DW. DWs can have different structures. For instance, in permalloy nanowires, three different DW structures have been identified as transverse, vortex and antivortex types[93]. In this section, we will describe two common DW types in systems with PMA, as well as the basic properties that define DWs. Lastly, we will present the dynamics of the DWs and their properties under magnetic field or current-induced SOTs.

2.3.1 Bloch and Néel domain walls

In magnetic systems with PMA, the two most common DW types are the Bloch and the Néel walls, which are classified according to the internal spin configuration and rotation when changing between adjacent domains. In a Bloch wall, the internal magnetization rotates in the plane parallel to the plane of the wall, while in a Néel wall, it rotates perpendicular to the plane. In addition, both types of DWs can be right- or left-handed, the energy minimization of the system defines the type of the DW (Fig. 2.4).

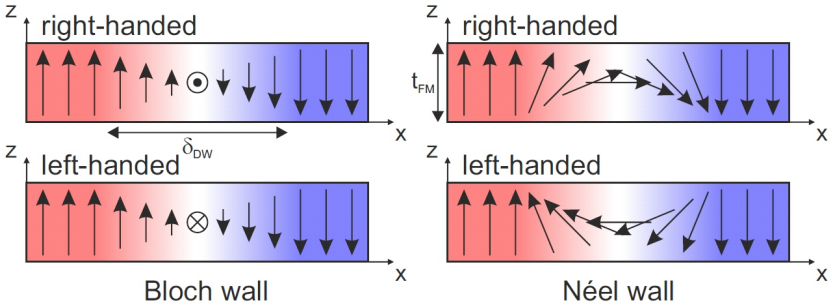

Figure 2.4 | Illustration of spin configurations of the right- and left-handed Bloch and Néel DWs. Figure adapted from Ref. 94.

We can also classify the different DWs according to the divergence of the magnetization, which can be written as $\nabla \cdot \mathbf{M} = \partial M_x/\partial x + \partial M_y/\partial y + \partial M_z/\partial z$. For a Bloch type wall,$\nabla \cdot \mathbf{M} = 0$ since $M_x = 0$ and the spins in the yz plane are parallel to each other. Therefore, a Bloch DW has no magnetic charge and no source of demagnetizing field in the wall. In a Néel type DW, as the magnetization rotates within the plane of the domain magnetization, the $\nabla \cdot \mathbf{M} \neq 0$, which results in finite stray field[82]. In thin films with out-of-plane anisotropy where the DMI is not present, the most stable magnetic DW configuration is the Bloch type. However, the DMI favors the formation of chiral Néel walls. For instance in Pt/Co/AlO_x trilayers, the DWs are the left-handed Néel type[95–97], which is determined by the balance of the DMI, exchange interaction, and anisotropy field.

2.3.2 Domain wall energy

In a ferromagnet, introducing a misalignment between adjacent spins costs energy as the exchange interaction energy between two neighbouring spins is -$\mathbf{JS_1 \cdot S_2}$ = -JS^2cosθ (Eq. 2.2). When $\theta \ll 1$, the total exchange energy in a Bloch wall where the spin rotates over N sites by an angle $\theta = \pi$/N is J$S^2\pi^2$/N. For a unit area wall with 1/a^2 spins (a is the lattice spacing), the total exchange energy is thus J$S^2\pi^2/a^2$N.

The anisotropy energy also contributes to the DW formation as the magnetization rotates inside the DW away from the easy axis direction, which costs energy. The related energy contribution per unit area of the wall can be written as NKa/2, where K is the anisotropy constant. Therefore, the DW energy per unit area can be written as follows considering both the exchange and anisotropy energy:

$$\sigma = JS^2 \frac{\pi^2}{\mathrm{a}^2 N} + \frac{NK\mathrm{a}}{2}. \tag{2.10}$$

The equilibrium DW configuration is given by $d\sigma/dN$=0, which leads to the following solution for N:

$$N = \pi S \sqrt{2J/K\mathrm{a}^3}. \tag{2.11}$$

The Bloch wall width is thus given by:

$$\Delta = Na = \pi S \sqrt{2J/K\mathrm{a}}. \tag{2.12}$$

Note that we can also write the DW width in the following form[83]:

$$\Delta = \sqrt{A/B_K^{eff}}, \tag{2.13}$$

where A is the micromagnetic exchange stiffness constant (related to J_{ij}). Therefore, a strong exchange interaction leads to a wider DW, whereas a stronger effective anisotropy field promotes a narrower DW. Note that the DMI will introduce chirality into the DW, but the DW width will mostly remain unchanged[98,99].

2.3.3 Magnetic field-driven domain wall motion

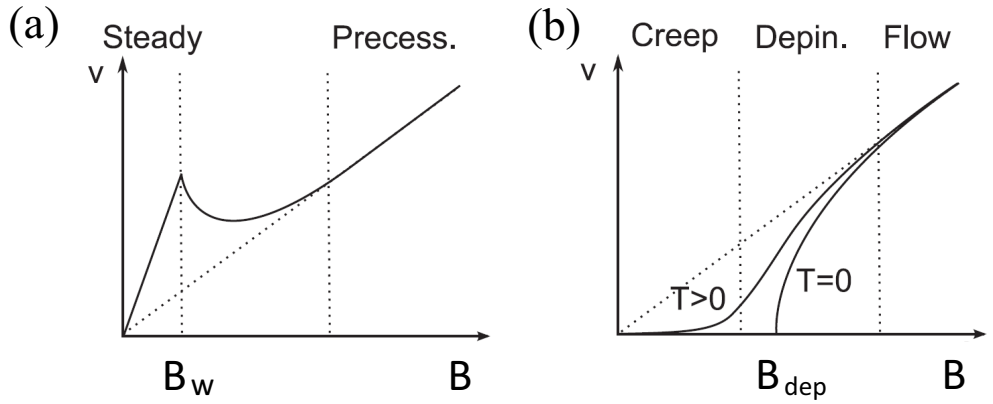

Figure 2.5 | (a) DW velocity as a function of the external magnetic field applied along easy axis in a film without defects. The Walker breakdown field (B_w) seperates the steady and precessional regimes[100]. (b) DW velocity as a function of the external magnetic field in a film with defects at zero and finite temperature. B_{dep} is the critical magnetic field required to depin a DW at zero temperature. In the presence of pinning, the DW dynamics can be separated in 3 regimes: creep, depinning, and flow regimes. Figure adapted from Ref. 100.

In an ideal film without defects or thermal fluctuations, the dynamics of DW motion under a magnetic field applied along the easy axis can be divided in two regimes [Fig. 2.5 (a)]. The steady state regime corresponds to the motion of DWs in the presence of a weak magnetic field B and is characterized by the linear velocity response with B. Above the Walker field (B_w), as the damping torque cannot compensate the Zeeman torque any more, the DW precesses[101], thus the velocity drops before increasing linearly again.

In real ferromagnetic layers, however, defects such as impurities and structural or chemical inhomogeneities influence the DW motion by providing pinning centers that effectively block or hinder DW motion. At zero temperature, the critical field at which DWs are depinned is called the depinning field (B_{dep}). At finite temperature, however, the thermal activation of the DW can help to depin the DWs, thus, lowering the magnetic field required [Fig. 2.5 (b)]. In this case, the DW dynamics covers 3 regimes defined as creep, depinning and flow regimes[100]. When the thermal activation and external field are small compared with the pinning potential, the DWs can only hop from one pinning potential to another in a creep-like fashion, which leads to a low velocity of the DWs. Upon increasing the external field, the DWs depin and thus the DW velocity increases rapidly. In the flow regime, as the external field is strong enough to overcome all pinning potentials, the motion of the DWs is not perturbed by the pinning sites any more, therefore the velocity is linear with the external field[100]. Note that the slope of this linear trend is also related to the damping which is a parameter correlated with the presence of the defects and disorder[100,102–104].

In addition to the external field, DWs can also be driven by the current-induced SOTs. As mentioned before, the effects of SOT on the magnetization dynamics can be regarded as the effective magnetic fields. Consequently, the DWs dynamics driven by SOTs can also be described by the three regimes explained above.

2.3.4 Current-induced domain wall motion

Figure 2.6 shows the dynamics of the left-handed Néel DWs under SOTs in the Pt/CoFe/MgO heterostructure[95]. In this system, the DMI of the Pt/Co interface favors the left-handed chirality of the DWs, similar to Pt/Co/AlO_x. The direction of the $\mathbf{B}^{DL}$ generated by the DL SOT depends on the orientation of the magnetization inside a DW. The effect of $\mathbf{B}^{DL}$ is analogous to that of a magnetic field applied parallel to the easy axis, which leads to the motion of adjacent up–down and down–up domains with velocity v_{DW} in the same direction, opposite to the electron flow j_e. However, when applying an in-plane magnetic field along the x direction, the projection of the magnetization along x (m_x) becomes unequal for up/down and down/up DWs. As $\mathbf{B}^{DL}$ is proportional to the x-projection of the magnetization (see Eq. 2.9), the DW with largest m_x moves faster than the other, thus "catching up" with the slowest DW and eventually leading to the reversal of the entire magnetic region.

The DW displacement depends on the angle between the direction of the

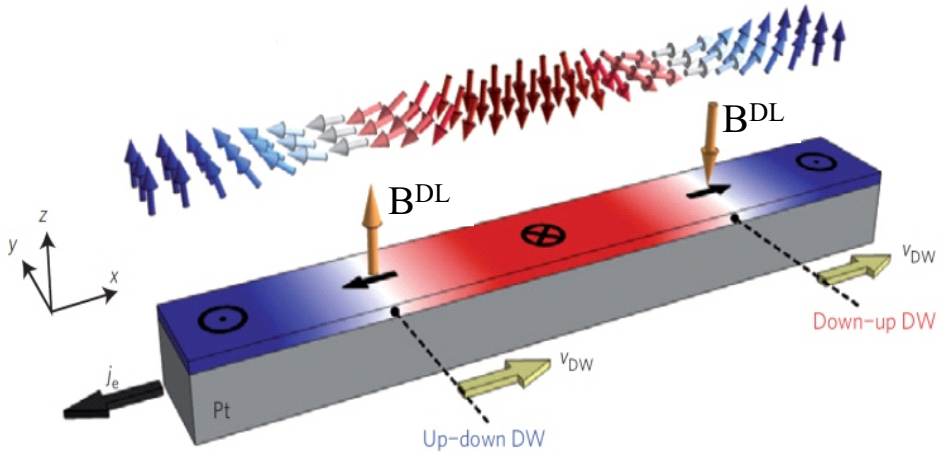

Figure 2.6 | Illustration of the current-induced motion of the left-handed chiral Néel DWs in Pt/CoFe/MgO. The current-induced effective field B^{DL} moves adjacent up–down and down–up domains with velocity v_{DW} in the same direction against the electron flow j_e. Figure adapted from Ref. 95.

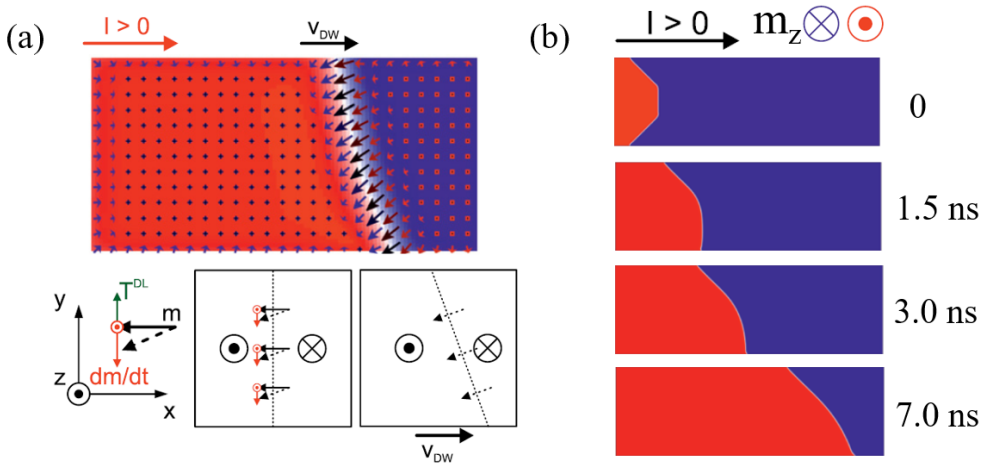

Figure 2.7 | (a) Dynamic DW tilt due to $\mathbf{T}^{DL}$ simulated for a current density of 2×10^8 A/cm^2. The original DW is parallel to y axis. (b) DW propagation during injection of a positive current 4.5×10^8 A/cm^2 simulated for a Pt/Co/AlO_x stripe that is 4.5 μm long and 1.5 μm wide. Figures adapted from Ref. 105.

current and domain wall internal magnetization[105–107]. The largest v_{DW} occurs when m_x is maximum as $v_{DW} \propto \mathbf{B}^{DL} \propto m_x$. Macrospin considerations as well as micromagnetic simulations show that the DW magnetization is distorted during the application of a current pulse, as T^{DL} rotates the DW moments away from the x direction towards the y direction. Because the DMI tends to maintain a Néel type DW, the DW tilts in response to T^{DL}. Because $v_{DW} \propto m_x$, and because m_x is modified upon current injection, DWs with different tilt angles have different velocities. This leads, for example, to the faster motion of the DW with negative tilt angle in Fig. 2.7(b), which is then rapidly expelled from a linear racetrack structure.

2.4 Skyrmions

2.4.1 Discovery of the skyrmions

Skyrmions were first observed in the inversion asymmetric B20-class chiral magnets, such as MnSi, $Fe_{0.5}Co_{0.5}Si$, FeGe[108–111] with the large bulk DMI due to the specific crystalline structures. Later, the interest has shifted to the ferromagnetic heterostructures (for example, Fe/Ir and PdFe/Ir multilayers) with interfacial DMI[112,113]. These early observations of magnetic skyrmions were done at low temperature, as the skyrmion chirality is easily destroyed by thermal fluctuations, which hindered investigations as well as applications of skyrmions in room-temperature electronic devices. This challenge was solved partially by applying an out-of-plane magnetic field to stablize magnetic skyrmions in heterostructures with either a single magnetic layer, such as Ta/CoFeB/TaO_x and Pt/Co/CoO/A_2O_3/HFO_2 [48,54,67,68,114], or magnetic superlattices, for example Pt/Co/Pt/$(Ir/Co/Pt)_{10}$/Pt [seen Fig.2.8(a) and (b)] and $(Pt/Co/Ta)_{15}$[57,59–61,64,69]. Heterostructures with geometrical confinement, on the other hand, present skyrmions at zero magnetic field [Fig.2.8(c)][58].

2.4.2 Skyrmion formation

In magnetic heterostructures with interfacial DMI, although the DMI does not change the DW shape and width, it introduces a chiral spin texture depending on the sign of DMI vector to lower the energy of the system[98,99]. The DW energy with DMI can be written as[99]:

$$\sigma = 4\sqrt{AB_K^{eff}} \pm \pi D \tag{2.14}$$

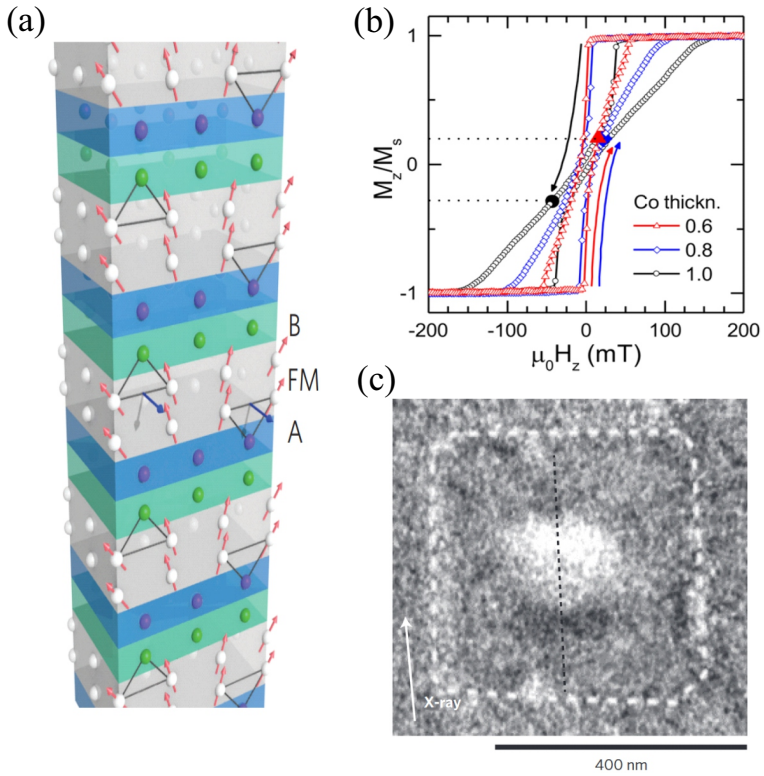

Figure 2.8 | (a) Schematic of an asymmetric multilayer made of several repetitions of Ir/Co/Pt. A and B are heavy metals with a ferromagnetic layer (FM) in between. Hysteresis loops of the perpendicular magnetization component M_z/M_s as a function of (b) the applied perpendicular field for the Pt/Co/Ir superlattice structure with different Co thickness. (c) X-ray magnetic circular dichroism - photoemission electron microscopy image of a skyrmion stablized in a 420 nm square Pt/Co/MgO element (indicated by the dotted line). At room temperature and zero external magnetic field, black/white contrast is observed at the bottom/top of the skyrmion, indicating that the skyrmion is Néel type as the in-plane DW magnetization is aligned parallel/antiparallel to the X-ray beam (see arrow). Figures adapted from Refs. 58, 59, 69.

When the DW energy goes to 0, then the critical DMI constant is given by[58,98,99]:

$$D_c = \mp 4\sqrt{AB_K^{eff}}/\pi \tag{2.15}$$

When $D < |D_c|$, the DW moments reorient smoothly to the Bloch configuration. When $D > |D_c|$, a Néel DW forms. This is also the necessary condition for the formation of skyrmions[98] as a Néel wall containing both out-of-pane and in-plane

components is the most basic chiral spin rotating configuration in the presence of the interfacial DMI[97]. Therefore, Eq. 2.15 is considered as the critical DMI threshold to form skyrmions[58,60,115–117].

Note that, as reported recently, skyrmion stability has no direct topological origin and is instead related to the competition of exchange interaction, B_K^{eff}, DMI, dipolar interaction and external field[60,118]. For example, strong exchange interaction and B_K^{eff} hinder the formation of skyrmions as they favor a collinear spin alignment along the easy axis. DMI helps to form skyrmions because it favors a noncollinear spin alignment. The dipolar interaction contributes to stabilize skyrmions by decreasing the DW energy, which in turn requires a larger external field to avoid skyrmion extension into stripe domains[119–121].

2.4.3 Skyrmion topology

A topology class describes the equivalence between two maps under smooth deformation. In the context of noncollinear spin textures, these maps are the spatial distribution of magnetic moments. Each topological class can be characterized by an integer Q called the skyrmion number or topological charge. The nontrivial skyrmion topology number is the number of times spins wind around the unit sphere[122], which is defined as follows:

$$Q = \frac{1}{4\pi} \int \mathbf{m} \cdot (\partial_{\mathrm{x}} \mathbf{m} \times \partial_{\mathrm{y}} \mathbf{m}) dx dy. \tag{2.16}$$

The skyrmion number/topological charge can be used to distinguish the topology of different types of spin textures. For example, magnetic vortices have half of the topological skyrmion number Q = ± 1/2, whereas skyrmions have Q = ± 1[67,71,97]. Note that an ideal skyrmion has a round shape, whereas the shape of the skyrmion could be distorted in real systems although, based on Eq. 2.16, its topology number is still ± 1.

2.4.4 Skyrmion Hall effect

The modified Thiele equation describes the motion of an isolated skyrmion without any pinning under the assumption that a Néel skyrmion is a rigid point-like particle[71,123]:

$$\mathbf{G} \times \mathbf{v} - 4\pi\alpha\mathcal{D} \cdot \mathbf{v} + 4\pi\mathcal{B} \cdot \mathbf{j} = 0 \tag{2.17}$$

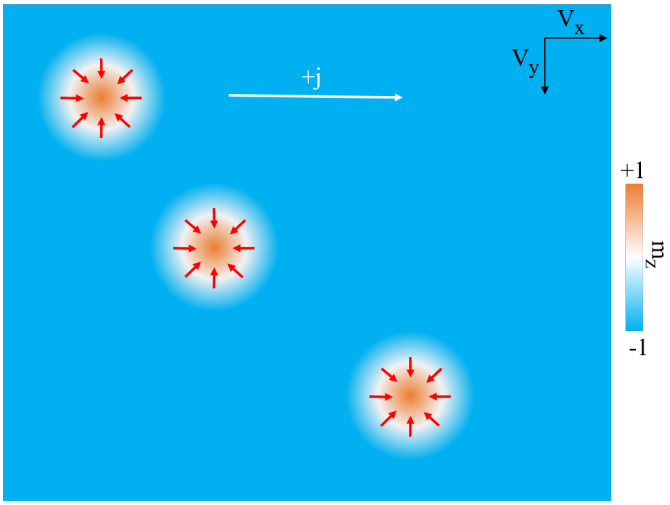

Figure 2.9 | Illustration of the skyrmion Hall effect showing the motion of a skyrmion with a constant topological charge Q = +1. The positive charge current $+j$ is injected along x direction. In addition to the longitudinal velocity v_x, there is a transverse velocity v_y during the motion. Red corresponds to a positive perpendicular (out of plane) magnetization ($+m_z$), while blue corresponds to a negative magnetization ($-m_z$).

Here, $\mathbf{G} = (0, 0, -4Q\pi)$ is the gyromagnetic coupling vector, $\mathbf{v} = (v_x, v_y)$ is the skyrmion velocity along the x and y axes. $\mathbf{G} \times \mathbf{v}$ is the topological Magnus force, which drives the skyrmion to move with a gyrotropic (transverse) velocity, leading to the Hall-like effect shown in Fig. 2.9. $-4\pi\alpha\mathcal{D} \cdot \mathbf{v}$ is the dissipative force linked to the intrinsic magnetic damping of a moving magnetic skyrmion, where α is the magnetic damping coefficient, and $\mathcal{D}$ is the dissipative force tensor, which depends on the skyrmion configuration. $4\pi\mathcal{B} \cdot \mathbf{j}$ is the driving force due to $\mathbf{T}^{DL}$, where $\mathcal{B}$ quantifies the efficiency of the SOTs over the 2-dimensional spin texture of the skyrmion, and $\mathbf{j}$ is the charge current density in the heavy metal. Upon applying current along the x (longitudinal) direction, a skyrmion moves with both longitudinal and transverse velocities, which is called the skyrmion Hall effect[57,97]. The deviation of the skyrmion motion relative to the current direction is quantified by the skyrmion Hall angle[124]

$$\theta_{sk} \approx tan^{-1}\left(-\frac{4\Delta Q}{\alpha d}\right), \tag{2.18}$$

where α is the damping parameter, d is the skyrmion diameter (this equation is valid under the assumption that $d \gg \Delta$, here Δ is the domain wall width). Therefore, for a skyrmion with fixed spin configuration, the skyrmion Hall angle

is a constant. However, recent studies shows that θ_{sk} firstly increases and then saturates with higher current density, which can be attributed to the the presence of pinning[71,125,126]. Once the current density is strong enough to drive the skyrmions to cross the creep and depinning regimes, it will have a constant θ_{sk} in the flow regime.

The skyrmion Hall effect is a drawback for applications, as it drives the skyrmions to the edge of the racetrack, leading to their annihilation. Therefore, it is important to understand and characterize the mechanisms leading to the skyrmion Hall effect. Recent studies on synthetic antiferromagnetic skyrmions with zero topology[70,72] show that skyrmion motion without the transverse velocity is possible.

3 Sample growth and characterization

In this chapter, I will firstly introduce the sputtering system used in our lab, then describe the deposition parameters for the three Pt/Co/AlO_x systems, followed by the characterization of the sample in terms of roughness, grain structure and chemical bonding information.

3.1 Magnetron sputtering

3.1.1 Mechanism of magnetron sputtering

Sputtering is a thin film deposition method that was firstly reported in the early 1800s[127]. By applying a negative voltage to the target (cathode), free electrons escaping from the cathode, collide with the Argon gas atoms that have been previously injected in the sputter deposition chamber at typical pressure around 100 mTorr. The plasma is ignited when the inert Ar gas atoms ionize due to

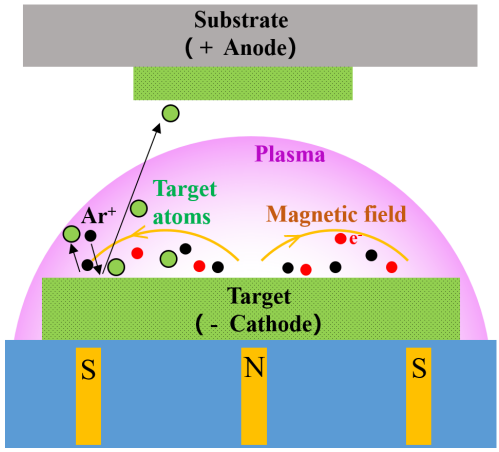

Figure 3.1 | Schematic diagram of the magnetron sputtering process. The substrate is the anode, the target is the cathode, magnets are put under the target. During the sputtering process, target atoms escape from the target surface and deposit on the substrate.

electron collisions and are attracted to the negatively charged target material at a very high velocity. The plasma atoms with typical energy 10 - 1000 eV bombard the target[128], ejecting atoms from its surface, which then deposit on the substrate surface. Secondary electrons are also emitted from the target surface as a result of the ion bombardment, and these electrons play an important

role in maintaining the plasma[129]. Due to the large deposition pressure and low deposition rate, sputtering was not widely used until magnetron sputtering was demonstrated in the late 1930s[127]. The sputtering process assisted by the magnets is called magnetron sputtering. This process is shown in Fig. 3.1. In a magnetron sputtering system, magnets underneath the target increase the ionization yield of Ar ions as the Lorentz force increases the electron path length. The increased ionization efficiency of a magnetron results in a dense plasma in the target region, leading to a higher sputtering rate at a lower operating pressure (down to 0.5 mTorr). In addition, the increased ionization efficiency achieved in magnetron sputtering allows the discharge to be maintained at lower operating voltages (typically, -500V, compared to -2000 to -3000 V) than the simple sputtering without magnet[129]. Nowadays, due to the fast deposition rate, low substrate temperature, and good adhesion of the deposited film to the substrates, magnetron sputtering is one of the most frequently used deposition methods in both laboratory and industry.

3.1.2 Commissioning of the sputtering system

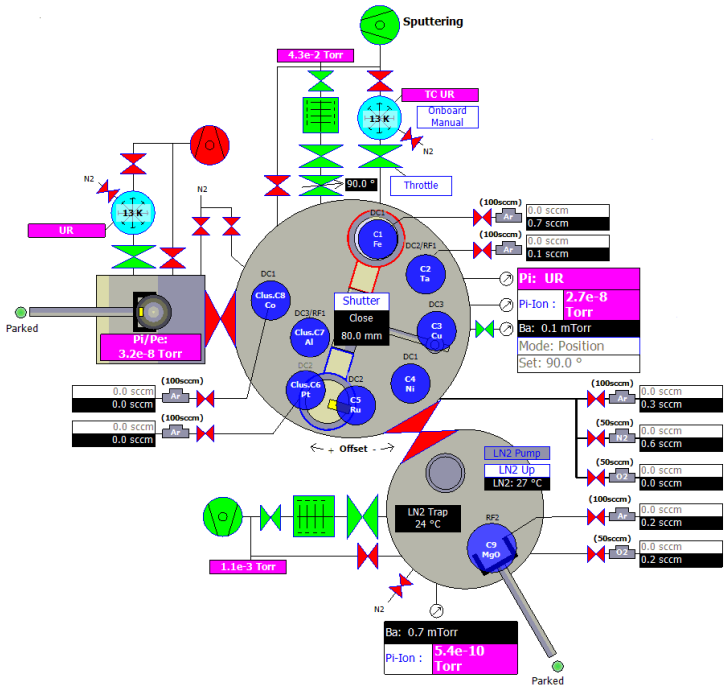

Figure 3.2 | Schematic diagram of the UHV Planetary Sputtering Cluster System.

The ultra-high vacuum planetary sputtering cluster system in the Magnetism and Interface Physics group was commissioned in 2016. As shown in Fig. 3.2, this sputtering system has three different chambers. A load lock chamber can hold five different pallets at the same time to reduce the substrate turn around time. The main sputtering chamber has a base pressure as low as 3.0×10^{-9} Torr.

Two deposition positions are available in this chamber, one is the hot position, where can heat samples up to 800°C, another is the wedge position, which shutter can be driven by a motor to open and close during the deposition, leading to a wedge layer deposition. Co-sputtering deposition is available in this chamber as cathodes 6, 7, and 8 can be tilted. Sample holders with either in-plane or out-of-plane magnetic fields are available, making it possible to perform in-situ depositions with external field. Two types of gas lines are available, one connected to the main chamber and another to the individual cathodes, leading to the deposition with a low pressure. The third chamber is the oxidation chamber including a liquid nitrogen cooling position with base pressure as low as 3.0×10^{-10}Torr. Both DC and RF power supplies are available for the main sputtering and the oxidation chamber. All the depositions in this system can be done automatically and samples can be transferred from one chamber to another automatically.

Homogeneity

In order to make sure that the deposited samples are homogeneous enough, I performed several tests of Al deposition on a SiO_2 substrate with the tilted target and a wedge mask on the pallet. Before the Al deposition, resist was spin-coated and patterned with by photolithography for lift-off. The thickness of Al was measured by the DektakXT surface step profiler with a vertical resolution of 1 nm. The thickness distribution diagram is shown in Fig. 3.3. After deposition, the grey part in Fig. 3.3 presents a different color relative to the other parts, which is mainly due to the shadow effect and relatively large thickness of the wedge mask, which blocks the deposition. The low thickness region shaded in red with $t_{\mathrm{Al}} = 20$ - 24 nm is due to the shadow effect, whereas the intermediate thickness region shaded in light blue with $t_{\mathrm{Al}} = 25$ - 27 nm is due to wedge mask. The middle 12 mm×10 mm dark blue part with $t_{\mathrm{Al}} = 26$ - 27 nm (2% variation), is considered to have a very good homogeneity.

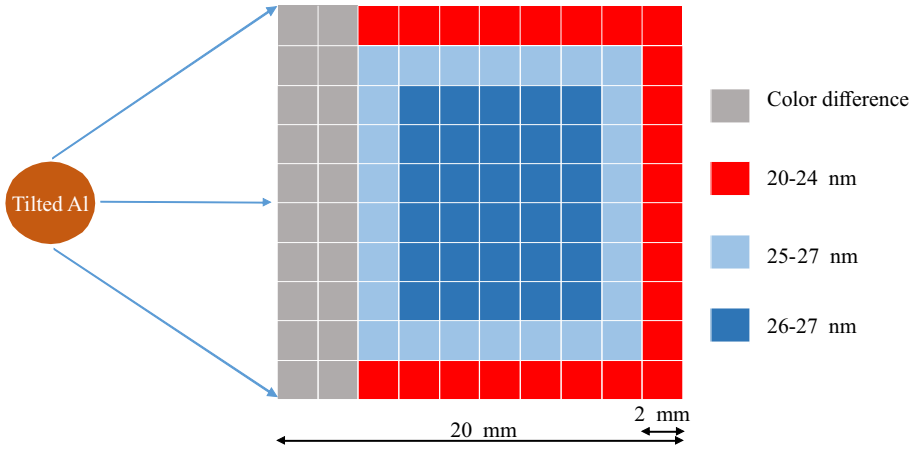

Figure 3.3 | Thickness measurement of a 20 mm × 20 mm Al/SiO_2 sample with a tilted Al target and wedge mask. The regions with different thicknesses are shaded in different colors.

Accuracy and reproducibility

Since the thickness during deposition needs to be as precise as possible, we deposited five different Pt single layer samples on SiO_2 substrates with a nominal thickness of 11 nm, and then measured the thickness by ellipsometry [Fig. 3.4 (a)]. The maximum thickness variation from the set value is around 2%, which demonstrates that the accuracy of this sputtering system is well-guaranteed. The thickness of these five samples is quite similar, meaning that the reproducibility is also good.

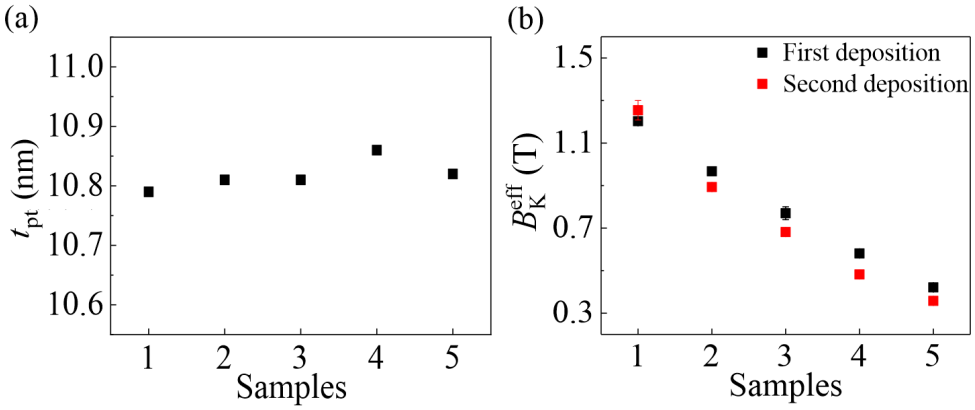

Figure 3.4 | (a) Thickness of 5 different Pt samples measured by ellipsometry. (b)B_K^{eff} of Pt(5)/Co(1)/AlO_x samples for two different batches, first deposition (black dots) and second deposition (red dots).

To test the reproducibility of the magnetic properties, five different Pt(5)/Co (1)/AlO_x samples in a single Al wedge batch were deposited on SiN substrates. As a comparison, a new second deposition was done with exactly the same recipe two months later. The effective anisotropy field (B_K^{eff}) was measured and shown in Fig. 3.4(b). From the data we can see that, even after two months, the samples present comparable magnetic properties.

Wedge deposition tests

Wedge deposition guarantees that the thickness is the only variable. Therefore it is a very good choice for the oxidation study which will be described in the following section. By measuring the thickness of Pt layers after the wedge deposition, we found that the Pt thickness increases linearly with the motion of the wedge shutter. For the following study in this thesis, I also tested the effective anisotropy field B_K^{eff} as a function of shutter motion. Fig. 3.4(b) shows that B_K^{eff} decreases linearly with thicker Al (thickness increases from Sample 1 to 5, further explanation in Chap. 4), demonstrating the wedge deposition is a very effective way to tune the magnetic properties of thin films.

3.2 Sample depositions and patterning

In this section, I will describe the sample deposition parameters and the photolithography process used to fabricate the patterned devices for the electrical measurements.

3.2.1 Depositions

I grew three series of samples on Si_3N_4 wafers using dc magnetron sputtering with base pressure $<8.0 \times 10^{-8}$ Torr and Ar pressure between 0.3 and 1.1 mTorr. The first series, which I refer to as Pt/Co/AlO_x, was obtained by depositing an Al wedge on a Pt(5)/Co(1) bilayer, where the numbers between parentheses represent the thickness in nm. After deposition of the full metallic stack, an oxygen plasma with 10.0 mTorr pressure and 53 W power was used to oxidize the Al wedge with the purpose of obtaining over- and under-oxidized regions of the top Co interface [Fig. 3.5(a)]. The deposition parameters for this system are shown in Table 3.1. Note that the easy magnetization axis is perpendicular to sample's plane for an Al thickness $t_{Al} = 13.4 - 18.9$ Å, whereas beyond this range the easy axis is in-plane, in agreement with previous reports[29,30,32,33].

$Pt/Co/AlO_x$					
Layer	Pressure (mTorr)	Power (W)	Current (mA)	Process time (s)	Thickness (nm)
Pt	0.3	8	20	67	5
Co	0.3	9	25	25	1
Al	0.9	15	40	wedge	1.34-1.89
Oxidation	12.8	28	-	35	-

Table 3.1 | Deposition parameters for the Pt(5 nm)/Co(1 nm)/AlO_x thin films by dc magnetron sputtering in chronological order from top to bottom.

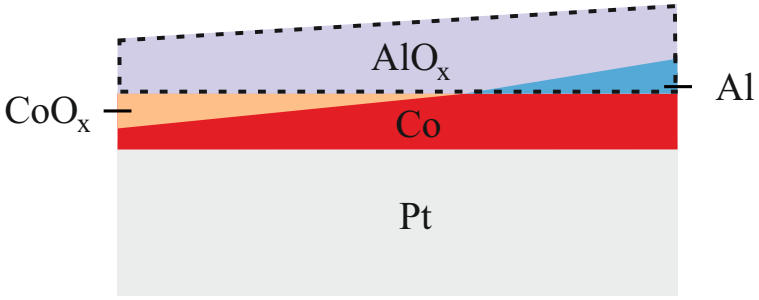

Figure 3.5 | Schematic diagram of $Pt/Co/AlO_x$trilayers.

The second series is $Pt(5)/CoO_x(t_{CoO_x})/Co(0.65)/AlO_x(1.85)$, which was grown by depositing a CoO_x wedge layer with thickness $t_{CoO_x} = 2.1 - 4.9$ Å on Pt by reactive sputtering of Co with an O_2:(Ar + O_2) ratio of 50% [Fig. 3.6]. The deposition parameters for this system are shown in Table 3.2. $t_{Al} = 1.85$ nm which is slightly thicker than the "optimized" Al thickness ($t_{Al} = 1.76$ nm, see details in the following section) to ensure that all the samples of this series have PMA with metallic Al.

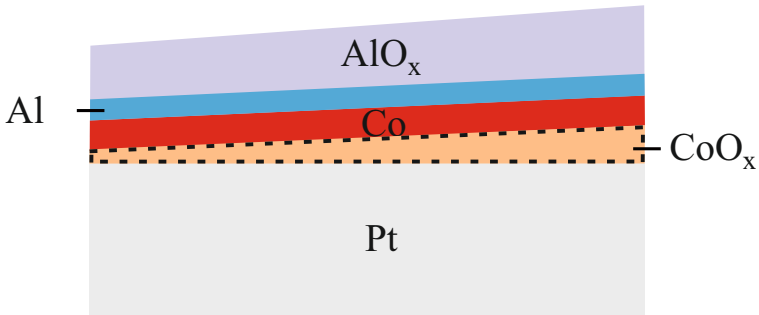

Figure 3.6 | Schematic diagram of $Pt/CoO_x/Co/AlO_x$.

$Pt/CoO_x/Co/AlO_x$					
Layer	Pressure (mTorr)	Power (W)	Current (mA)	Process time (s)	Thickness (nm)
Pt	0.4	8	20	67	5
CoO_x	0.5	10	25	wedge	2.1-4.9
Co	0.5	10	25	16	0.65
Al	1.1	15	40	60	1.85
Oxidation	12.3	28	-	35	-

Table 3.2 | Deposition parameters for the Pt(5 nm)/Co_x/Co(0.65 nm)/AlO_x(1.85nm) thin films by dc magnetron sputtering in chronological order from top to bottom.

Unlike the first two series that have a wedge structure, the third serie includes seven different samples grown with an O_2:(Ar + O_2) ratio ranging between 0 and 60% during deposition of the Pt layer. In order to make all these samples have the same easy axis, a 2.5 nm-thick Al layer was deposited to obtain in-plane magnetic anisotropy, resulting from the under-oxidation of the Al cap layer and much reduced perpendicular anisotropy at the PtO_x/Co interface. The deposition parameters for this system are shown in Table 3.2.

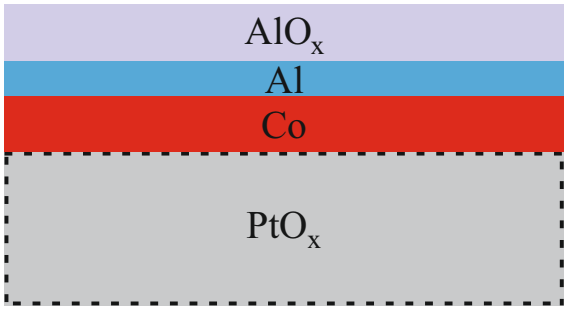

Figure 3.7 | Schematic diagram of PtO_x/Co/AlO_x.

$PtO_x/Co/AlO_x$					
Layer	Pressure (mTorr)	Power (W)	Current (mA)	Process time (s)	Thickness (nm)
PtO_x	2.0	10	20	60	5
Co	1.5	9	25	25	1
Al	1.0	3	7	180	2.5
Oxidation	12.8	28	-	35	-

Table 3.3 | Deposition parameters for the PtO_x(5 nm)/Co(1 nm)/AlO_x (2.5nm) thin films by dc magnetron sputtering in chronological order from top to bottom.

After deposition, all the samples were diced in two pieces, one for the characterization of the structure and magnetization properties, and the other for device patterning and SOT measurements. The devices are 10 μm wide and 50 μm long Hall bars defined by optical lithography followed by Ar milling.

3.2.2 Patterning

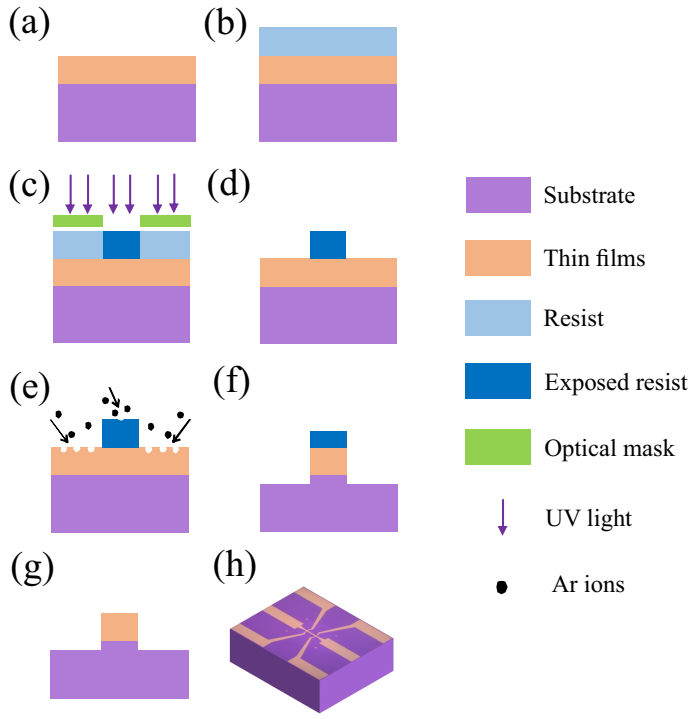

Figure 3.8 | Step by step photolithograph fabrication procedures (a to h).

We use photolithography to fabricate devices for the electrical measurements. This process is illustrated in Fig. 3.8. We firstly spin coat the resist with 4000 rpm speed and then bake the substrate for 120 seconds at 120 °C, after which a 2 μm thick negative maN-1420 photo resist layer (b) is spin-coated on the top of the sample (a). Then we let the UV light (UV radiation of 10 mW/cm^2 intensity and 310W for 30s) from the MJB3 mask aligner pass through the glass mask, which is partially covered by the metallic layers, in order to expose the resist partially (c). The structure of the resist which is exposed by the UV radiation changes, making it resistant to the D533s developer (d). After Ar ion etching (e), the area of the film without resist will be etched away (f). Finally, by removing the remaining resist with acetone (g), we obtain the devices with

Hall bar patterns (h).

3.3 Structural characterization

After sample fabrications and patterning, I measured the roughness, grain sizes and orientation, as well as used XPS to characterize these three systems.

3.3.1 Roughness

Atomic force microsopy (AFM) is used to measure the roughness of the deposited samples. The root mean square (RMS) roughness data in Fig. 3.9 shows that, with increasing Al thickness, the roughness becomes larger. This means that Al deposition is relatively rough due to self shadowing[130]. In order to investigate whether the oxygen plasma during deposition leads to a much rougher surface or not, a new test sample SiN/Pt(5)/Co(1)/Al(1.76)/Pt(1) was deposited using the same recipe. Here, Pt 1 nm capping was used to prevent Al from being oxidized in air. Compared with the previous sample with the same Al thickness, which has an RMS roughness of 7.8 Å, the RMS roughness of the test sample is around 5 Å, which suggests that the oxygen plasma probably leads to the much rougher surface.

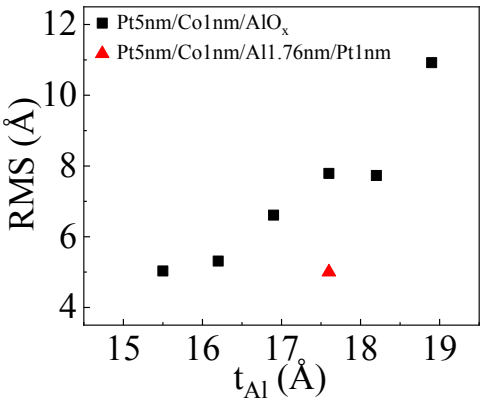

Figure 3.9 | RMS roughness of Pt/Co/AlO$_x$ samples with different Al thickness. The red triangle indicates the sample with Pt 1 nm cap layer on top instead of oxygen plasma treatment during deposition for comparison.

3.3.2 Transmission Kikuchi diffraction

Transmission Kikuchi diffraction (TKD) also known as transmission electron back scatter diffraction (EBSD), gives information on the grain size, orientation

and distribution of crystalline samples.

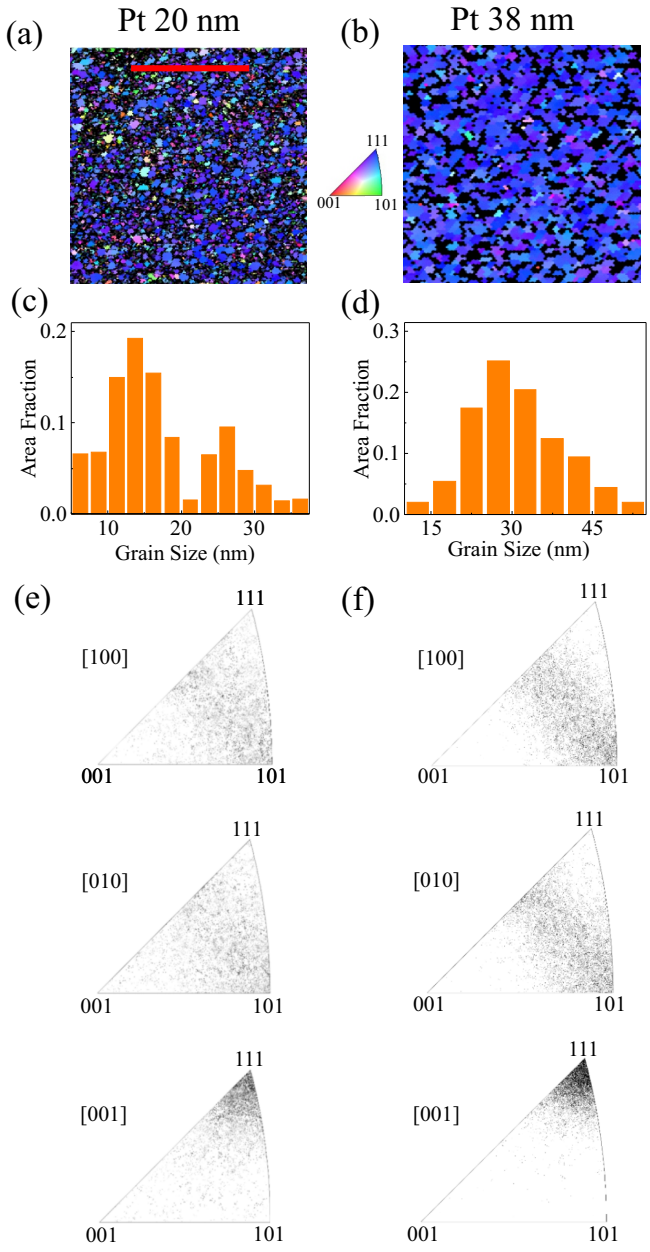

Figure 3.10 | Crystal orientation mapping obtained by TKD of (a) Pt 20 nm and (b) Pt 38 nm. The scale bar is 300 nm. Color code according to unit triangle of crystal directions with respect to the sample normal direction. Raw data are post-processed by clean up routines in software OIM Analysis (CI standard, O corr). Grey levels indicate pixels with low reliability in indexing (confidence index between 0 and 0.1). Grain size distribution of (c) Pt 20 nm and (d) Pt 38 nm. Grain inverse pole figures of (e) Pt 20 nm and (f) Pt 38 nm from TKD measurements.

A spatial resolution improvement of up to one order of magnitude relative to EBSD can be achieved by TKD. This technique uses Kikuchi patterns captured from underneath an electron transparent sample, while the EBSD signal is produced by back scattering diffracted electrons escaping a highly tilted sample. TKD uses existing EBSD hardware but requires software adaptations and electron transparent samples deposited on the TEM lamella. TKD's high spatial resolution performance makes it the best choice for quantitative characterization of nanomaterials or ultrafine grained materials.

Dr. Karsten Kunze (ScopeM, ETH) performed TKD to characterize the crystal structure of ultrathin Pt layers. Three Pt samples with thickness 10, 20 and 38 nm were deposited on SiN membrane windows. The Kikuchi signal of the 10 nm thick Pt sample is so low that we cannot obtain enough data points for a complete TKD measurement. For the two thicker samples, the crystal orientation mapping and grain size figures are given in Fig. 3.10(a)-(d). Different colors in Fig. 3.10(a) indicate different crystal orientations, thus both Pt layers are polycrystalline. From Fig. 3.10(c) we can tell that, in the 20 nm thick sample, most of the grains have a size of 15 nm, while for the 38 nm thick sample, most of the grains have a size of 25 nm. This indicates that thinner Pt layers have smaller grain size, and most grain sizes are smaller than the thickness. Although we can not measure the 5 nm thick Pt due to the low signal, we can deduce from Fig. 3.10(c) and (d) that the ultrathin Pt should be nanocrystalline. In addition to the grain size information, we obtain the crystal orientation information from the two grain inverse pole figures Fig. 3.10(e) and (f). The grain inverse pole figure gives the density of crystals with certain orientations. As Pt has the face-centered cubic structure, we observed the structures from three identical directions: [100], [010] and [001]. The [111] corners cover more crystals meaning that grains with this orientation are preferred in both Pt films. Comparing with Fig. 3.10(e) and (f), we can conclude from the difference of the amount of the crystals that for the thicker Pt, more crystals prefer to have the [111] crystal orientation than the thinner one. This is reasonable as Pt has the face-centered cubic structure with the energy-favorable [111] closed packed plane. Therefore for the thicker Pt films, more grains prefer to have the [111] orientation in order to minimize the energy of the system during the deposition process.

3.3.3 X-ray photoelectron spectroscopy

We performed x-ray photoemission spectroscopy (XPS) in order to characterize the oxidation state of Pt/Co/AlO_x and PtO_x/Co/AlO_x series described above.

Figure 3.11(a) shows the XPS spectra of Pt/Co/AlO_x recorded by measuring photoemission from the Co $2p_{1/2}$ and $2p_{3/2}$ core levels of samples with different t_{Al}. The spectra of samples with t_{Al} larger than 17.6 Å present two peaks at 778.1 and 793.4 eV, which are characteristic of metallic Co (Refs. 30, 31). On the other hand, the spectra of samples with t_{Al} smaller than 17.6 Å show high energy shoulders at 780.7 and 796.7 eV characteristic of CoO (Ref. 30, 31), the intensity of which increases with decreasing Al thickness. These measurements show that the Co/Al interface is underoxidized and that Co remains fully metallic down to t_{Al} = 17.6 Å, after which CoO forms. We designate the sample with t_{Al} = 17.6 Å as the "optimized" sample for which the Co/Al interface is fully oxidized, leading to maximum PMA.

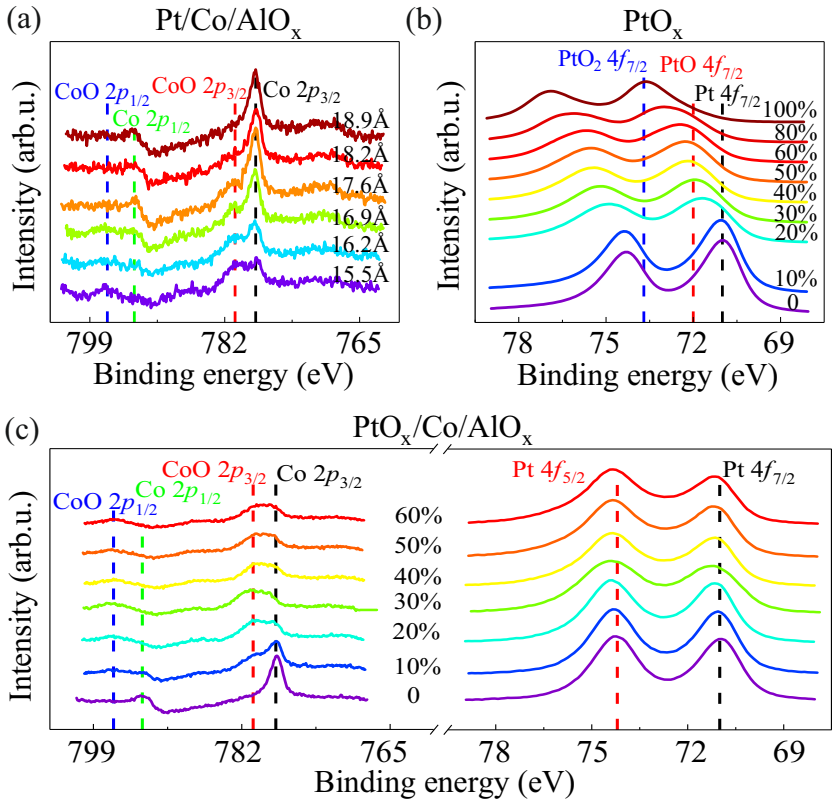

Figure 3.11 | The XPS spectra of (a) Co $2p$ edges in Pt/Co/AlO_x system with different t_{Al}, (b) Pt $4f$ edges in PtO_x single layers with different O_2 ratio and (c) Co $2p$ and Pt $4f$ edges in PtO_x/Co/AlO_x trilayers with different O_2 ratio.

In order to characterize the third series, we first measured the XPS spectra of single PtO_x(5) layers deposited on Si_3N_4 with the same O_2:(Ar + O_2) ratios as used for the full PtO_x/Co/AlO_x trilayers as a reference. The spectra, reported

in Fig. 3.11(b), show the evolution of the Pt $4f_{7/2,5/2}$ doublet with increasing O_2 partial pressure. As the energy of the Pt $4f_{5/2}$ level overlaps with the Al $2p$ level around 74.6 eV, typical of Al_2O_3 (Ref. 131), we focus on the behavior of the $4f_{7/2}$ peak. This peak shifts from 71 eV below 10% O_2, as typical of Pt, to 72 eV around 40% O_2, characteristic of PtO, and finally to 73.7 eV at 100% O_2, indicating the formation of PtO_2 (Ref. 47). These spectra confirm that a single layer of Pt can be stably oxidized by controlling the amount of O_2 during sputtering. However, the measurements of the full PtO_x/Co/AlO_x stack, shown in Fig. 3.11(c), reveal quite a different picture. In these samples, the Pt $4f_{7/2}$ peak does not shift with increasing O_2 partial pressure, showing that Pt remains metallic. On the other hand, a strong shift of the Co $2p$ peaks is observed, indicating the formation of CoO upon diffusion of oxygen into Co from the Pt side.

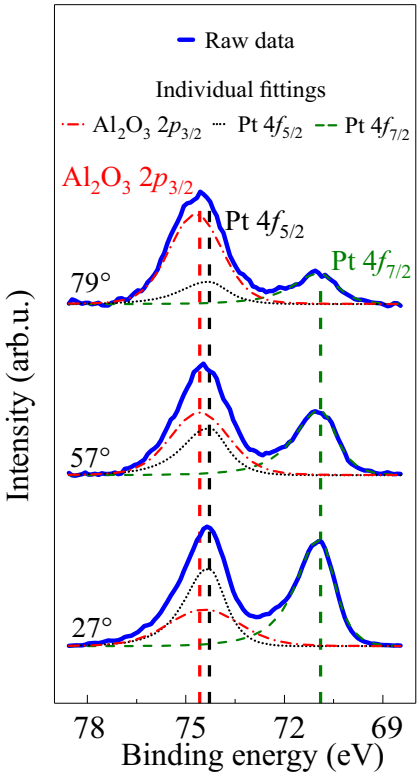

Figure 3.12 | Angle-resolved XPS of the Al $2p$ and Pt $4f$ edges in PtO_x(40%)/Co/AlO_x trilayers, three incident angles are indicated with repect to the sample surface normal, the higher angle during the measurement, the more surface sensitivity it has. The raw data and individual fittings are given in different colors and symbols.

The progressive oxidation of the top layers resulting from oxygen diffusion was further characterized using angle-resolved XPS by Prof. Antonella Rossi and Dr. Giovanni Cossu at ETH, as shown in Fig. 3.12 for PtO_x(40%)/Co/AlO_x. The spectra recorded with an increasing angle of incidence relative to the surface normal, from 27° to 79°, have a higher degree of surface sensitivity. These spectra reveal a progressive increase of the Al_2O_3 intensity relative to Pt, showing that Al is strongly oxidized, whereas the position of the Pt peak does not change as a function of incidence angle. Note that t_{Al} = 25 Å in this series, such that Al was supposed to be underoxidized. Overall, these observations indicate that PtO_x layers are not stable when embedded in a multilayer structure, as oxygen tends to diffuse away from Pt and oxidize both the Co and Al layers. Such a behavior can be rationalized in terms of the formation enthalpy of PtO_x (-101.3 kJ/mol)[132], which is significantly lower than that of AlO_x (-1675.7 kJ/mol)[133] and CoO_x (-237.4 kJ/mol)[134].

4 Experimental methods

In this chapter, I will introduce three different methods and instruments used to characterize the SOTs and magnetic properties of the samples.

Generally speaking, we can measure the SOTs and (or) magnetotransport properties by methods such as MOKE, DW motion, ferromagnetic resonance (FMR) and harmonic voltage methods. In this chapter, I will introduce how to obtain the SOTs, efficiencies, effective anisotropy field as well as the thermal gradient signals by the harmonic Hall voltage methods.

Magnetic domains are characterized by a MOKE and a magnetic force microscope (MFM) which are introduced in the last two sections of this chapter.

4.1 Harmonic Hall voltage measurements

We describe the magnetization in the Cartesian coordinate as shown in Fig. 4.1. The current direction is along the x axis, θ is the polar angle between the magnetization and the z axis, and φ is the azimuthal angle between magnetization and x axis.

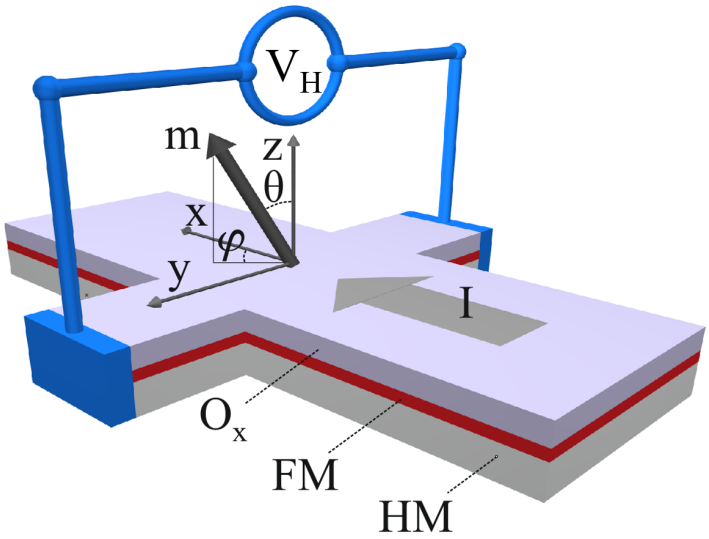

Figure 4.1 | Geometry of the harmonic measurement.

The anomalous Hall resistance, magnetic anisotropy, and SOT effective fields are measured using the harmonic Hall voltage method[7,20,23,90,91]. The method is based on the injection of an ac current $I = I_0 \cos(\omega t)$ with amplitude I_0 and

frequency $f = \omega/2\pi$ typically around 10 Hz. As the magnetization oscillates around its equilibrium state due to the oscillating SOTs, the Hall resistance varies as $R_H(t) = R_H(\mathbf{B}_0 + \mathbf{B}_I)$, where $\mathbf{B}_0$ is the sum of the external field $\mathbf{B}_{\text{ext}}$ and effective anisotropy field $\mathbf{B}_K^{eff}$, and $\mathbf{B}_I$ is the sum of the current-induced effective fields $\mathbf{B}^{DL}$, $\mathbf{B}^{FL}$, and the Oersted field $\mathbf{B}^{Oe}$. In this situation, the Hall voltage can be written as

$$V_H = I_0 \cos(\omega t)\, R_H(\mathbf{B}_0 + \mathbf{B}_I) \tag{4.1}$$

$$= I_0[R_H^0 + R_H^\omega \cos(\omega t) + R_H^{2\omega} \cos(2\omega t)]. \tag{4.2}$$

Here, R_H^0, R_H^ω, and $R_H^{2\omega}$ are the zeroth, first, and second harmonic Hall resistance, respectively. R_H^ω corresponds to the Hall resistance measured in a dc experiment, which is determined by the anomalous Hall effect (AHE) and planar Hall effect (PHE):

$$R_H^\omega = R_{\text{AHE}} \cos\theta + R_{PHE} \sin^2\theta \sin(2\varphi), \tag{4.3}$$

where R_{AHE} and R_{PHE} are the AHE and PHE coefficients, respectively, and θ and φ are the polar and azimuthal angles of the magnetization, as defined in Fig. 1(e) of the main text. The ordinary Hall resistance is negligibly small in our samples compared with R_{AHE} and R_{PHE}, and ignored in the following. For samples with perpendicular magnetic anisotropy (PMA), namely $\text{Pt/Co/AlO}_\text{x}$ and $\text{Pt/CoO}_\text{x}\text{/Co/AlO}_\text{x}$, R_{AHE} is given by half of the difference between the R_H^ω when the magnetization is up/down at $B_{\text{ext}} = 0$ [Fig. 4.2(a,b)]. For samples with in-plane magnetic anisotropy, namely $\text{PtO}_\text{x}\text{/Co/AlO}_\text{x}$, we swept B_{ext} out-of-plane up to 2.2 T magnetic field and estimated R_{AHE} as the intercept of the linear fit of the R_H^ω with the y-axis [Fig. 4.2(c)]. Examples of R_H^ω and $R_H^{2\omega}$ as a function of applied field for samples of the three series with different oxidation levels are shown in Fig. 4.2.

4.1.1 Measurement of B_K^{eff}

The effective magnetic anisotropy field is determined from the field dependence of R_H^ω reported in Fig. 4.2(a-c). For the samples with PMA, B_K^{eff} is given by

$$B_K^{\text{eff}} = \left| \frac{cos\theta_B}{cos\theta} - \frac{sin\theta_B}{sin\theta} \right| B_{\text{ext}}, \tag{4.4}$$

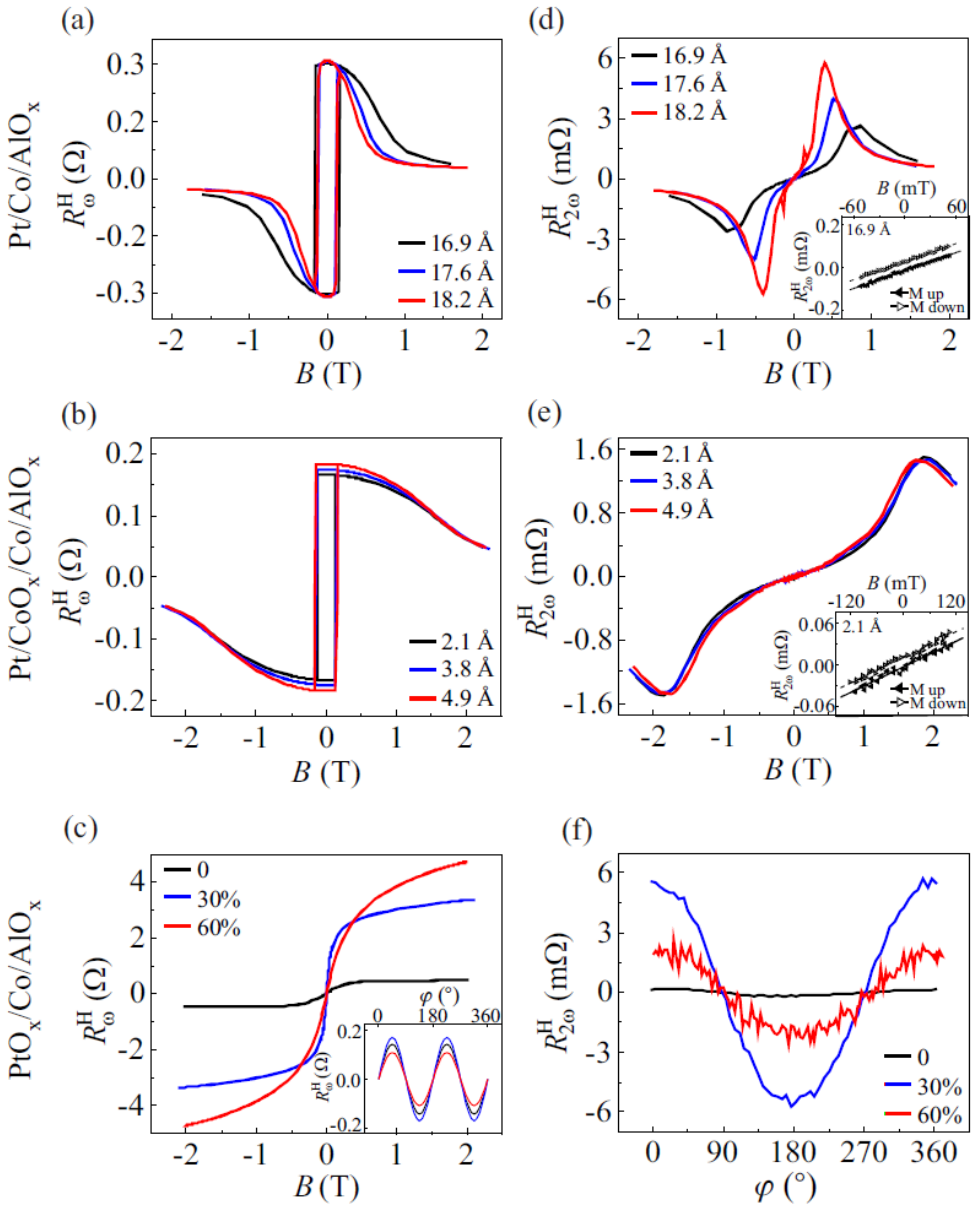

Figure 4.2 | R^{ω}_H as a function of external field for (a) Pt/Co/AlO$_x$ with different t_{Al}, (b) Pt/CoO$_x$/Co/AlO$_x$ with different t_{CoO_x}, and (c) PtO$_x$/Co/AlO$_x$ with different O_2 ratios. (d,e) $R^{2\omega}_H$ measured simultaneously with the curves shown in (a,b). Close ups of the low field behavior of $R^{2\omega}_H$ for the two systems are shown in the insets. (f) $R^{2\omega}_H$ as a function of φ_B for PtO$_x$/Co/AlO$_x$, measured simultaneously with the angle scans of R^{ω}_H shown in the inset of (c). For Pt/Co/AlO$_x$ and Pt/CoO$_x$/AlO$_x$, the external field is applied at angles $\theta_B = 86°$ and $\varphi_B = 0°$. For PtO$_x$/Co/AlO$_x$, the field is applied at $\theta_B = 0°$. The in-plane angle scans are performed by varying the direction of a 1 T external field.

where θ_B is the polar angle of the applied field, which is set prior to the measurement, and θ is obtained from Eq. 4.3. This equation assumes that the magnetization behaves as a macrospin in a uniaxial anisotropy field, which is approximately correct as long as R_H^ω has a reversible behavior versus the external field.

All the samples of the $PtO_x/Co/AlO_x$ series have in-plane magnetic anisotropy (B_K^{eff} <0), which cannot be estimated using the method described above. An approximate estimate of B_K^{eff} in this series can be obtained by measuring the field required to saturate the magnetization along the out-of-plane hard-axis. In the macrospin approximation, such a field corresponds to the sum of the demagnetizing field and magnetocrystalline anisotropy field, as given in Eq. 1. The hard axis saturation field is obtained by the crossing point of the two lines that fit R_H^ω at high field and in the low field region where the magnetization coherently rotates from in-plane to out-of-plane [Fig. 4.2(c)].

4.1.2 Methods for SOTs effective fields

For samples with PMA, the dependence of $R_H^{2\omega}$ on the current is conveniently expressed as[23,90]

$$\begin{aligned} R_H^{2\omega} =& [R_{\mathrm{A}HE} - 2R_{PHE}\cos\theta\sin(2\varphi)]\frac{d\cos\theta}{d\mathbf{B}_I}\cdot\mathbf{B}_I \\ &+ R_{PHE}\sin^2\theta\frac{d\sin(2\varphi)}{d\mathbf{B}_I}\cdot\mathbf{B}_I + I_0\alpha\nabla T\sin\theta\cos\varphi, \end{aligned} \tag{4.5}$$

where $\mathbf{B}_I = \mathbf{B}^{DL} + \mathbf{B}^{FL} + \mathbf{B}^{Oe}$ and $I_0\alpha\nabla T$ is the anomalous Nernst voltage due to the out-of-plane temperature gradient induced by Joule heating[90]. The subtraction of $I_0\alpha\nabla T$ is introduced later. Inhomogeneous current flow in a Hall cross also results in a smaller in-plane temperature gradient, whose Nernst voltage can be subtracted from $R_H^{2\omega}$ by performing a measurement at $\theta_B = 0^\circ$[23,135]. Note that the angle dependent thermal voltage signals should be subtracted from $R_H^{2\omega}$ in order to avoid overestimating the SOTs.

In order to measure the first order contributions to the SOT, it is sufficient to consider the limit of small oscillations of the magnetization about the out-of-plane direction ($\theta \approx 0^\circ$). In such a case, B^{DL} and B^{FL} can be obtained as follows after subtracting the vertical thermal component $I_0\alpha\nabla T\sin\theta\cos\varphi$[20,91]

$$B_{\theta\approx0^\circ}^{DL,FL} = -2\frac{\partial(R_H^{2\omega} - I_0\alpha\nabla T\sin\theta\cos\varphi)}{\partial B_{\varphi=0^\circ,90^\circ}} \Big/ \frac{\partial^2 R_H^\omega}{\partial B_{\varphi=0^\circ,90^\circ}^2}, \tag{4.6}$$

where $\frac{\partial(R_H^{2\omega}-I_0\alpha\nabla T\sin\theta\cos\varphi)}{\partial B_{\varphi=0^\circ,90^\circ}}$ is the derivative of $R_H^{2\omega}-I_0\alpha\nabla T\sin\theta\cos\varphi$ as a function of external field and simultaneously $\frac{\partial^2 R_H^{\omega}}{\partial B^2_{\varphi=0^\circ,90^\circ}}$ is the second derivative of R_H^{ω} as a function of external field ($\theta\approx 0^\circ$, and $\varphi=0^\circ$ for B^{DL}, $\varphi=90^\circ$ for B^{FL}).

If $R_{PHE}\ll R_{AHE}$, Eq. 4.6 is enough to quantify the SOT effective fields, which are proportional to the ratio of the current-dependent Hall susceptibility and a normalization factor that accounts for the tendency of the magnetization to remain aligned along the easy axis. If R_{PHE} cannot be ignored, a correction to Eq. 4.6 is required[23,91], which gives

$$B^{DL,FL} = \frac{B^{DL,FL}_{\theta\approx 0^\circ}\pm 2rB^{FL,DL}_{\theta\approx 0^\circ}}{1-4r^2}, \tag{4.7}$$

where $r=R_{PHE}/R_{\mathrm{A}HE}$.

In order to quantify the SOTs in samples with in-plane magnetic anisotropy we performed harmonic Hall voltage measurements by rotating the sample in the xy plane and applying a sufficiently large external field (with various amplitudes) to ensure the magnetic saturation of the sample is along the field direction. In this geometry, assuming that the in-plane magnetization is isotropic, $R_H^{2\omega}$ is given by[90]:

$$\begin{aligned} R_H^{2\omega} =&(R_{\mathrm{A}HE}\frac{B^{DL}}{B_{ext}-B_{\mathrm{K}}^{\mathrm{eff}}}+I_0\alpha\nabla T)\cos\varphi \\ &+2R_{PHE}(2\cos^3\varphi-\cos\varphi)\frac{B^{FL}+B^{Oe}}{B_{ext}}. \end{aligned} \tag{4.8}$$

We note that, by symmetry, there are two contributions to the above signal, the first one is proportional to $\cos\varphi$ and depends on both the DL-SOT and Nernst effect, and the second one is proportional to $2R_{PHE}(2\cos^3\varphi-\cos\varphi)$ and depends on the FL-SOT. We fit $R_H^{2\omega}$ by using these two expressions and obtain two coefficients, $(R_{\mathrm{A}HE}\frac{B^{DL}}{B_{ext}-B_{\mathrm{K}}^{\mathrm{eff}}}+I_0\alpha\nabla T)$ and $\frac{B^{FL}+B^{Oe}}{B_{ext}}$ for each external field value. Plotting these two coefficients as a function of $\frac{1}{B_{ext}-B_{\mathrm{K}}^{\mathrm{eff}}}$ and $\frac{1}{B_{ext}}$ yields a linear curve with slopes corresponding to B^{DL} and B^{FL}, respectively. Finally, the intercept of $(R_{\mathrm{A}HE}\frac{B^{DL}}{B_{ext}-B_{\mathrm{K}}^{\mathrm{eff}}}+I_0\alpha\nabla T)$ vs. $\frac{1}{B_{ext}-B_{\mathrm{K}}^{\mathrm{eff}}}$ gives the thermal contribution due to the out-of-plane temperature gradient and resulting anomalous Nernst effect (Fig. 4.3). We note that here B^{FL} is the sum of SOT and Oersted field contributions from which the latter is calculated as $B^{Oe}=\mu_0 j_{\mathrm{HM}}t_{\mathrm{HM}}/2$ in our samples, where j_{HM} is the current density of HM and t_{HM} is the thickness of

the HM[23,135]. We found $B^{Oe} = 0.31$ mT for current density of 1.0×10^7 A/cm^2 in Pt(5)/Co(1)/AlO$_x$.

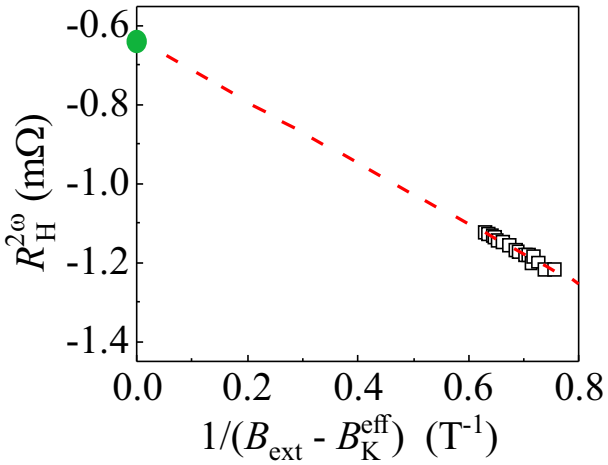

Figure 4.3 | Separation of B^{DL} and Nernst thermal $I_0\alpha\nabla T$ contribution from $R_H^{2\omega}$. Plot the cosine component of $R_H^{2\omega}$ as a function of $\frac{1}{B_{ext}-B_K^{eff}}$ measured in a field scan performed $\varphi = 45°$ for Pt(5)/Co(1)/AlO$_x$ with current density 1.0×10^7 A/cm^2. The intercept (green dot) of the linear fitting is the thermal contribution.

We note that Eq. 4.8 and the analysis described above is equally valid for PMA samples as long as the magnetization is fully saturated in-plane by applying a B_{ext} larger than B_K^{eff}. Alternative to the angle scan measurements which are time consuming, an easier way to determine the thermal contribution and B^{DL} in PMA samples is by performing an in-plane field sweep along $\varphi = 45°$ at magnetic saturation (i.e., $B_{ext} > B_K^{eff}$). In this measurement the second term on the right hand side of Eq. S8 vanishes by symmetry (since $2\cos^3\varphi - \cos\varphi = 0$). After subtracting a magnetically irrelevant offset on the signal, the data are plotted as a function of $\frac{1}{B_{ext}-B_K^{eff}}$, B^{DL} and the thermal contribution at $\varphi = 45°$ is obtained.

4.1.3 Methods for SOTs efficiencies

In order to compare the SOT amplitudes in different systems, it is practical to define the SOT efficiency as a normalized parameter after considering the volume of the FM layer and current density[19]. The efficiency is given as follows

$$\xi_j^{DL,FL} = \frac{2e}{\hbar} M_s t_F \frac{B^{DL,FL}}{j}. \tag{4.9}$$

Here M_s is the saturation magnetization, t_F is the thickness of the magnetic layer, $\hbar$ is the reduced Planck constant, j is the injected current density obtained by dividing the current by the cross sectional area of the conductive layers. The current density applied to study the SOTs in the $Pt/Co/AlO_x$ and $Pt/CoO_x/Co/AlO_x$ series was 1.0×10^7 A/cm^2, which was calculated by dividing the total current by the width of the Hall bar and the sum of the thickness of the Pt and Co layers, 6 and 5.65 nm, respectively. For the $PtO_x/Co/AlO_x$ series, we applied a current of 1 mA, which corresponds to a current density of 1.7×10^6 A/cm^2 when considering both $PtO_x(5)$ and Co(1) as the conductive layers.

Because the current distribution is not expected to be homogeneous in samples made of different layers with varying degrees of oxidation, we also consider the SOT efficiency per unit electric field[136]

$$\xi_E^{DL,FL} = \frac{2e}{\hbar} M_s t_F \frac{B^{DL,FL}}{E} = \frac{2e}{\hbar} ML \frac{B^{DL,FL}}{SRI}. \tag{4.10}$$

Here E=ρj is the electric field (ρ is the resistivity). L is the length between two Hall crosses, S is the surface area of the samples for the magnetization measurements, R is the electrical resistance, and I is the current applied to the samples. $\xi_E^{DL,FL}$ can be easily calculated by knowing the total magnetic moment measured by superconducting quantum interference device and is therefore independent of t_F as well as on any assumption on the thickness of the conductive layers. When comparing samples with similar resistivity, it is equivalent to use either $\xi_j^{DL,FL}$ or $\xi_E^{DL,FL}$, which can be considered as an effective spin Hall angle and spin Hall conductivity, respectively. However, for samples with very different resistivities such as those belonging to the $PtO_x/Co/AlO_x$ series, the electric field normalization provides a better means of comparison.

4.2 Magneto-optical Kerr effect microscopy

MOKE can be used to image the magnetic domains of magnetic films and surfaces. In a MOKE setup, a linearly polarized beam from the polariser rotates its polarization plane after it is reflected by the magnetic surface. After the reflected light is filtered by the analyser, the CMOS camera measures the residual intensity of the light, which depends on the Kerr rotation as well as on the angle between polariser and analyser. The residual light intensity thus provides a map of the surface magnetization of the sample.

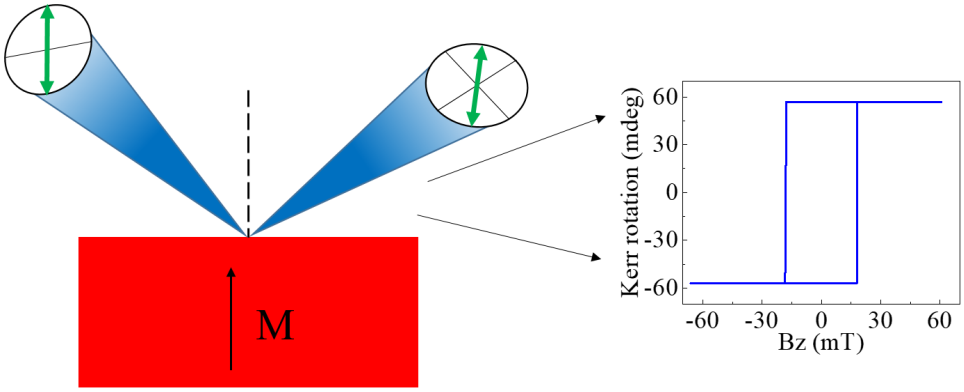

Figure 4.4 | Illustration of the polar Kerr effect. The black arrow indicate the magnetization direction. The angle between the two green arrows indicates the Kerr rotation. By sweeping the external magnetic field, a magnetic hysteresis loop can be obtained based on the Kerr rotation as shown on the right.

The incident polarized light is the combination of both the right-handed and left-handed circularly polarized beams. Without magnetic field or the influence of magnetic material, both the right- and left-handed beams are in phase and have the same amplitude. If both a net magnetization and spin-orbit coupling are present, the absorption of left- and right-circularly polarized light by the electronic bands of the sample becomes asymmetric, leading to different refractive indices for left- and right-circularly polarized light. Thus, the emerging beam has an ellipticity as well as a rotated plane of polarization compared with the original one, which is regarded as the Kerr rotation (See green arrows in Fig. 4.4). Depending on the sample magnetization, the plane of polarization of the light is rotated differently.

MOKE can be operated in different geometries. In the polar MOKE (Fig. 4.4), the magnetization direction is perpendicular to the sample surface, in the longitudinal MOKE, the magnetization direction is in-plane, whereas in the transverse MOKE, the magnetization direction is perpendicular to the scattering plane.

In this thesis, we use a home-built polar MOKE microscope to image the magnetic domains of the samples with perpendicular magnetic anisotropy. In this MOKE setup, we used an LED light source which emits blue light with wavelength 451 $\pm$ 24 nm. In an ideal system, the lateral resolution is only limited by the wavelength of the incident beam and the numerical aperture of the objective lens. In practice, the spatial resolution of our home-built MOKE is around 350 nm. Both in-plane (up to 30 mT) and out-of-plane (up to 46 mT)

magnetic fields can be applied to the samples. During the measurements, we firstly take the initial state as the background, then take the difference between the background and the changed state after applying the current pulses and/or magnetic fields in order to characterize the magnetization changes.

4.3 High resolution magnetic force microscopy

An MFM is a type of scanning probe microscope that is used for the measurement of the tip-sample forces mediated by the magnetic field. Compared with other surface probe methods such as the atomic force microscope, MFM utilizes a magnetized tip, which is sensitive to the magnetic field coming from the sample of interest.

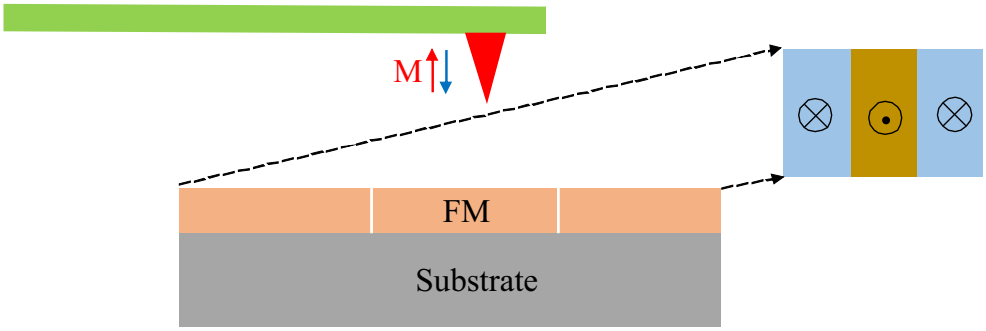

Figure 4.5 | Schematics of the MFM. During the measurements, the cantilever scans the whole region of interest. The red and black arrows indicate the magnetization direction of the magnetic tip. As the force between tip and magnetic domains with up and down magnetization are different, magnetic domains with different stray fields (magnetizations) can be imaged as shown in the right.

The signal obtained from the MFM includes all the forces acting on the magnetized tip:

$$F_{\mathrm{MFM}} = F_{\mathrm{cap}} + F_{\mathrm{vdW}} + F_{\mathrm{atom}} + F_{\mathrm{mag}} \tag{4.11}$$

Here, $\mathrm{F_{cap}}$ is the capacitive force given by the derivative of the energy stored in the capacitor that is formed by the MFM tip and the sample. $\mathrm{F_{vdW}}$ is the van der Waals force between the sample and the tip. $\mathrm{F_{atom}}$ is the interatomic force due to the overlap of the electronic wave functions of the tip and sample. $\mathrm{F_{mag}}$ is the magnetic force between the magnetic moment of the tip and the stray field produced by the distribution of magnetic moments or currents in the sample. The MFM measurement in this thesis were performed by PhD student Yaoxuan

Feng in Prof. Hans J. Hug's group at EMPA. During the measurements, we firstly used a permanent magnet to magnetize the MFM tip with the magnetization up (Fig. 8.2 red arrow), then measured the first scan. After that, we magnetized the tip down (Fig. 8.2 blue arrow), then measured the second scan. Compared with the first scan, F_{mag} is negative, whereas other forces are the same. Therefore, we can take the difference between the first and the second scans, which is due to F_{mag} only, to obtain the stray field information.

Due to the small magnitude of the magnetic force and its decay with increasing distance from the sample, measuring close to the sample surface improves the signal to noise ratio. On the other hand, the probe should not get too close to the sample as spatial variations of the van der Waals forces may dominate the signal. An average tip-sample distance between about 5 and 20 nm is preferred. These requirements imply the need for an accurate tip sample distance control. To achieve this, Prof. Hans J. Hug's group developed a new single-passage capacitive tip-sample distance control method and operated the MFM measurement with a sensitive distance control mode in vacuum. These improvements provided an MFM instrument with very high spatial resolution, which in theory could be a few angstroms.

5 Effects of oxidation on the electrical and magnetic properties of Pt/Co/AlO_x

In this chapter, I will present the electrical and magnetic properties of the three Pt/Co/AlO_x systems characterized in Chapter 3. Among the magnetic properties, I will focus on the saturation magnetization, anomalous Hall effect, and effective anisotropy field.

5.1 Electrical resistance

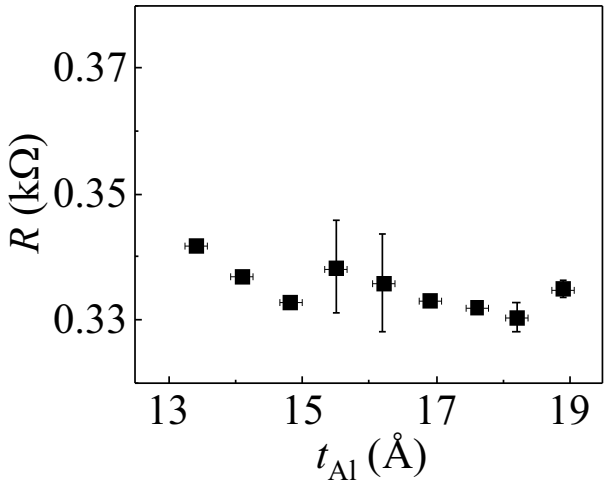

Figure 5.1 | 4-point resistance as a function of t_{Al} in Pt/Co/AlO_x. Vertical error bars represent the standard deviation of the average of different devices from the same series; horizontal error bars represent the uncertainty of the thickness calibration.

Figure 5.1 shows that the typical device resistance of Pt/Co/AlO_x is 0.33-0.34 kΩ, which corresponds to a resistivity of 40-41 $\mu\Omega$·cm by assuming that only Pt and Co are conductive. This assumption is corroborated by the weak dependence of the resistance on t_{Al}, which shows that the oxidation state of the top Co/Al interface does not influence significantly the conductivity of these layers.

Devices belonging to the Pt/CoO_x/Co/AlO_x series have a resistance of 0.35-0.36 kΩ, which corresponds to a resistivity of 40-41 $\mu\Omega$cm. Also in this case we assume that only Pt and Co are conductive. Note that the resistance is approximately constant as a function of t_{CoO_x}, suggesting that CoO_x is effectively

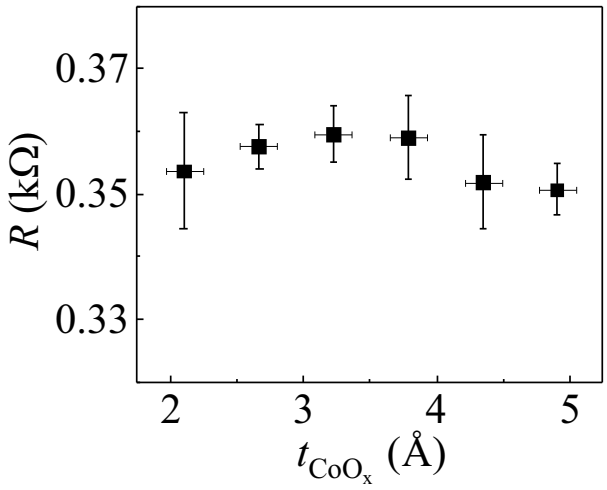

Figure 5.2 | 4-point resistance as a function of t_{CoO_x} in $Pt/CoO_x/Co/AlO_x$. Vertical error bars represent the standard deviation of the average of different devices from the same series; horizontal error bars represent the uncertainty of the thickness calibration.

an insulator (Figure 5.2).

From these two sets of data we conclude that the oxidation of the Co/Al and Pt/Co interfaces does not have a major impact on the resistivity, indicating that conduction is dominated by the 5 nm-thick Pt channel.

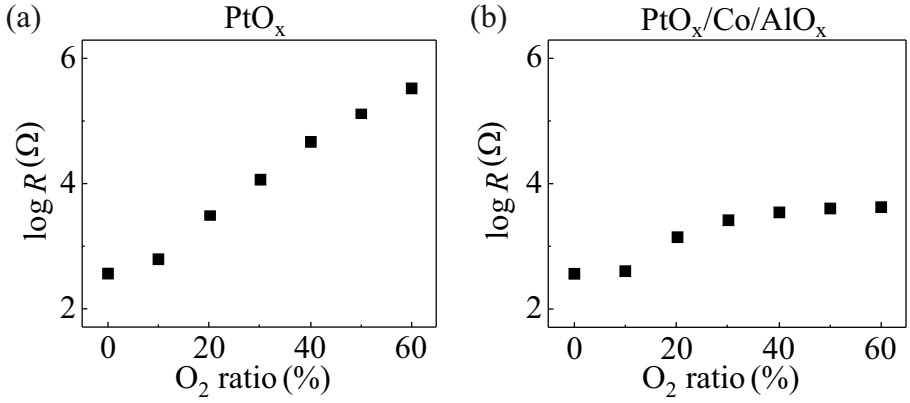

Figure 5.3 | 4-point resistance as a function of oxygen ratio in (a) PtO_x single layers and (b) $PtO_x/Co/AlO_x$.

The resistances of the reference PtO_x layers are shown in Figure 5.3 as a function of O_2:(Ar+O_2) ratio. The resistance of PtO_x increases dramatically with increasing O_2 ratio (note the log scale of the plot), indicating that PtO_x becomes nearly insulating for 50-60% of O_2. These results are consistent with

the conclusions drawn from the XPS spectra presented in Chapter 3. In contrast with the reference PtO_x layers, the resistance of $PtO_x/Co/AlO_x$ saturates around 40% of O_2 rather than increasing monotonically with O_2 ratio, to a value that is about two orders of magnitude lower compared to PtO_x single layers. These findings corroborate the oxygen diffusion scenario outlined in Chapter 3.

5.2 Saturation magnetization

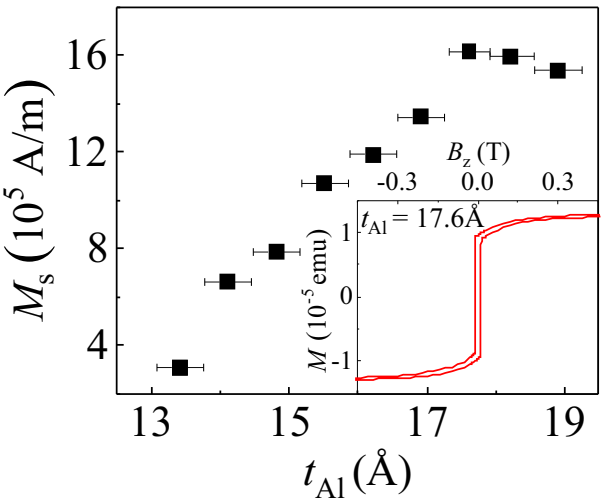

Figure 5.4 | Saturation magnetization as a function of t_{Al} in $Pt/Co/AlO_x$. The inset shows the total magnetic moment of $Pt/Co/AlO_x$ with t_{Al} = 17.6 Å as a function of out-of-plane external field. Horizontal error bars represent the uncertainty of the thickness calibration.

We measured the total magnetic moment of each sample using superconducting quantum interference device (SQUID) magnetometry in an out-of-plane external field (see inset of Fig. 5.4 for an example of a magnetization curve). The saturation magnetization M_s is obtained by dividing the saturation magnetic moment by the nominal volume of the Co layer, which corresponds to a thickness of 1 nm, 0.65 nm, and 1 nm of Co for the $Pt/Co/AlO_x$, $Pt/CoO_x/Co/AlO_x$, and $PtO_x/Co/AlO_x$ series, respectively.

In $Pt/Co/AlO_x$, M_s increases with increasing t_{Al} until it saturates around t_{Al} = 17.6 Å (Fig. 5.4). This behavior is consistent with the formation of CoO with antiferromagnetic correlations below t_{Al} = 17.6 Å and the metallic character of Co evidenced by XPS at and above this thickness.

In $Pt/CoO_x/Co/AlO_x$, we observe a monotonic decrease of M_s as a function of t_{CoO_x} (Fig. 5.5), which we ascribe to several factors. First, some of the

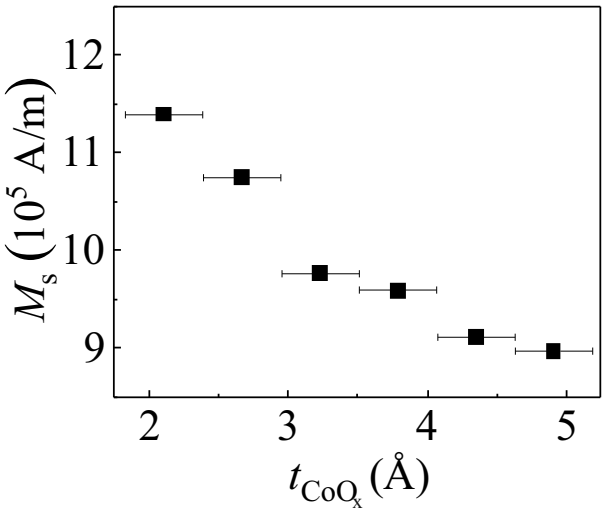

Figure 5.5 | Saturation magnetization as a function of t_{CoO_x} in $Pt/CoO_x/Co/AlO_x$. Horizontal error bars represent the uncertainty of the thickness calibration.

oxygen initially present in CoO_x most likely diffused into the metallic Co part, thus reducing M_s. Since the total amount of oxygen is proportional to t_{CoO_x} and t_{Co} is fixed, we expect that oxygen diffusion becomes more pronounced with increasing t_{CoO_x}. Second, the formation of a CoO_x layer between Pt and Co strongly reduces the proximity magnetization in Pt, which would contribute to reducing M_s, albeit with a weaker dependence on thickness beyond $t_{CoO_x} \approx 2$ Å.

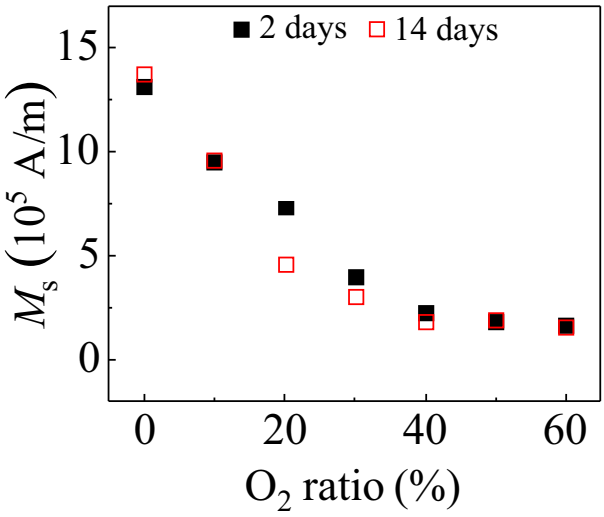

Figure 5.6 | Saturation magnetization as a function of O_2:Ar ratio in $PtO_x/Co/AlO_x$. The data shown as solid and open symbols were obtained, respectively, 2 and 14 days after the deposition of $PtO_x/Co/AlO_x$.

Finally, Fig. 5.6 shows M_s of $PtO_x/Co/AlO_x$ as a function of the O_2 ratio. For this series, we observe that M_s decreases by about a factor 7 as the O_2 ratio increases from 0 to 40% and beyond. This trend is consistent with the significant diffusion of oxygen into the Co layer evidenced by XPS as well as with the resistance measurements presented above. Moreover, as diffusion is a rather slow process, we may expect that the sample properties change over time. To verify this point, we have measured the M_s of $PtO_x/Co/AlO_x$ 2 and 14 days after growth, as shown by the solid and open symbols in Fig. 5.6, respectively. We find that M_s has changed slightly, particularly for intermediate oxidation ratios (20-40%), demonstrating that diffusion can take up to several days before the oxidation profile of these samples is stabilized.

5.3 Anomalous Hall effect

When applying an out-of-plane magnetic field, there is a component of the Hall resistance which can not be neglected for FM. This component is the anomalous Hall effect resistance (R_{AHE}) due to the anomalous Hall effect (AHE). AHE occurs in solids with broken time-reversal symmetry, typically in a ferromagnetic phase, as a consequence of spin-orbit coupling[137]. AHE is the analogous of the Hall effect in magnetic samples[82,137]. It is called anomalous to distinguish it from the ordinary Hall effect (OHE) in nonmagnetic conductors. Compared with OHE which increases linearly with the external field, the AHE is proportional to M_z. R_H^ω signal due to AHE can be written as:

$$R_H^\omega = R_{AHE} M_z = R_{AHE} M_s cos\theta. \tag{5.1}$$

θ is the polar angle of the magnetization. As reported recently, AHE can be also influenced by the interface and oxidation effects[138–140].

The AHE was measured by using the harmonic Hall voltage detection method. For samples with PMA, the values of the anomalous Hall resistance coefficient R_{AHE} are given by the half difference of the first harmonic signal when the magnetization is up/down at zero external field. For samples possessing IMA, we swept the out-of-plane magnetic field up to 2.2 T and took the intercept of the linear fit of the first harmonic curve within the high field range as the R_{AHE}.

In the $Pt/Co/AlO_x$ series, similar to M_s, we find that R_{AHE} increases and then saturates as a function of t_{Al} (Fig. 5.7). This behavior shows that R_{AHE} depends on the volume fraction of metallic Co, which increases with increasing t_{Al}. Additionally, we observe that R_{AHE} approaches saturation faster than M_s,

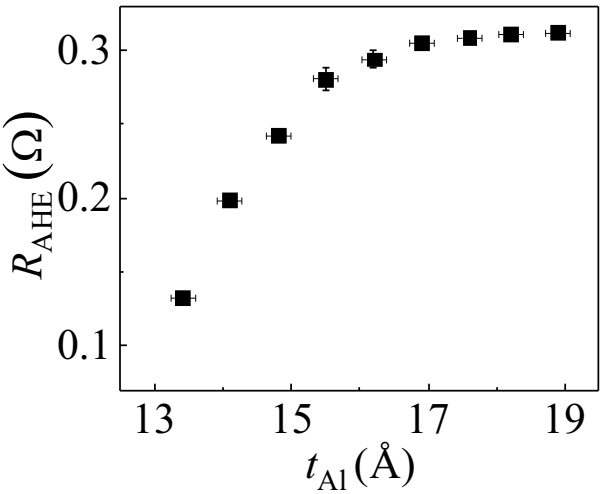

Figure 5.7 | Anomalous Hall resistance as a function of t_{Al} in $Pt/Co/AlO_x$. Vertical error bars represent the standard deviation of the average of different devices from the same series; horizontal error bars represent the uncertainty of the thickness calibration.

indicating that the AHE increases upon interfacial oxidation of Co, in agreement with previous work[141], which we attribute to the enhanced electron scattering at the Co/AlO_x interface.

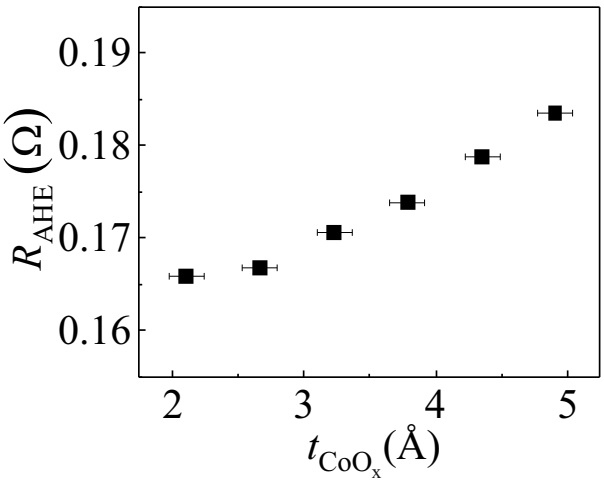

Figure 5.8 | Anomalous Hall resistance as a function of t_{CoO_x} in $Pt/CoO_x/Co/AlO_x$. Horizontal error bars represent the uncertainty of the thickness calibration.

Partial oxidation of Co appears to play a role in increasing R_{AHE} also in the $Pt/CoO_x/Co/AlO_x$ series. In samples with thicker CoO_x, we would expect that metallic Co partially oxidizes due to oxygen diffusion from the as-grown CoO_x layer, leading to a reduction of M_s and R_{AHE} with increasing t_{CoO_x}. Instead,

we find that R_{AHE} increases monotonically with t_{CoO_x} (Fig. 5.8). Although the relative change of R_{AHE} is small, this observation supports the conclusion that moderate oxidation of the Co interfaces, and possibly of the Co grain boundaries, enhances the AHE. These results are consistent with a previous study of the AHE in $MgO/(Co/Pt)_3/MgO$ multilayers, which evidenced an increase of R_{AHE} upon insertion of a CoO_x layer between MgO and Co[142]. In this study, the enhancement of R_{AHE} was attributed to the modified metal/oxide interfacial structures together with the improved crystallization of the core $(Co/Pt)_3$ multilayers.

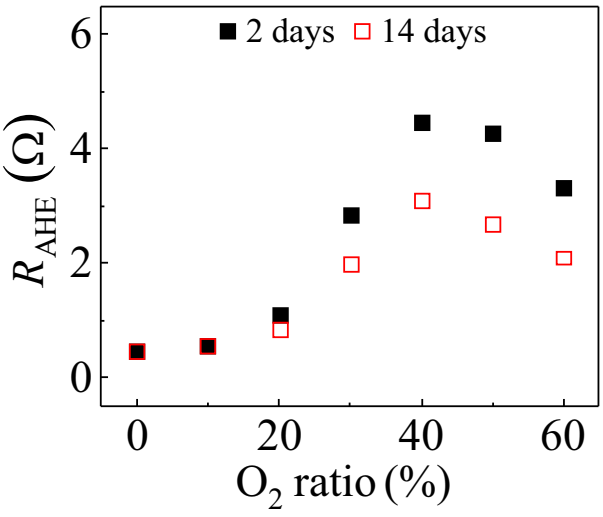

Figure 5.9 | Anomalous Hall resistance as a function of O_2:(O_2+ Ar) ratio in $PtO_x/Co/AlO_x$. The data shown as solid and open symbols was obtained, respectively, 2 and 14 days after the deposition of $PtO_x/Co/AlO_x$.

The strongest increase of R_{AHE}, by more than one order of magnitude, is found in $PtO_x/Co/AlO_x$. In this series, R_{AHE} reaches a maximum of 4.5 Ω around 40% O_2 ratio, compared to 0.3 Ω in $Pt/Co/AlO_x$, and decreases afterwards (Fig. 5.9). This nonmonotonic behavior suggests that, in the lower oxidation range (0-40%), the higher resistivity of Pt causes less current shunting and a larger current flow through Co, which is also partially oxidized, thereby increasing R_{AHE}. The turning point at 40% and successive decrease of R_{AHE} can then be attributed to the strong reduction of M_s that occurs with the progressive oxidation of Co. In this case, the difference between samples measured 2 and 14 days after deposition is substantial, which shows that changes in the oxidation profile influence the Hall conductivity more strongly than M_s.

5.4 Effective anisotropy field

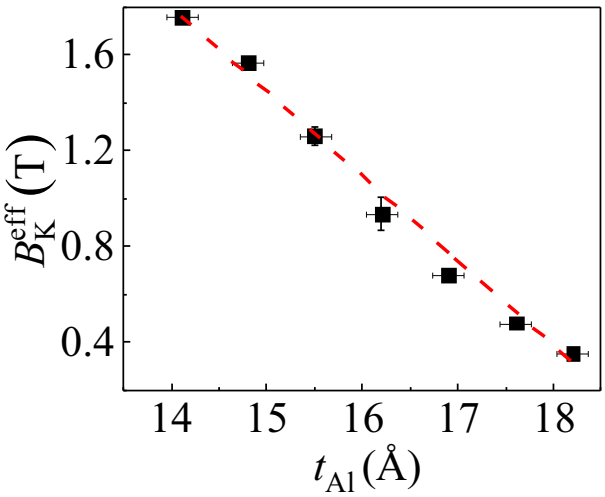

Figure 5.10 | Effective magnetic anisotropy field as a function of t_{Al} in $Pt/Co/AlO_x$. The dashed line is a linear fit of the data. Vertical error bars represent the standard deviation of the average of different devices from the same series; horizontal error bars represent the uncertainty of the thickness calibration.

Figure 5.10 shows B_K^{eff} as a function of t_{Al} in the $Pt/Co/AlO_x$ series. With increasing t_{Al}, B_K^{eff} decreases almost in a linear fashion from 1.7 T to 0.4 T (note that the magnetic anisotropy of samples with $t_{Al} > 18.2$ Å could not be measured due to the appearance of the in-plane magnetization component). This trend is consistent with the linear decrease of M_s reported before in the over-oxidized range (t_{Al} = 13.4-16.9 Å). In this range, the top and bottom interfaces do not change significantly and B_K^{eff} is mostly affected by the change of the demagnetizing field, which is directly proportional to M_s. In the optimally-oxidized and under-oxidized range (t_{Al} = 17.6-18.9 Å), M_s remains approximately constant, but the oxidation of the top Co interface leads to an increase of the PMA[143].

In the $Pt/CoO_x/Co/AlO_x$ series, B_K^{eff} remains close to 1.7 T in the entire CoO_x thickness range (Fig. 5.11), despite the moderate decrease of M_s as a function of t_{CoO_x} (Fig. 5.5). We attribute this behavior to the strong PMA induced by the CoO_x/Co interface, as suggested by previous studies[144,145].

The samples belonging to the $PtO_x/Co/AlO_x$ series have IMA. B_K^{eff} in this case was estimated by the magnetic field required to saturate the sample in the hard out-of-plane direction, as described in Ref. 40. Figure 5.12 shows B_K^{eff} as a function of the O_2 ratio measured 2 and 14 days after deposition. We identify two different regimes below and above 20% of O_2. B_K^{eff} decreases going from 0

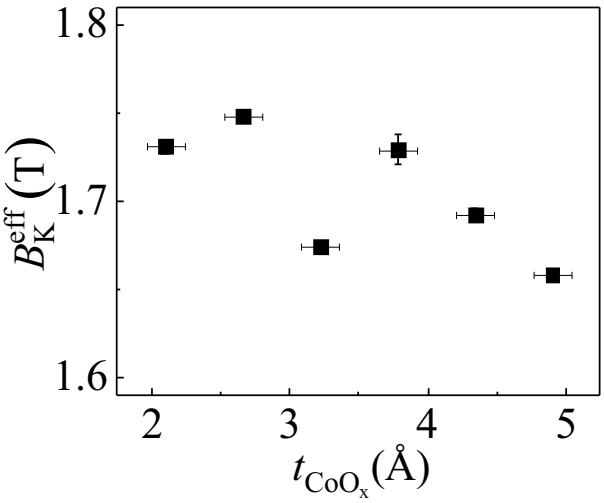

Figure 5.11 | Effective magnetic anisotropy field as a function of t_{CoO_x} in $Pt/CoO_x/Co/AlO_x$. Vertical error bars represent the standard deviation of the average of different devices from the same series; horizontal error bars represent the uncertainty of the thickness calibration.

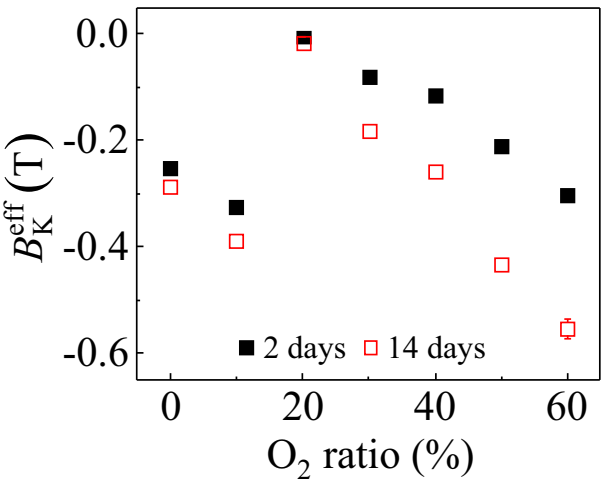

Figure 5.12 | Effective magnetic anisotropy field as a function of O_2 ratio in $PtO_x/Co/AlO_x$. The solid and open symbols refer to measurements carried out 2 and 14 days after the deposition, respectively.

to 10% O_2, presumably due to the oxidation of Pt at the Pt/Co interface at this low O_2 concentration. However, at 20% O_2 ratio B_K^{eff} suddenly approaches zero and then decreases again for larger O_2 ratios. One plausible explanation of this peculiar behavior is that oxygen diffuses through Co up to the Al interface with increasing O_2 ratio. At 20% O_2, the Co/Al interface is oxidized, leading to PMA and almost complete compensation of the demagnetizing field. Further increasing the O_2 ratio leads to a decrease of B_K^{eff} due to oxygen diffusing throughout the Co layer, as shown by the more pronounced decrease of B_K^{eff} after 14 days.

In this chapter, I studied the oxidation effects on the resistivity, saturation magnetization, anomalous Hall resistance, and magnetic anisotropy of $Pt/Co/AlO_x$, $Pt/CoO_x/Co/AlO_x$, and $PtO_x/Co/AlO_x$ heterostructures. The main conclusions we summarized as follows:

- In all samples, increasing levels of oxidation lead to a reduction of M_s due to the formation of CoO_x.
- R_{AHE} decreases with increasing oxidation in $Pt/Co/AlO_x$ but increases in $Pt/CoO_x/Co/AlO_x$ and $PtO_x/Co/AlO_x$, consistently with the AHE being influenced by the magnetic volume as well as by spin-dependent scattering at oxidized interfaces.
- The magnetic anisotropy is determined by the competition between the PMA of the Pt/Co and Co/Al interfaces and shape anisotropy. The latter scales as M_s and is strongly influenced by the oxidation of Co. In $Pt/Co/AlO_x$, B_K^{eff} decreases linearly with increasing t_{Al}, from 1.76 T to 0.36 T going from over-oxidized to under-oxidized Co/Al interfaces. Interestingly, the insertion of a thin CoO_x layer between Pt and Co results in very strong PMA of the $Pt/CoO_x/Co/AlO_x$ series, with $B_K^{eff} \approx 1.7$ T, which is nearly independent on t_{CoO}. Direct oxidation of Pt, on the other hand, leads to a reduction of the PMA in $PtO_x/Co/AlO_x$ compared to $Pt/Co/AlO_x$.

Overall, this set of data proves that the magnetic properties of Pt/Co/Al trilayers are extremely sensitive to the oxidation of both the top and bottom Co interfaces as well as to the oxygen concentration within the layers.

6 Effects of oxidation on the SOTs and switching properties of $Pt/Co/AlO_x$

In this chapter, I will present the SOTs and current-induced switching properties of the three $Pt/Co/AlO_x$ systems described in Chapter 3 and 5, using the methods introduced in Chapter 4.

6.1 Current-induced SOTs

In this section, we report not only $B^{DL,FL}$ but also the two SOT efficiencies $\xi_j^{DL,FL}$ and $\xi_E^{DL,FL}$ as a function of the 3 different oxidation variables.

6.1.1 $Pt/Co/AlO_x$

Here we consider the effect of changing t_{Al}, hence the oxidation of the Co/Al interface, in the $Pt/Co/AlO_x$ system. As shown in Fig. 6.1(a), the effective fields $B^{DL,FL}$ decrease monotonically as a function of t_{Al}. This decrease mostly reflects the increase of M_s as the Co layer changes from over- to under-oxidized. Accordingly, the SOT efficiencies show a weaker dependence on t_{Al}. $\xi_j^{DL,FL}$ and $\xi_E^{DL,FL}$ decrease slowly up to $t_{Al} = 16.9$ Å, and then increase rather abruptly from $t_{Al} = 16.9$ to 17.6 Å [Fig. 6.1(b,c)]. As the latter thickness corresponds to the optimal oxidation of the Co/AlO_x interface, we attribute the local maxima of $\xi_j^{DL,FL}$ and $\xi_E^{DL,FL}$ to the enhancement of the charge transfer and ensuing interfacial electric field between the Co and AlO_x layers. We note that this enhancement affects both the damping-like and field-like components of the SOT, as expected from the spin current contributions originating from spin-orbit coupling and spin-dependent scattering at interfaces[146–148]. Moreover, the larger SOT efficiencies found for the optimized samples are consistent with the larger torkances (torques per unit electric field and unit magnetization) calculated ab-initio for Pt/Co/O relative to Pt/Co/Al[149].

The sign of the field-like SOT is such that B^{FL} opposes the Oersted field generated by the current flowing the Pt layer. ξ_j^{DL} (ξ_j^{FL}) and ξ_E^{DL} (ξ_E^{FL}) peak at 0.14 (0.08) and 3.5 (2.1) $\times 10^5\,(\Omega m)^{-1}$, which compares well with the SOT efficiencies reported in previous studies of optimized $Pt/Co/AlO_x$[23]. Interestingly, these SOT efficiencies are consistently larger than those reported for Pt(5)/Co(1)/MgO(2), where ξ_j^{DL} (ξ_j^{FL}) = 0.11 (0.024) and ξ_E^{DL} (ξ_E^{FL}) = 2.43

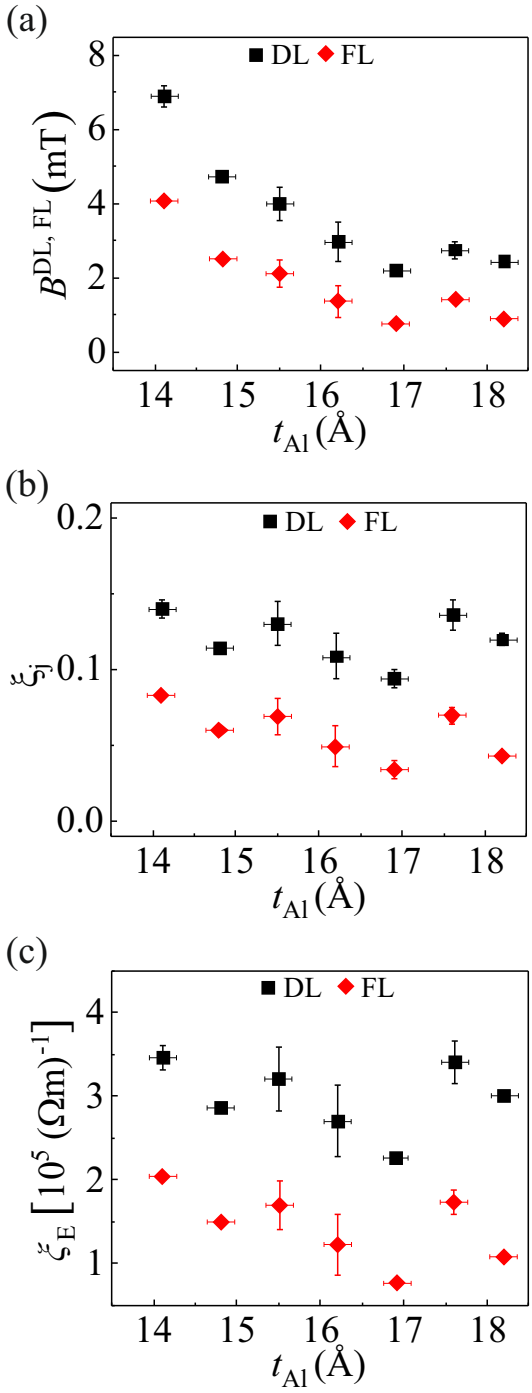

Figure 6.1 | (a) $B^{DL,FL}$, (b) $\xi_j^{DL,FL}$ and (c) $\xi_E^{DL,FL}$ as a function of t_{Al} in Pt/Co/AlO$_x$. The current density is 1.0×10^7 A/cm^2 as obtained by considering the nominal thickness of the Pt and Co layers. B^{Oe} is included in the FL data shown here. Vertical error bars represent the standard deviation of the average of different devices from the same series; horizontal error bars represent the uncertainty of the thickness calibration.

$(0.53) \times 10^5\,(\Omega m)^{-1}$ [136]. Such a difference might be related to the different band alignment between Co and either AlO_x or MgO, leading to different interfacial electrical fields and scattering properties.

6.1.2 $Pt/CoO_x/Co/AlO_x$

Inserting a 2.1 Å thick CoO_x layer between Pt and Co leads to an enhancement of the SOT effective fields and efficiencies by about a factor 2 compared to the optimized $Pt/Co/AlO_x$ trilayer (Fig. 6.2). This remarkable result indicates that the Pt/CoO_x and CoO_x/Co interfaces are very efficient in transferring spins from Pt to Co. Given that the Néel and blocking temperatures of CoO are well below room temperature in films thinner than 10 nm [150], the spin transfer across the insulating CoO_x layer is likely mediated by antiferromagnetic spin fluctuations, as found for the reciprocal effect of spin pumping in $Y_3Fe_5O_{12}/NiO/Pt$ and $Y_3Fe_5O_{12}/CoO/Pt$ trilayers [151,152]. Differently from these studies, however, here the FM layer is metallic and the spin current flows towards the FM, which is extremely promising for the efficient manipulation of the magnetization by an electric current. Additionally, we find that $\xi_j^{DL,FL}$ and $\xi_E^{DL,FL}$ decrease upon increasing the thickness of the CoO_x layer, consistently with diffusive spin transport mediated by correlated spin fluctuations [151]. Such a decrease shows that a significant fraction of the spin current giving rise to the SOTs originates from either the Pt or the Pt/CoO_x interface. However, we also observe that $\xi_j^{DL,FL}$ and $\xi_E^{DL,FL}$ tend to saturate towards finite values rather than tending to zero, which may indicate that the CoO_x/Co interface also contributes to generating a spin current [146–148]. Overall, these results indicate that the insertion of a thin paramagnetic CoO_x layer significantly improves the charge-spin conversion efficiency of HM/FM/Ox structures at a very small cost in terms of material engineering, consistently with recent reports [153,154].

6.1.3 $PtO_x/Co/AlO_x$

The oxidation of Pt leads to a very different behavior compared to the oxidation of Co. Figure 6.3 shows the SOT effective fields and efficiencies measured 2 days (full symbols) and 14 days (open symbols) after deposition of the $PtO_x/Co/AlO_x$ series. Note that the values of $B^{DL,FL}$ at 0% O_2 ratio, i.e., for unoxidized Pt, are lower than reported for $Pt/Co/AlO_x$ because the current density employed in these measurements was about a factor 6 smaller compared to the $Pt/Co/AlO_x$ series, whereas $\xi_j^{DL,FL}$ and $\xi_E^{DL,FL}$ are comparable. We recall also that changing

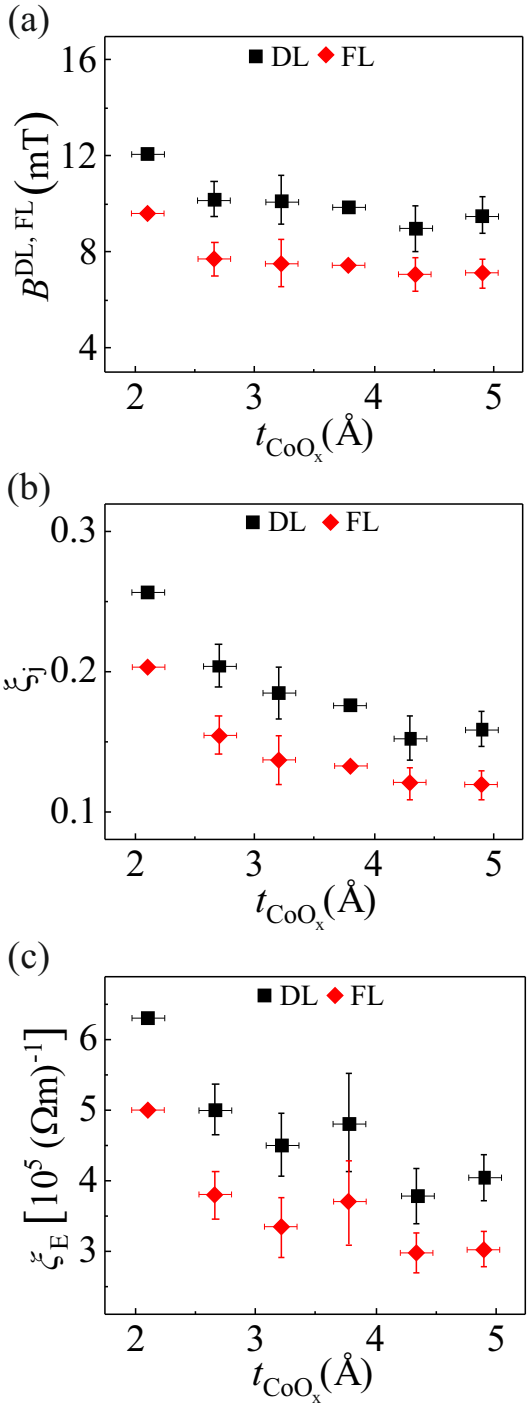

Figure 6.2 | (a) $B^{DL,FL}$, (b) $\xi_j^{DL,FL}$ and (c) $\xi_E^{DL,FL}$ as a function of t_{CoO_x} in Pt/CoO$_x$/Co/AlO$_x$. The current density applied for the Pt/CoO$_x$/Co/AlO$_x$ system is 1.0×10^7 A/cm^2 by considering the nominal thickness of the Pt and Co layers. B^{Oe} is included in the FL data shown here. Vertical error bars represent the standard deviation of the average of different devices from the same series; horizontal error bars represent the uncertainty of the thickness calibration.

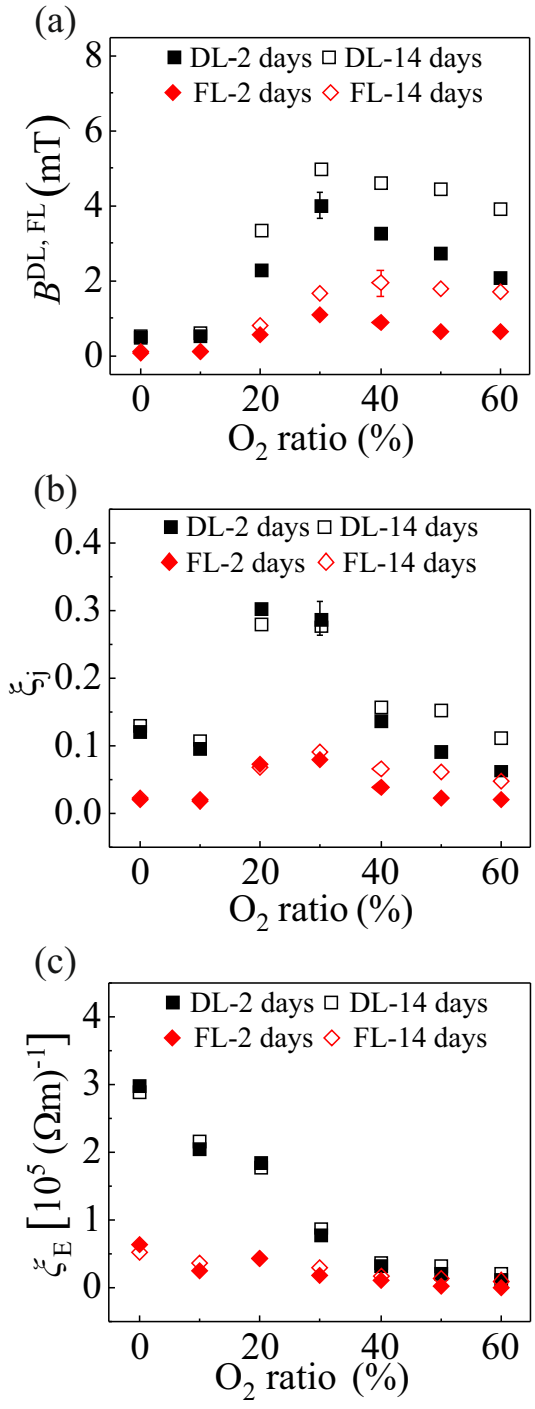

Figure 6.3 | (a) $B^{DL,FL}$, (b) $\xi_j^{DL,FL}$ and (c) $\xi_E^{DL,FL}$ as a function of O_2 : (O_2 + Ar) ratio in $PtO_x/Co/AlO_x$. For the $PtO_x/Co/AlO_x$ series, we applied a current of 1 mA, which corresponds to a current density of 1.7×10^6 A/cm^2 when considering both $PtO_x(5)$ and Co(1) as the conductive layers. B^{Oe} is included in the FL data shown here. The data shown as solid and open symbols were obtained, respectively, 2 and 14 days after the deposition of $PtO_x/Co/AlO_x$. Vertical error bars represent the standard deviation of the average of different devices from the same series.

the O_2 ratio from 0 to 30% O_2 leads to about a 10-fold increase of the resistance and R_{AHE} as well as to a 3-fold decrease of M_s. The samples of these series have IMA, the strength of which varies with the O_2 ratio.

Figure 6.3(a) shows that $B^{DL,FL}$ increase first by about a factor 10 as the O_2 ratio reaches 30% and then decrease by an amount that depends on the time elapsed between the deposition and the measurements. Samples measured 20 days after deposition show the same SOTs compared with the measurement done after 14 days, suggesting that the oxidation profiles becomes stable after several days. The initial increase of $B^{DL,FL}$ is partly assigned to the reduction of M_s, as shown by the comparatively smaller change of $\xi_j^{DL,FL}$ [Fig. 6.3(b)]. ξ_j^{DL} and ξ_j^{FL} peak at 0.30 and 0.07, respectively, close to 20% O_2 ratio. Our XPS measurements, however, show that Pt is not significantly oxidized at this ratio, as oxygen migrates towards the Co and Al layers. Further, measurements of the magnetic anisotropy suggest that, at around 20% O_2 ratio, oxygen reaches the Co/Al interface. It is therefore likely that the peak of $\xi_j^{DL,FL}$ reflects a change of the current distribution in the $PtO_x/Co/AlO_x$ layers rather than a true increase of the SOT efficiency. For example, if oxygen from the topmost part of the PtO_x layer migrates towards Al, most of the current will flow close to the Pt/Co interface, leading to an apparent increase of $\xi_j^{DL,FL}$. We recall that, for consistency between different samples, $\xi_j^{DL,FL}$ is calculated by assuming a constant cross-section for current flow, i.e., the total thickness of the PtO_x and Co layers.

Further insight into the dependence of the SOT on the O_2 ratio can be gained by analyzing the behavior of $\xi_E^{DL,FL}$, which does not depend on the current distribution. Figure 6.3(c) shows that $\xi_E^{DL,FL}$ decreases monotonically with increasing O_2 ratio. Specifically, ξ_E^{DL} starts at 2.98×10^5 $(\Omega m)^{-1}$ at 0% O_2 and reaches 0.13×10^5 $(\Omega m)^{-1}$ at 60% O_2; ξ_E^{FL} shows a similar decreasing trend, from 0.63×10^5 $(\Omega m)^{-1}$ to 0.01×10^5 $(\Omega m)^{-1}$. According to Eq. 4.10, for measurements performed at constant current, $\xi_E^{DL,FL} \propto B^{DL,FL} M_s/R$. The strong decrease of $\xi_E^{DL,FL}$ is thus ascribed to the increase of R and reduction of M_s that occur upon augmenting the O_2 ratio.

Our results are in stark contrast with previous work carried out on $PtO_x/Ni_{81}Fe_{19}/SiO_2$ trilayers[46,47], in which both $\xi_j^{DL,FL}$ and $\xi_E^{DL,FL}$ were found to increase monotonically with O_2 ratio, up to ξ_j^{DL} $(\xi_j^{FL}) = 0.92$ (0.19) and ξ_E^{DL} $(\xi_E^{FL}) = 8.7$ (1.8) $\times 10^5$ $(\Omega m)^{-1}$ at 100% O_2. In the following, we discuss possible reasons for this discrepancy. First, the FM and cap layers are different, which may result in significant differences in both oxygen diffusion and oxidation profile as well as in

the generation and transmission of spin currents at interfaces. Second, the measurements of $B^{DL,FL}$ in Refs. 46, 47 were performed by spin-torque ferromagnetic resonance (FMR) and by measuring the broadening of the FMR lineshape upon dc current injection. The current and field normalizations required to calculate $\xi_j^{DL,FL}$ and $\xi_E^{DL,FL}$ in Refs. 46, 47 were carried out by assuming current flow in the $Ni_{81}Fe_{19}$ layer only and constant resistance, respectively. The current normalization affects the absolute value of $\xi_j^{DL,FL}$, but would not induce a different trend as a function of O_2 ratio compared to ours, since we also assume a constant cross section for the current. The field normalization required to calculate $\xi_E^{DL,FL}$ is more critical, since the resistance increases continuously as a function of O_2 ratio in $PtO_x/Ni_{81}Fe_{19}/SiO_2$[47]. However, even assuming a constant resistance, we do not observe a monotonous increase of $\xi_E^{DL,FL}$. We also note that assumptions on the distribution of the current as well as on the different contributions to the FMR lineshape can significantly affect the determination of the effective fields by spin-torque FMR[155]. Finally, no hints of post-deposition oxygen diffusion or changes of M_s were reported for either $PtO_x/Ni_{81}Fe_{19}/SiO_2$ or $PtO_x/CoTb/MgO$[46,47], but also not specifically analyzed, which prevents a more stringent comparison with our results.

6.2 Current-induced switching

By increasing the current density beyond a critical threshold $j_c \approx 10^7 - 10^8$ A/cm^2, the SOT become large enough to reverse the magnetization of trilayers with strong PMA, such as $Pt/Co/AlO_x$[17,156], Pt/Co/MgO[92], Ta/CoFeB/MgO[90,157], and $Pt/[Co/Ni]_N/Al$[158]. Magnetization reversal is driven by the damping-like torque[17]; the field-like torque, which is equivalent to a hard axis field, facilitates the switching by lowering the energy barrier for domain nucleation and propagation[18,80,159]. As the damping-like torque is perpendicular to both the current direction and the normal to the plane, an in-plane external field B_x parallel to the current is required in order to break the symmetry of the system and determine the polarity of the switching[7,17]. In the macrospin approximation, the critical switching current is given by[160]

$$j_c^{\mathrm{MS}} = \frac{2e}{\hbar}\frac{M_s t_{\mathrm{Co}}}{\xi_j^{DL}}\left(\frac{B_K^{eff}}{2} - \frac{B_x}{\sqrt{2}}\right). \tag{6.1}$$

Although SOT-driven magnetization switching in structures with lateral dimensions larger than about 20 nm occurs by nucleation and expansion of magnetic

domains[37,80,95,106,161], this expression provides a useful starting point to evaluate the dependence of j_c on critical material parameters.

In realistic systems, j_c depends on the parameters appearing in Eq. (6.1) as well as on the Dzyaloshinskii–Moriya interaction, domain pinning field, device geometry, size, temperature, and duration of the current pulses[80,156,162–167]. The temperature, which is determined by the current distribution as well as by the thermal conductivity of the different materials in the stack, plays a major role, both in activating the switching as well as in changing critical parameters such as M_s, B_{K}, and ξ_j^{DL} during switching. These factors vary significantly, even among nominally similar material systems reported in the literature[7], so that a comparative study of the critical switching current versus, e.g, magnetic anisotropy or SOT efficiency is hard to achieve. Here we use the controlled oxidation of the top Co interfaces in $Pt/Co/AlO_x$ in order to investigate such effects.

Figure 6.4(a) shows the switching of the out-of-plane magnetization of $Pt/Co/AlO_x$ with $t_{\mathrm{Al}} = 18.2$ Å measured by the change of the anomalous Hall resistance during a sweep of a dc current in the presence of a constant field $B_x = +70$ mT. The curve represents the normalized signal $M_z = R_H^{\omega}/R_{AHE}$, where R_H^{ω} is the first harmonic Hall resistance. The critical switching current density is defined as the current for which $M_z = 0$.

As seen in Chapter 5, reducing the oxidation of the top Co interface increases M_s and decreases B_K^{eff} by about a factor 4, whereas ξ_j^{DL} changes by about 40% depending on t_{Al}. According to Eq. (6.1), j_c depends linearly on each of these parameters. Note that j_c for the samples with higher B_K^{eff} are not reported because these samples cannot be fully switched before they are damaged by the current. We find that j_c scales linearly with j_c^{MS}, the theoretical current density calculated using Eq. 6.1 [Fig. 6.4(b)]. However, j_c is about one order of magnitude smaller than j_c^{MS}, which is reasonable since Eq. 6.1 does not take temperature effects into account and switching by domain nucleation and propagation requires less energy compared to macrospin reversal. Fig. 6.4(c) shows that the factor that mostly affects j_c is the strength of the magnetic anisotropy, as seen by the close linear scaling of j_c with B_K^{eff}.

In this chapter, I studied the oxidation effects on B^{SOTs}, ξ_j^{SOTs} and ξ_E^{SOTs} of $Pt/Co/AlO_x$, $Pt/CoO_x/Co/AlO_x$, and $PtO_x/Co/AlO_x$ heterostructures as well as the current-induced switching properties of $Pt/Co/AlO_x$. The main conclusions we summarized as follows:

- Oxidation of the Co/Al top interface influences the SOT efficiencies, leading to a 21% and 42% variation of the damping-like and field-like SOT

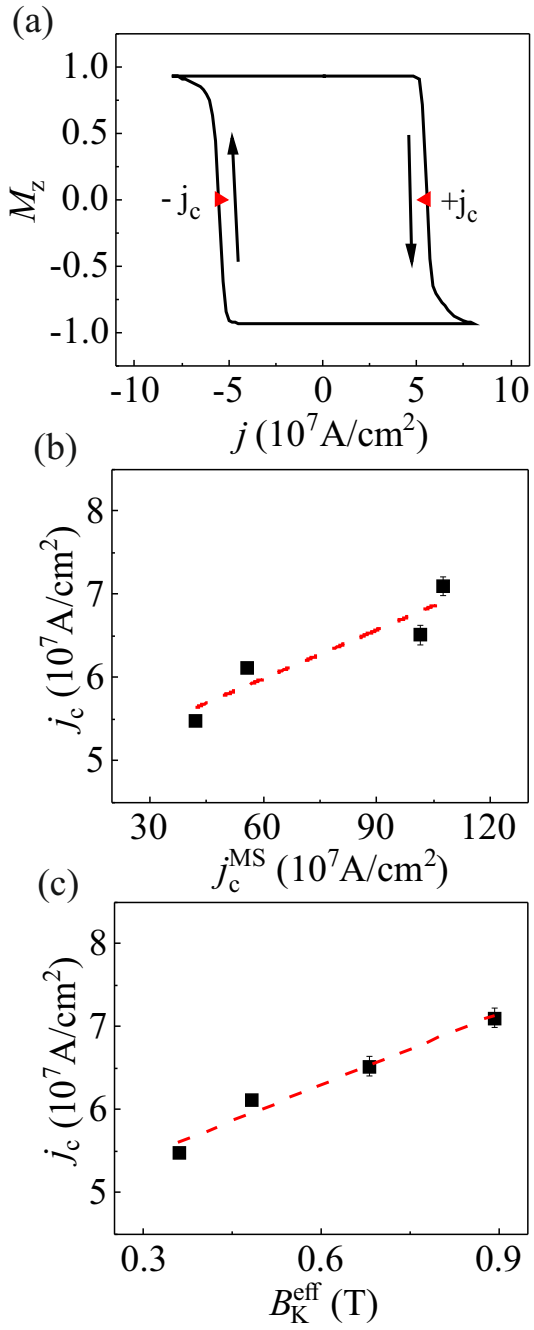

Figure 6.4 | (a) Out-of-plane component of the magnetization $M_z = R_H^{\omega}/R_{AHE}$ of Pt/Co/AlO$_x$ as a function of dc current density during a switching measurement with $B_x = +70$ mT. The red triangles show the points that define j_c. (b) j_c versus j_c^{MS} calculated using Eq. 6.1 for the of Pt/Co/AlO$_x$ series. (c) j_c as a function of B_K^{eff}. The lines represent linear fits to the data. Vertical error bars represent the standard deviation of the average of different devices from the same series.

efficiencies, which peak at 0.14 and 0.07, respectively.

- The insertion of an ultrathin paramagnetic CoO_x layer between Pt and Co enhances the SOT efficiency by up to 100% as CoO_x likely enhances the transmission of the spin current generated by the Pt layer and Pt/CoO_x interface[151–154], additionally, the CoO_x/Co interface generates an additional spin accumulation that is independent of t_{CoO_x}.

- The metastable PtO_x does not enhance the SOT efficiency of PtO_x/ Co/AlO_x, which is in stark contrast with the SOT efficiency reported in Refs. 46, 47.

- The critical current density required to switch the magnetization of the Co layer scales linearly with the theoretical current density calculated using the macrospin approximation, but is smaller by about one order of magnitude. The critical current density of $Pt/Co/AlO_x$ is also found to depend linearly on B_K^{eff}, which is determined by the degree of oxidation of the Co/Al interface.

7 Effects of oxidation on the domain textures

In this chapter, we study the influence of oxidation on the magnetic textures that form upon magnetic field- and current-induced magnetization reversal. We first present the Pt/Co/AlO_x samples chosen for this investigation. Second, we introduce the MOKE measurement protocol. Finally, we study the magnetization reversal process and the formation of different magnetic textures of representative samples with different oxidation levels.

7.1 Samples

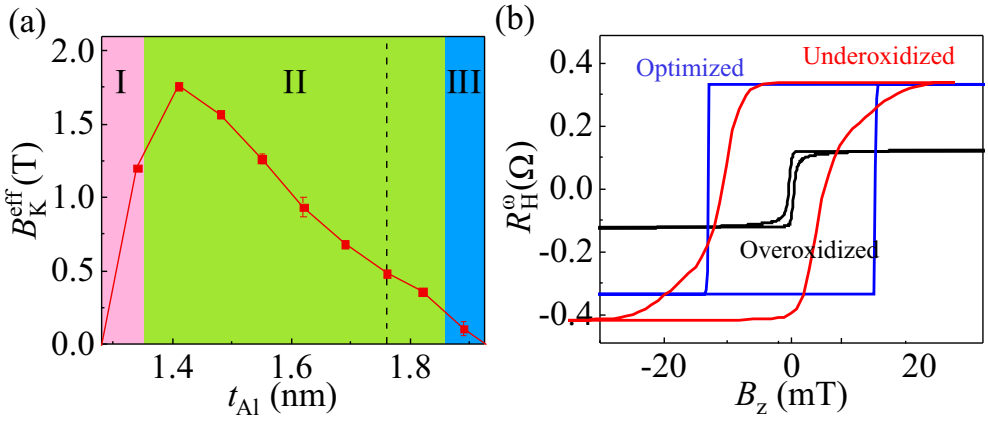

Figure 7.1 | (a) B_K^{eff} as a function of Al thickness in Pt/Co/AlO_x trilayers with PMA. The diagram is divided into regions I , II and III according to the different domain textures and behaviour under magnetic field and current pulses. The sample with t_{Al} = 1.76 nm indicated by the vertical dashed line is the "optimized" sample as defined in Chapter 3. Vertical error bars represent the standard deviation of the average of different devices from the same series. (b) R_ω^H as a function of the out-of-plane magnetic field B_z. The hysteresis loops of the three representative "overoxidized", "optimized" and "underoxidized" samples in region I, II and III are drawn in black, blue and red, respectively.

We investigate the Pt/Co/AlO_x wedge samples described in Chapter 3 to explore the role of oxidation effects on the domain formation and propagation upon magnetization reversal. The effective anisotropy field B_K^{eff} of the Pt/Co/AlO_x wedge is shown in Fig. 7.1(a) as a function of t_{Al}. For samples with t_{Al} = 1.89 nm

and 1.34 nm, B_K^{eff} was estimated by the field at which the M_x magnetization saturates ($M_z = 0$), using the method described in Ref. 32 as the PMA is weak. B_K^{eff} of the other samples was estimated by using the method described in Chapter 4.

The behaviour of B_K^{eff} as a function of t_{Al} shows a typical "volcano" shape, which reflects the influence of the interfacial oxidation on the magnetic anisotropy of Co. The sample with 1.41 nm Al has the highest B_K^{eff}. For $t_{Al} < 1.41$ nm, B_K^{eff} drops rapidly with decreasing thickness. For $t_{Al} > 1.41$ nm, the increase of thickness results in a decrease of B_K^{eff}. For a detailed explanation of this trend, please refer to Chapter 5. Note that the sample with $t_{Al} = 1.34$ nm exhibits both in-plane and out-of-plane magnetization components as the remanence is not 100% at $B_z = 0$.

According to the domain textures found in the experiment (see section 7.3), we classify the samples of Fig. 7.2(a) in three regions, which we label as overoxidized (I), optimized (II) and underoxidized (III). The magnetic hysteresis loops of representative "overoxidized", "optimized" and "underoxidized" $Pt/Co/AlO_x$ samples are shown in Fig. 7.1(b). The oxidation state of the Co layer in each sample is verified by XPS measurements as described in Chapter 3. In section 7.3, we present wide-field MOKE measurement showing the domain nucleation and expansion under magnetic field and current pulses in representative samples of these three regions.

7.2 MOKE measurement protocol

MOKE measurements are performed in differential mode, i.e., the changes of magnetization are captured by taking the difference between an image and a reference image corresponding to a uniformly magnetized state or a pre-set domain pattern. To take the reference image, we first saturate the magnetization up (down) by applying an out-of-plane magnetic field B_z = + (-) 46 mT. Then, we set the magnetic field to zero or a value that depends on the sample under investigation and acquire the reference image. A differential MOKE image of a Hall bar device is shown in Fig. 7.2. Positive (negative) current j is injected along the + (-) x axis. Dark contrast indicates that the magnetization points up, light grey contrast indicates that the magnetization points down.

7.3 Nucleation and growth of magnetic domains

In this section, we investigate the field- and current-induced domain nucleation and growth by MOKE microscopy in representative samples of regions I, II and

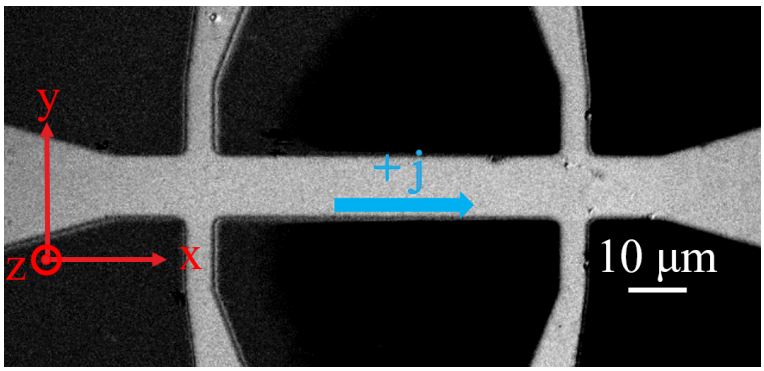

Figure 7.2 | (a) Differential MOKE image of a Pt/Co/AlO_x Hall bar patterned on SiN_x. The magnetization is first set down by applying B_z = - 46 mT, then the reference image is taken at $B_z = 0$. After applying B_z = + 46 mT to let the magnetization up, this differential image is obtained at $B_z = 0$. The coordinate of the system, direction of current, and the scale bar are indicated.

III [see Fig. 7.1(a)].

7.3.1 Overoxidized Pt/Co/AlO_x

As the remanence of the overoxidized sample in region I is less than 100 % [see black curve in Fig. 7.1(b)], the reference for differential MOKE measurements is taken at B_z = -5 mT, where the magnetization is saturated parallel to -z [Fig. 7.3(a)]. Upon increasing B_z to 0, we observe that several bubble domains of diameter 0.4-1 μm nucleate in different parts of the Hall bar. Bubble domains nucleate at defects $B_z = 0$ because of the weak B_K^{eff}. Increasing the field from 0 to +0.4 mT [Fig. 7.3(a)] results in further nucleation of bubble domains as well as bubble growth into labyrinthine stripe domains. The procedure for nucleating the bubbles is different from that used in previous studies, which started from a striped domain pattern rather than a uniformly magnetized state[59,60,62,66,114,115,168,169]. In previous studies, the bubbles are stabilized by shrinking the stripe domains with magnetization opposite to the applied field, resulting in bubbles with core magnetization antiparallel to the field. Here, the bubbles are nucleated starting from a saturated state and the core magnetization is parallel to the field. At B_z = +0.4 mT, we also observe that, due to the larger bubble density, neighbouring bubbles merge and form irregular-shaped domains. However, due to the limited spatial resolution of the MOKE, which is about 0.35 μm, we cannot conclude whether the magnetic domains of the merged bubbles are indeed fully merged or small gaps below the resolution are still present.

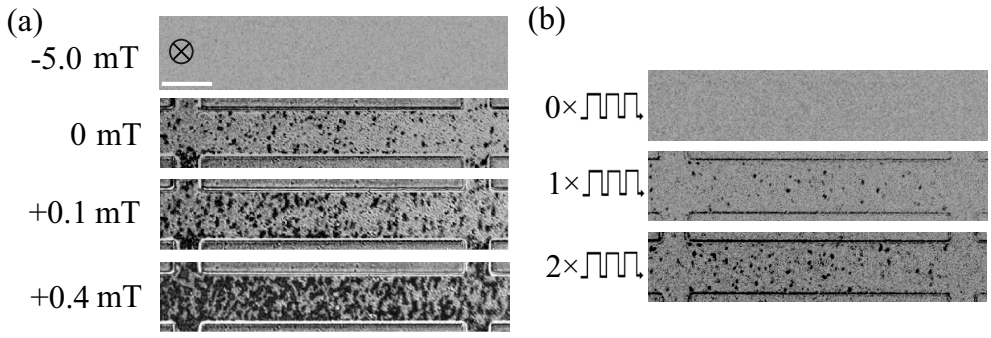

Figure 7.3 | Domain nucleation and growth in the "overoxidized" sample (region I) when the reversal occurs by (a) sweeping B_z, and (b) injecting multiple current pulses at $B_z = 0$. The current density for (b) is 2.2×10^{11} A/m^2 with width 10 μs and 1 kHz frequency. The numbers here indicate one series of 5000 pulses. The scale bar is 10 μm.

In order to study the current-induced nucleation, we take a reference image at $B_z = 0$ [Fig. 7.3(b)], in which a few bubble domains are already present and inject 2 series (each series includes 5000 pulses) of positive pulses along the x direction with density $j_x = +2.2\times10^{11}$ A/m^2, width 10 μs, and 1 kHz frequency. We find that the application of current pulses results in the nucleation and growth of bubble domains, similar to what is observed during the field reversal [Fig. 7.3(a)]. Similar results are obtained for a sequence of negative current pulses, indicating that the nucleation of domains is independent on the polarity of the current. Therefore, we may conclude that the nucleation is mainly due to Joule heating[156,170], although the effects of SOTs cannot be excluded. This sample is supposed to have strong disorder due to inhomogeneous oxidation, leading to a broad distribution of M_s, B_K^{eff}, DMI and SOT parameters.

7.3.2 Optimized Pt/Co/AlO$_x$

As the "optimized" Pt/Co/AlO$_x$ samples in region II have 100 % remanence, we take the background image at $B_z = 0$, and then increase B_z to +13 mT, where the magnetization reversal takes place [Fig 7.4(a)]. We find that large magnetic domains nucleate and propagate from one side of the Hall bar to the other [Fig 7.4(a)], with the domain wall pinning at defect sites [marked by circles in Fig 7.4(a)]. The motion of the DW at constant magnetic field [bottom image in Fig 7.4(a)] is an indication of DW motion in creep regime[100]. The absence of bubbles may be explained by the large B_K^{eff} in region II, where the relative weak DMI cannot support the formation of skyrmionic textures. Moreover, compared

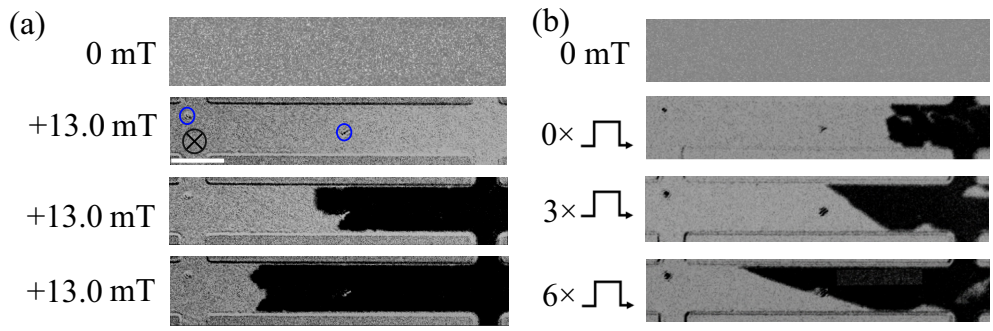

Figure 7.4 | Domain growth in "optimized" Pt/Co/AlO_x (region II) when the reversal occurs by (a) sweeping the out-of-plane magnetic field and (b) injecting single current pulses as indicated at $B_z = 0$. Circles indicate the position of two defects that result in contrast changes in the MOKE images unrelated to the magnetic changes. The current density for (b) is 9.0×10^{11} A/m^2 with width 100 ns. The scale bar is 10 μm.

with the "overoxidized" sample, due to the reduced oxidation, pinning and disorder are reduced here, therefore a single DW can be more easily driven by the field.

To investigate the current-induced domain propagation, we take the reference image at $B_z = 0$, nucleate a domain by applying $B_z = +13$ mT, then sweep back B_z to zero and start recording the MOKE images after current injection [upper image in Fig 7.4(b)]. We first inject three single pulses with j_x = -9.0×10^{11} A/m^2 and width 100 ns. We find that domain propagates to the left, parallel to the current direction. Moreover, the domain wall is a straight line, tilted with respect to the Hall bar [middle image in Fig 7.4(b)]. The domain wall is further pushed to the left and the tilt is enhanced upon injection of three more single pulses [lower image in Fig 7.4(b)].

This current-induced domain wall propagation is consistent with recent studies[95,105,107,171–173]. As mentioned in chapter 2.3.4, SOTs can drive the Néel domain walls in Pt/Co/AlO_x against electron flow with a tilt that is determined by both DMI and SOTs. The DW magnetization is distorted during the application of a current pulse, as T^{DL} rotates the DW moments away from the x direction towards the y direction. As the DMI tends to maintain a Néel type DW, the total energy of the system is reduced by tilting the DW relative to the current direction[105]. The tilt angle is determined by the energy balance between DMI, DW surface energy, and magnetostatic interactions.

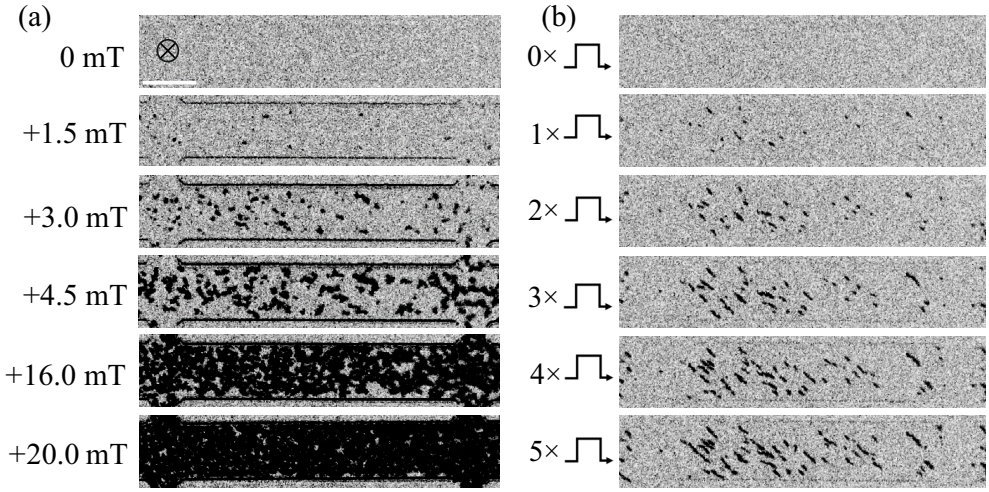

Figure 7.5 | Domain nucleation and propagation in "underoxidized" Pt/Co/ AlO_x (region III). (a) Out-of-plane magnetic field reversal and (b) after injecting single current pulses as indicated at $B_z = 0$. The current density for (b) is $6.8{\times}10^{11}$ A/m^2, each pulse is 40 ns. The scale bar is 10 μm.

7.3.3 Underoxidized Pt/Co/AlO_x

For the "underoxidized" Pt/Co/AlO_x sample (region III), we take the reference MOKE image at $B_z = 0$ after fully saturating the magnetization down [Fig. 7.5(a)]. For the field-driven magnetization reversal, we find that bubble domains with diameter 0.4-0.6 μm nucleate at $B_z = +1.5$ mT. Increasing B_z leads to more bubble nucleation and growth of labyrinthine domains until the magnetization is almost fully saturated at +20 mT [Fig. 7.5(a)], in agreement with the hysteresis loop in Fig. 7.1(b). Repeating the process we observe that the bubbles nucleate always at the same position, indicating that nucleation occurs at defect sites.

As reported recently, skyrmions have been observed in many HM/FM heterostructures so far[58,61,63,64,67–69,71,73,115,174,175], particularly in Pt/Co/X heterostructures, where X is Ir, MgO and AlO_x[63,68,69,73,115]. The "underoxidized" Pt/Co/AlO_x samples studied here exhibit strong DMI due to Pt, and weak B_K^{eff} due to underoxidation. Thus, it is likely that left-handed Néel type skyrmion bubbles form in this region, as the DMI is larger than the critical value determined by B_K^{eff} (See Eq. 2.15)[58,97,99]. Therefore, we suggest that these bubbles are skyrmion bubbles and thus carry a nonzero topological charge.

Next, we study the current-induced nucleation and motion of the bubbles. We take the reference at $B_z = 0$ with initial magnetization down and inject five

positive single pulses with $j_x = +6.8\times10^{11}$ A/m^2 and width 40 ns [Fig. 7.5(b)]. Contrary to the overoxidized sample, current pulses lead not only to bubble nucleation but also to bubble growth along a well-defined direction with respect to the current. This motion is reminiscent of the skyrmion Hall effect reported in the literature[57,97] and will be analyzed in chapter 8.

Moreover, consistent with both simulations[61,75] and experimental observation in Pt/Co/Ir[69] and Pt/Co/MgO[73], the elongation here may be the result of strong pinning obstructing the bubble motion as analyzed further in chapter 8. Disorder can also induce a large dispersion of bubble size and shape[73,168,169], which is consistent with the high-resolution MFM results reported in the next chapter.

In chapter 8, we perform more current-induced measurements in order to verify the topology of the skyrmion bubbles and investigate their expansion. We report a detailed study of the current-induced bubble expansion, with the aim of indicating the effects of pinning and disorder on the evolution of the skyrmionic textures.

8 Current-induced expansion of skyrmion bubbles in the presence of strong pinning

In this chapter we investigate the current-driven growth of skyrmion bubbles in "underoxidized" Pt/Co/AlO_x in the presence of strong pinning using MOKE and high-resolution MFM. We show how the pinning influences the transverse deflection of the skyrmion bubbles and how this depends on current density, pulse width and out-of-plane field. We interpret the current-driven expansion of the skyrmion bubbles as the result of the combination of the bubble topology, asymmetric SOTs, and pinning, revealing that the skyrmion Hall effect in our system has both intrinsic and extrinsic origins. Lastly, we compare the final magnetization state reached by continuous pulsing with the fully saturated state obtained by applying an out-of-plane magnetic field, and discuss the possible origins of current-induced demagnetization.

8.1 Skyrmion Hall effect

In Chapter 7 we showed that, in "underoxidized" Pt/Co/AlO_x, current pulses result in the nucleation and directional expansion of skyrmion bubbles. As seen in Fig. 7.5(b), the bubbles expand by elongating in a direction oblique to the current. One side of the bubble, however, remains pinned, which prevents the displacement of the bubble. In the following, we investigate the relationship between the bubble magnetization, current direction, and deflection angle, and demonstrate that the latter originates from the topology of the bubbles.

For each experimental sequence, we begin by taking a reference MOKE image in a fully saturated state (up or down) at zero field and inject a sequence of current pulses of a given polarity (positive or negative), then take intermediate MOKE images to track the evolution of the system. An exemplary sequence of differential MOKE images is shown in [Fig. 8.1(a)], in which the four combinations of $\pm j_x$ and initial $\pm M_z$ state are presented.

The images reveal that the bubbles elongate along a certain angle, which depends on the polarity of the magnetization and current. The schematics in the middle of Fig. 8.1(a) illustrates the expansion direction. As described in Chapter 2, the skyrmion Hall effect[57,97,124] describes the deflection angle that a skyrmion bubble exhibits when moving along a racetrack due to its topology.

The skyrmion Hall angle is given by $\theta_{sk} \approx tan^{-1}(-\frac{4\Delta Q}{\alpha d})$ under the assumption that $d \gg \Delta$, where Δ is the domain wall width, Q is the topological charge, α is the damping, and d is the diameter of the skyrmion bubble. We find that the sign of the deflection angle in $Pt/Co/Al_x$ is consistent with the sign of θ_{sk} predicted above, considering Q and the sign of the current[71,124].

Although the skyrmion Hall effect has been widely studied so far, the expansion of the skyrmion bubbles in the strong pinning regime has not been investigated. In the following, we explore the emergence of the skyrmion Hall effect and the dependence of θ_{sk} as a function of different experimental conditions. At least four skyrmion bubbles with straight elongation are chosen for data averaging in order to reduce the influence of pinning, which can distort the expansion (more details in the next section) and make the measurement of θ_{sk} less precise.

The phase diagram of θ_{sk} as a function of j_x, and Q = $\pm$1 is shown in Fig. 8.1(b). The phase diagram is symmetric under inversion of Q and j_x. The experiments are performed at zero field and the pulse width is fixed to 40 ns. The bubbles do not start expanding until j_x reaches 10.6×10^{11} A/m^2, after which θ_{sk} increases with j_x monotonically, consistent with previous observations[69,71,73]. Theoretically, in the absence of pinning, θ_{sk} should be constant[71]. However, due to the presence of defects, the skyrmion bubble trajectory is modified, resulting in a lower θ_{sk}. Larger j_x results in an increase of θ_{sk} because the influence of pinning on the bubble expansion becomes weaker. By increasing the amplitude of the current pulses (larger SOTs), the flow regime is approached, where θ_{sk} reaches its theoretical value[69,71,100]. Note that we are unable to saturate θ_{sk} with j_x because at large current density ($j_x \geqslant 19.2\times10^{11}$ A/m^2), thermal effects start to dominate, resulting in random nucleation of bubbles rather than expansion. Here we conclude that the bubble expansion is dominated by pinning. Due to the symmetry of the skyrmion bubble expansion with j_x and Q [Fig. 8.1(b)], all the measurements in the following section were performed for Q = +1, $j_x > 0$.

Fig. 8.1(c) shows the dependence of θ_{sk} with pulse width at constant $j_x = 16.3\times10^{11}$ A/m^2. We find that -θ_{sk} increases almost linearly with pulse width. As the amplitude of SOTs is proportional to j_x and not to the pulse width[23], SOTs cannot be responsible for this behaviour.

Previous work on skyrmion shows that the skyrmion dynamics can be activated by thermal agitation, which helps skyrmions to overcome the pinning energy barrier[176–179]. For shorter pulses, a larger current amplitude is required to induce skyrmion motion, indicative of a thermally assisted depinning pro-

cess[71]. In addition, thermal fluctuations also affect the transverse motion of the skyrmions, leading to a different θ_{sk}[179]. Therefore, as Joule heat dissipation is linear with pulse width, the linear dependence between pulse width and θ_{sk} indicates that thermally activated depinning plays an important role in the bubble expansion. In order to verify this assumption, we lower the current density to j_x = 13.0×10^{11} A/m^2. In such a case, θ_{sk} has a weak dependence on pulse width [Fig. 8.1(c)], consistent with our assumption.

Next, we investigate the relationship between θ_{sk} and B_z [Fig. 8.1(d)]. As B_z increases from -4.3 mT to +6.3 mT, -θ_{sk} increases from about 27° to 52°. In principle, B_z can have different effects on the bubble behaviour. First, as B_z goes from negative to positive, a bubble with core magnetization pointing up is expected to expand [Fig. 7.5(a)]. However, as $\theta_{sk} \propto 1/d$ in the limit of $d \gg \Delta$ (Eq. 2.18), this effect would lead to a reduction of θ_{sk}, which is opposite to what we observe. Second, B_z may assist the depinning of the bubbles, leading to a faster bubble expansion and therefore to a larger deflection angle. This effect is similar to the transition from a creep regime at negative B_z to flow regime at positive B_z observed for DW motion in Pt/Co/Pt, which supports to the second hypothesis.

From the MOKE images, we can also evaluate the skyrmion bubble expansion velocity, which is defined as the average of the displacements of several bubbles after a single pulse divided by the pulse width. We characterize the skyrmion bubble expansion velocity as a function of both current density (40 ns pulse width) and pulse width (j_x = 16.3×10^{11} A/m^2) at zero field. Fig. 8.1(e) shows that the velocity increases with j_x, as expected. However, the velocity also increases monotonically with pulse width. This behaviour can be explained by the fact that when pulse width is small, the bubble expansion is dominated by pinning as thermal activation is weak. Increasing j_x and the pulse width results in higher speed as the pinning effect is less pronounced. The fact that both θ_{sk} and the velocity increase with pulse width, consistent with the hypothesis that θ_{sk} is limited by pinning[73]. The increase of velocity with pulse width also rules out inertial effects in the bubble expansion, which would artificially increase the velocity extracted from the displacement measurements at short pulse width. This observation is consistent with recent studies of DW dynamics in Pt/Co/AlO_x[80,180,181], where no inertial effects were observed, but contrary to W/CoFeB/MgO[182].

Let us finally comment on the magnitude of θ_{sk} estimated using Eq. 2.18 versus the one measured in the experiment. For the Pt/Co/AlO_x trilayer, we take

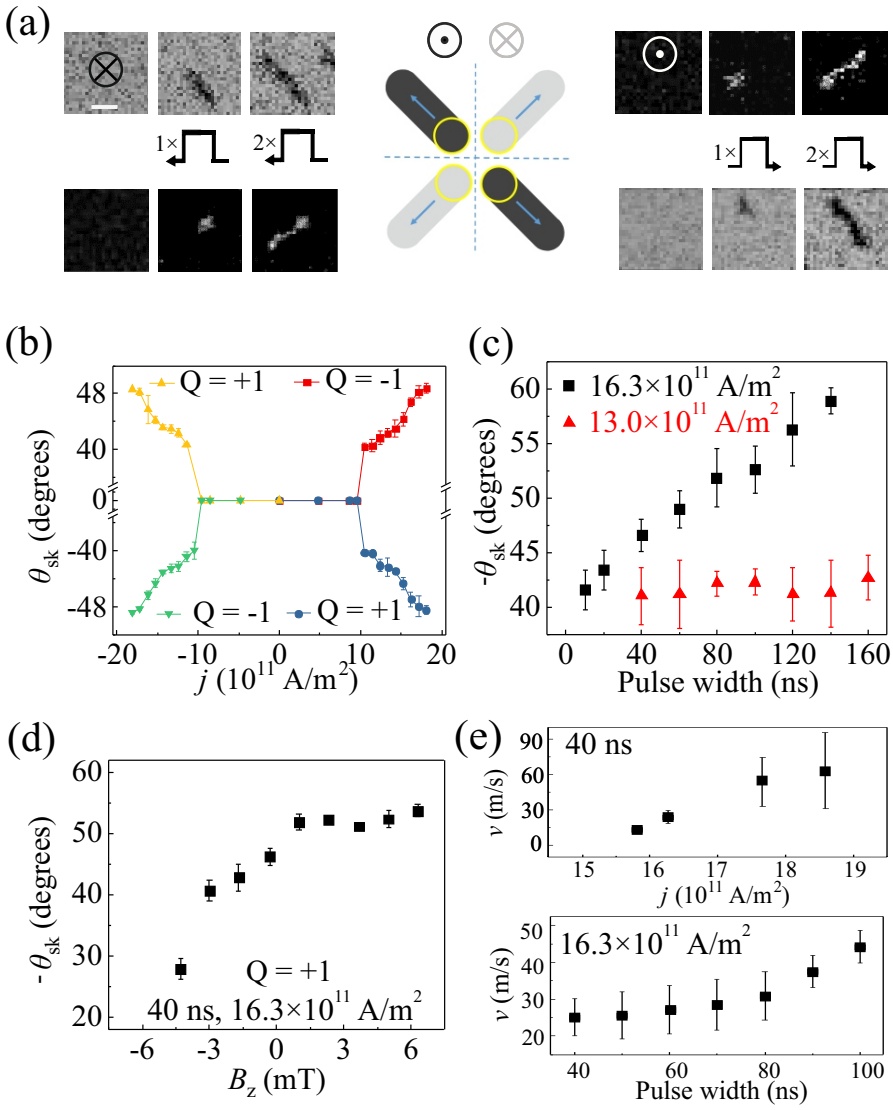

Figure 8.1 | (a) Wide field polar MOKE images and schematics showing the nucleation and expansion of the skyrmion bubbles in "underoxidized" Pt/Co/AlO_x (see chapter 7) for different polarities of the magnetization and current. The dark contrast indicates that the magnetization points up, the light grey contrast indicates that the magnetization points down, and the scale bar is 1 μm. (b) Phase diagram of the skyrmion Hall angle θ_{sk} as a function of current density j_x and bubble topology at zero magnetic field. The current pulse width is 40 ns. (c) θ_{sk} as a function of pulse width at zero magnetic field. Measurements with current density 16.3 and 13.0×10^{11} A/m^2 are given in black and red colors, respectively. (d) θ_{sk} as a function of out-of-plane field B_z. $B_z > 0$ indicates that the field points up. Note that the inner magnetization of the skyrmion bubbles here is up (Q = +1). (e) Bubble expansion velocity as a function of current density (pulse width fixed at 40 ns) and pulse width (j_x = 16.3×10^{11} A/m^2). The measurements are performed at zero magnetic field. Vertical error bars represent the standard deviation of the average of different skyrmion bubbles in the same sample.

$\Delta = 16$ nm (estimated from Eq. 2.13 with $B_K^{eff} = 100$ mT and exchange stiffness $J = 15$ pJ/m)[16] and $d = 350$ nm (from MFM measurement). Taking $\alpha \sim 0.39$[73], we estimate $\theta_{sk} \approx 25°$, which is smaller than the largest $\theta_{sk} \approx 60°$ observed in Fig. 8.1(c). In order to match the experimental and theoretical θ_{sk}, we should have either $\alpha \sim 0.1$ or $\Delta = 59$ nm, which is unlikely. Therefore, we infer that, in addition to the intrinsic skyrmion Hall effect described by Eq. 2.18, there is an additional extrinsic contribution to θ_{sk}. As reported recently, pinning and disorder may give rise to an extrinsic skyrmion Hall effect[168,169,183] because they can be viewed as a force acting opposite to the ideal skyrmion motion direction. The gyrotropic response to this force leads to a transverse displacement opposite to that due to the intrinsic skyrmion Hall effect. This effect explains the reduction of θ_{sk} at low j_x, as the pinning force in comparable to the force due to the current. However, it cannot explain the large values of θ_{sk} observed at large j_x, which are above the intrinsic skyrmion Hall angle in the flow regime. Therefore, there should be an additional extrinsic skyrmion Hall effect which leads to the large θ_{sk} observed in our experiment. We suppose that this extrinsic origin might be the asymmetric SOTs, which is discussed in the next section.

8.2 Anisotropic expansion of skyrmion bubbles

In order to increase the resolution of our measurements, we asked Yaoxuan Feng from Prof. Hans J. Hug's group in EMPA to perform high resolution MFM measurements in order to resolve the local texture of the skyrmion bubbles. In these measurements, we initialize the magnetization so that it points down, then perform MFM at zero field and room temperature. Without injecting pulses, we find that skyrmion bubbles nucleate at zero field with a diameter $d \approx 350$ nm [first image of Fig. 8.2(a)]. Note that the remanence of the sample for the MFM measurement is $\approx 97\%$. Then we inject two positive current pulses (40ns and $j_x = 16.3 \times 10^{11}$ A/m^2) and find that the skyrmion bubbles elongate along the current direction with a transverse velocity, which is consistent with the MOKE measurements shown in Fig. 8.1(a). Surprisingly, after reversing the current polarity two times, we observe that the skyrmion bubbles always elongate with the back end pinned, which is determined by the current polarity and independent of $Q = \pm 1$. The three ellipses and the differential MFM images in Fig. 8.2(a) highlight the elongation path with different current polarities. Note that a few bubbles break into small bubbles, which we attribute to the result of SOTs and pinning effects, or to the stray field of the MFM tip. Fig. 8.2(b)

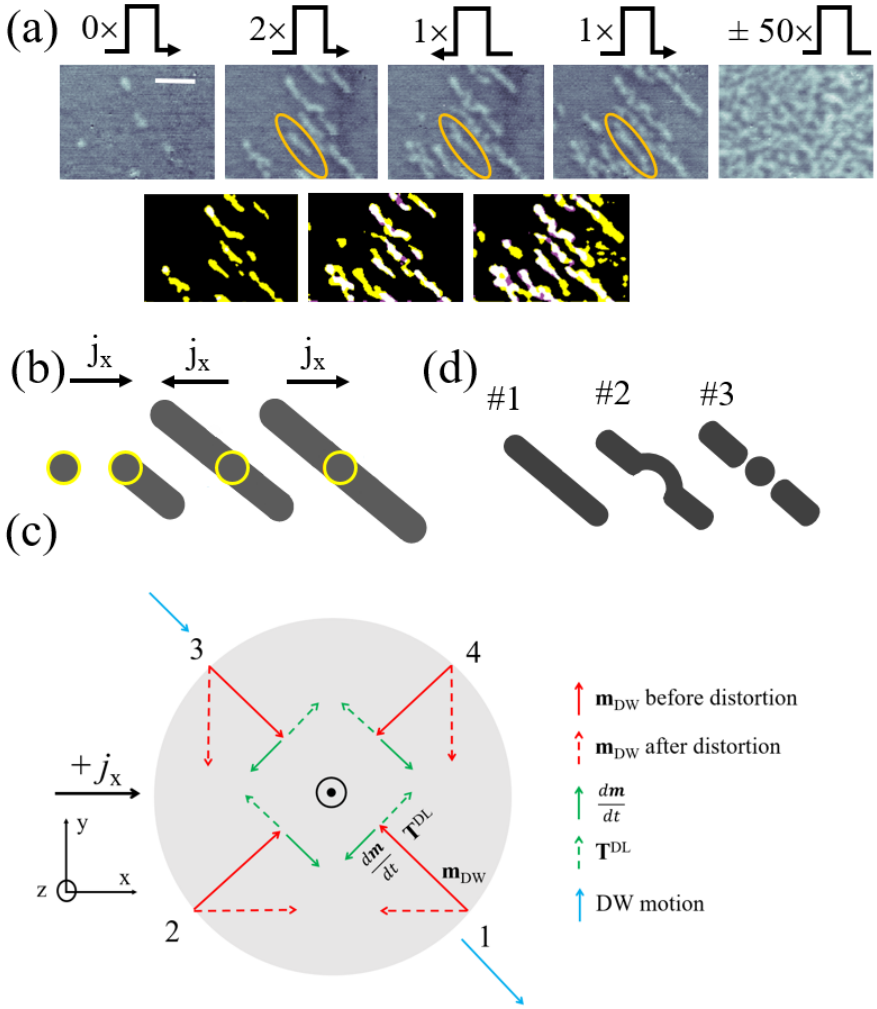

Figure 8.2 | (a) High resolution MFM images of skyrmion bubbles. The magnetization of the sample is initialized by applying a field B_z = -46 mT. A sequence of 40 ns long pulses is injected with $j_x = 16.3\times10^{11}$ A/m^2, before taking the MFM images. Arrows indicate the direction of the current, ± 50 indicates 50 positive and negative pulses applied at a frequency of 10 Hz. The orange ellipses highlight the dynamics of the skyrmion bubbles after switching the current polarity. The bottom three images are the differential MFM images of the upper two consecutive MFM images. The white color shows the original domains, the yellow color indicates the bubble expansion, the purple color indicates back switching. The scale bar is 2 μm. (b) Schematic of the expansion of a pinned skyrmion bubbles induced by current pulses with different polarity. The yellow circle indicates the original skyrmion bubble. (c) Schematic of the asymmetric torques at different positions of the bubble edge. The green solid (dashed) arrow indicates $d\mathbf{m}/dt$ ($\mathbf{T}^{DL}$), the red solid (dashed) arrow indicates the DW magnetization before (after distortion), the blue arrow indicates the DW motion direction. (d) Schematic of the three different configurations of the elongated skyrmionic textures.

shows a schematic representation of the same process. We now set a qualitative model that explains the asymmetric expansion of the bubbles, namely, a positive extrinsic contribution to θ_{sk}.

In the 3D coordinate, as $\mathbf{m} = (\mathbf{m}_x, \mathbf{m}_y, \mathbf{m}_z)$, we can write $\mathbf{T}^{DL}$ as follows:

$$\mathbf{T}^{DL} = T^{DL}\mathbf{m} \times (\mathbf{m} \times \mathbf{y}) = T^{DL}(m_x m_y, -m_x^2 - m_z^2, m_y m_z). \tag{8.1}$$

Suppose in a skyrmion bubble with up core magnetization Q = +1 [Fig. 8.2(c)], the initial DW magnetization $\mathbf{m}_{\mathrm{DW}}$ at sites 1 to 4 has $m_x = m_y \neq 0$ and $m_z < m$ due to DMI. The Landau-Lifshitz-Gilbert equation can be written in a simplified form as $d\mathbf{m}/dt \propto -\mathbf{T}^{DL} - \mathbf{m} \times \mathbf{T}^{DL}$ considering only the effect of $\mathbf{T}^{DL}$ [105] and $T^{DL} < 0$ in Pt/Co/AlO_x. Hence, at site 1, $\mathbf{T}^{DL}$ rotates $\mathbf{m}_{\mathrm{DW}}$ anticlockwise, leading to a new equilibrium with $|m_x| > |m_y|$ and $m_x < 0$. At site 2, $\mathbf{T}^{DL}$ rotates $\mathbf{m}_{\mathrm{DW}}$ clockwise, leading to $|m_x| > |m_y|$ and $m_x > 0$. At sites 3 and 4, on the other hand, $\mathbf{T}^{DL}$ results in a decrease of $|m_x|$ relative to the equilibrium situation. Therefore, the largest torques occur at sites 1 and 2 where the new $\mathbf{m}_{\mathrm{DW}}$ is (anti)parallel to $\mathrm{j_x}$, as here m_{x} is maximum, which leads to the highest DW propagation velocity ($v_{\mathrm{DW}} \propto m_{\mathrm{x}}$) [105,106,184]. On the contrary, the sites 3 and 4 possess the lowest velocity. Therefore, without defect and disorder, after injecting current pulses, these asymmetric torques distort the skyrmion bubble into an ellipse and drive it along a tilted path (blue arrows). As the driving force ($\mathbf{T}^{DL}$) at the top half of the bubble are smaller than at the bottom half, it is natural that the top half bubble is blocked by the strong pinning, while the bottom half can depin, leading to the observed asymmetric bubble expansion. Upon reversing the current polarity, the sign of the torques changes, leading to bubbles that are pinned at the bottom half and expand from the top.

We also notice that for Q=+1, $j_{\mathrm{x}} > 0$, by increasing j_{x}, stronger torques shift the sites with maximum (minimum) velocity to the top (bottom), thus, a higher θ_{sk} is obtained. Therefore, we confirm that θ_{sk} can be influenced by asymmetric SOTs, demonstrating the previous assumption of the extrinsic skyrmion Hall effect. Thus, we conclude that in our strongly pinned Pt/Co/AlO_x sample, both intrinsic and extrinsic skyrmion Hall effects contribute to the high θ_{sk}.

From the high resolution MFM images, we can distinguish three different expansion "modes" of the skyrmion bubbles, whose schematics are shown in Fig. 8.2(d). The first one is the straight elongation in which the bubbles grow with a cosntant deflection angle without disturbance. The second is a distorted elongation, which is probably due to the presence of local disorder, such as sites

with strong anisotropy. In this situation, skyrmion bubbles change their original growth route to avoid the regions of high DW energy, thus, deviating from a straight path[169]. Once the bubbles circumvent these regions, skyrmion bubbles continue to elongate with the same θ_{sk}. The third case is the fragmentation of an elongated bubble into small bubbles. A possible explanation for the fragmentation is the competition between strong pinning and SOT, with both quantities depending locally on disorder.

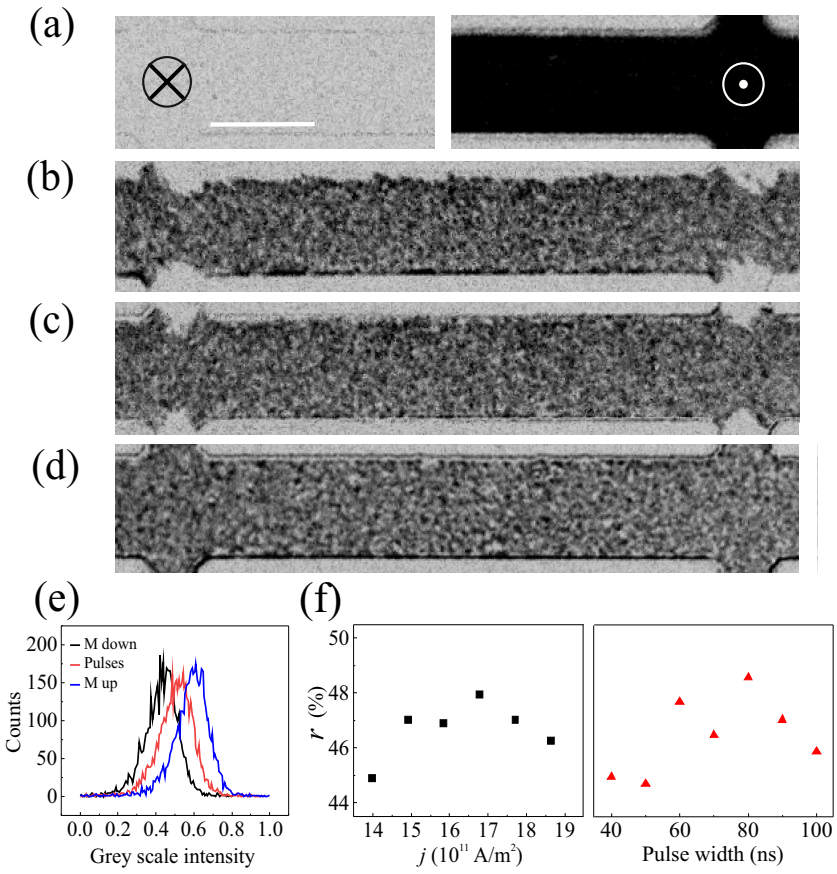

Figure 8.3 | (a) MOKE image of the field-saturated states with magnetization down (left) and up (right) obtained by applying $B_z = \pm 46$ mT. The scale bar is 10 μm. (b) MOKE image of the current-nucleated state after applying continuous positive pulses (x direction). (c) MOKE image of the current-nucleated state after applying continuous negative pulses (-x direction) in the presence of a 30 mT in-plane magnetic field (x direction). (d) MOKE image of the demagnetized state by cycling B_z with amplitude approaching to zero. (e) Grey scale intensity distribution of the magnetization in different states. (f) Grey scale ratio of the pulse-nucleated states as a function of current density and pulse width. In (b) and (c), 100 pulses with $j_x = 16.3 \times 10^{11}$ A/m^2, 40 ns width and 10 Hz were injected.

8.3 Observation of a topologically demagnetized state

As the skyrmionic textures keep on growing regardless of the current polarity, we inject continuous pulses with both polarity to investigate the final state after current injection [last image of Fig. 8.2(a)]. From the MFM images, We deduce that this is a demagnetized state compared to the one saturated by magnetic field. In order to further understand this current-nucleated state, we perform more MOKE measurements as described below.

We performed MOKE measurements on a sample initially saturated down and subject to about 50 positive current pulses followed by an equal number of negative current pulses. The pulses are applied at a frequency of 10 Hz, are each 40 ns long, and have $j_x = 16.3\times10^{11}$ A/m^2. Compared with the fully saturated state by a magnetic field [Fig. 8.3(a)], the current-nucleated state presents both grey and black contrast, consistent with the MFM measurements. Then we initialize the magnetization down by applying B_z = -46 mT, and inject -j_x in the presence of an in-plane B_x = +30 mT to assist the switching process (see chapter 6). Note that this field is the largest in-plane field that we can apply in the MOKE setup. Surprisingly, this state [Fig. 8.3(c)] shows the same contrast as Fig. 8.3(b), indicating that, even with a relative strong in-plane field, the magnetization cannot be fully switched by the current, unlike the optimized Pt/Co/AlO$_x$ sample (Fig. 7.4).

Indeed, we find that the contrast of Fig. 8.3(b) and (c) is similar to that obtained after demagnetization by repetitive cycling of B_z with amplitude approaching to zero [Fig. 8.3(d)]. In order to prove this point in a more quantitative way, we plot the grey scale intensity of the field-induced up and down saturated states and compare it with that of the current-nucleated state [Fig.8.3(e)]. We use the following equation to calculate the current-induced switching ratio:

$$r = \frac{I_j - I_{down}}{I_{up} - I_{down}} \tag{8.2}$$

Here I_j, I_{down}, I_{up} are the mean grey scale intensity of the pulse-nucleated, field-induced magnetization down and up states, respectively. We plot r as a function of j_x and pulse width, and find that $r \approx 47\%$ in both cases, close to 50%, demonstrating that the sample is indeed close to a fully demagnetized state.

A possible explanation is that current-induced heating leads to nucleation of more bubbles until the demagnetized state is reached. Another possibility, not necessarily alternative to the first, is that the skyrmion bubbles cannot merge

into a single domain because the energy barrier to annihilate the bubble DW in the confined volume between bubbles is too large. This effect can be see as an effective topological barrier that prevents the unwinding of the chiral DW around the bubbles, thus hindering the formation of a uniform domain magnetized in the direction determined by j_{x} and B_{x}. Evidently, a strong B_{z} can destroy the topology by changing the skyrmionic textures into a single domain, whereas the current and B_{x} are not strong enough to change the topology of the textures.

9 Summary and outlook

9.1 Summary

In this thesis, I have investigated the effects of oxidation on the magnetic properties, spin-orbit torques, and skyrmionic textures in ultrathin $Pt/Co/AlO_x$ heterostructures.

In the first part, I studied the oxidation effects on the resistivity, magnetization, magnetic anisotropy, anomalous Hall resistance, and SOTs of $Pt/Co/AlO_x$, $Pt/CoO_x/Co/AlO_x$, and $PtO_x/Co/AlO_x$ heterostructures. In all samples, increasing levels of oxidation lead to a reduction of M_s due to the formation of CoO_x. On the contrary, R_{AHE} decreases with increasing oxidation in $Pt/Co/AlO_x$ but increases in $Pt/CoO_x/Co/AlO_x$ and $PtO_x/Co/AlO_x$, consistently with the AHE being influenced by the magnetic volume as well as by spin-dependent scattering at oxidized interfaces.

The magnetic anisotropy is determined by the competition between the PMA of the Pt/Co and Co/Al interfaces and shape anisotropy. The latter scales as M_s and is strongly influenced by the oxidation of Co. In $Pt/Co/AlO_x$, B_K^{eff} decreases linearly with increasing t_{Al}, from 1.76 T to 0.36 T going from over-oxidized to under-oxidized Co/Al interfaces. Interestingly, the insertion of a thin CoO_x layer between Pt and Co results in very strong PMA of the $Pt/CoO_x/Co/AlO_x$ series, with $B_K^{eff} \approx 1.7$ T, which is nearly independent on t_{CoO}. Direct oxidation of Pt, on the other hand, leads to a reduction of the PMA in $PtO_x/Co/AlO_x$ compared to $Pt/Co/AlO_x$.

The amplitude of the damping-like and field-like SOTs varies substantially depending on the oxidation profile, reflecting changes of M_s and SOT efficiency. For $Pt/Co/AlO_x$, we find that ξ_j^{DL} and ξ_j^{FL} peak at 0.14 and 0.07, respectively, upon optimal oxidation of the Co/Al interface, which corresponds to a maximum of M_s and minimum oxidation of Co, as confirmed by XPS. The insertion of a 2 Å thick paramagnetic CoO_x layer between Pt and Co nearly doubles ξ_j^{DL} and ξ_j^{FL}, indicating that the overall spin conversion efficiency of $Pt/CoO_x/Co/AlO_x$ is significantly higher than $Pt/Co/AlO_x$. Both ξ_j^{DL} and ξ_j^{FL} decrease with increasing t_{CoO_x}, but appear to level off around 0.15 and 0.12, respectively, for $t_{CoO_x} > 4$ Å. This trend suggests that, not only the CoO_x layer enhances the transmission of the spin current generated by the Pt layer and Pt/CoO_x interface[151–154], but also that the CoO_x/Co interface generates an additional spin

accumulation that is independent of t_{CoO_x}.

The oxidation of the Pt layer leads to significant oxygen diffusion upon deposition of Co and Al, as confirmed by XPS and this is rationalized by the larger enthalpy of formation of Al_2O_3 and CoO relative to PtO. The inhomogeneous oxidation profile of the $PtO_x/Co/AlO_x$ series prevents a clear cut determination of ξ_j^{DL} and ξ_j^{FL}, which remain, in any case, significantly smaller than reported for $PtO_x/Ni_{81}Fe_{19}/SiO_2$ [46,47]. Additionally, the SOT efficiencies normalized by the electric field are found to decrease continuously with increasing O_2 ratio. These results are in stark contrast with the SOT efficiency reported in Refs. 46, 47, which shows a monotonic increase with increasing concentration of O_2. Possible explanations for such a discrepancy are discussed in chapter 6.

Comparing the SOT efficiency in these three systems, we conclude that insertion of the ultrathin paramagnetic CoO_x layer between Pt and Co can heavily enhance the SOTs of the system, meaning the charge to spin current conversion is strongly improved.

Finally, we demonstrated that the critical current density required to switch the magnetization of the Co layer scales linearly with the theoretical current density calculated using the macrospin approximation, but is smaller by about one order of magnitude. The critical current density of $Pt/Co/AlO_x$ is also found to depend linearly on B_K^{eff}, which is determined by the degree of oxidation of the Co/Al interface.

In the second part, I investigated how the domain textures of $Pt/Co/AlO_x$ are systematically influenced by oxidation effects. The overoxidized, optimized and underoxidized $Pt/Co/AlO_x$ show distinct domain nucleation and growth by magnetic field and current-induced SOTs. Due to the weak B_K^{eff} and strong DMI, skyrmion bubbles form in underoxidized $Pt/Co/AlO_x$ by applying moderate out-of-plane fields or current pulses. We find that the strong pinning and disorder heavily influence the nucleation and expansion of the skyrmion bubbles. We investigate the skyrmion Hall effect as a function of current density, pulse width and out-of-plane field, and show that it strongly depends on the different regimes of the skyrmion dynamics. Moreover, by reversing the current polarity, we find that skyrmion bubbles expand with the back end pinned due to the asymmetric SOTs and strong pinning. This study reveals that the skyrmion Hall effect in $Pt/Co/AlO_x$ has both extrinsic and intrinsic contributions. The extrinsic contribution has two components: one that reduces θ_{sk} due to disorder in the creep regime and one that increases θ_{sk} due to the asymmetry in the flow regime. Lastly, we show that repeated current pulsing of underoxidized

$Pt/Co/AlO_x$ leads to a topological demagnetized state rather than to a fully saturated magnetic state.

These results demonstrate the critical impact of interfacial oxidation on the SOT and magnetotransport properties of HM/FM/Ox trilayers. Taken together with recent studies[36–43,45,153,154], this work shows that devices with strongly improved PMA and charge-to-spin conversion efficiency might be realized by careful control of the oxidation of the top and bottom interfaces of the FM layer. Finally, these results shed light on the oxidation effects on the domain textures as well as the current-induced skyrmion expansion in the presence of strong pinning in ultrathin heterostructures.

9.2 Outlook

In most studies of $HM/FM/O_x$ and $HMO_x/FM/O_x$ systems, oxygen is supposed to remain localized at it interfaces or be uniformly distributed inside a given layer. However, as seen in chapter 3, this is far from being the case. Oxygen migration can give rise to uniform oxidation gradients as well as to inhomogeneous oxidized regions within a single layer, for example at grain boundaries. In-depth correlation of the sample microstructure and oxygen concentration are required in order to shed light on this issue. Such studies could be performed, e.g., by atom probe tomography, which allows to map the three-dimensional distribution of elemental species in a small sample volume.

A very interesting result is the enhancement of the SOT efficiency obtained upon insertion of a 2 Å thick CoO_x layer between Pt and Co. Here an interesting question is whether other binary antiferromagnets such as NiO, Cr_2O_3, and MnF_2 would have similar or perhaps even larger effects. Is it important to match the magnetic elements in the antiferromagnetic and ferromagnetic layers? How relevant are the thickness and Néel temperature for oxide and metallic antiferromagnets? Answering these questions requires extensive growth and characterization studies.

A related point is to distinguish effects due to the transmission of a spin current by fluctuating antiferromagnetically coupled spins from spin-dependent scattering due to interfacial oxidation. To this end, besides using metallic antiferromagnets, one may insert different spacer layers between the antiferromagnet and the ferromagnet, such as a light metal or a nonmagnetic oxide, and study the SOT efficiency as a function of spacer thickness.

Concerning the skyrmion motion, this work suggests that topology, anisotropic

domain wall velocity, and disorder contribute in different amounts to the skyrmion Hall effect. Disentangling these three contributions is not simple, mainly because disorder is poorly characterized. In this case, performing micromagnetic simulations starting from known distributions of the relevant magnetic parameters should shed light on the relative importance of the extrinsic and intrinsic contributions.

Bibliography

1. M. Julliere, "Tunneling between ferromagnetic films," *Phys. Lett. A*, vol. 54, no. 3, pp. 225 – 226, 1975.

2. P. Grünberg, R. Schreiber, Y. Pang, M. B. Brodsky, and H. Sowers, "Layered magnetic structures: Evidence for antiferromagnetic coupling of fe layers across cr interlayers," *Phys. Rev. Lett.*, vol. 57, pp. 2442–2445, Nov 1986.

3. G. Binasch, P. Grünberg, F. Saurenbach, and W. Zinn, "Enhanced magnetoresistance in layered magnetic structures with antiferromagnetic interlayer exchange," *Phys. Rev. B*, vol. 39, pp. 4828–4830, Mar 1989.

4. M. N. Baibich, J. M. Broto, A. Fert, F. N. Van Dau, F. Petroff, P. Etienne, G. Creuzet, A. Friederich, and J. Chazelas, "Giant Magnetoresistance of (001)Fe/(001)Cr Magnetic Superlattices," *Phys. Rev. Lett.*, vol. 61, pp. 2472–2475, Nov 1988.

5. S. A. Wolf, D. D. Awschalom, R. A. Buhrman, J. M. Daughton, S. von Molnár, M. L. Roukes, A. Y. Chtchelkanova, and D. M. Treger, "Spintronics: A spin-based electronics vision for the future," *Science*, vol. 294, no. 5546, pp. 1488–1495, 2001.

6. I. Žutić, J. Fabian, and S. Das Sarma, "Spintronics: Fundamentals and applications," *Rev. Mod. Phys.*, vol. 76, pp. 323–410, Apr 2004.

7. A. Manchon, I. Miron, T. Jungwirth, J. Sinova, J. Zelezný, A. Thiaville, K. Garello, and P. Gambardella, "in press, Current-induced spin-orbit torques in ferromagnetic and antiferromagnetic systems," *Rev. Mod. Phys.*, 2019.

8. Images are from Dr. Manuel Baumgartner.

9. S. Ikeda, K. Miura, H. Yamamoto, K. Mizunuma, H. D. Gan, M. Endo, S. Kanai, J. Hayakawa, F. Matsukura, and H. Ohno, "A perpendicular-anisotropy CoFeB – MgO magnetic tunnel junction," *Nat. Mater.*, vol. 9, no. 9, pp. 721–4, 2010.

10. M. D. Stiles and A. Zangwill, "Anatomy of spin-transfer torque," *Phys. Rev. B*, vol. 66, no. 1, p. 014407, 2002.

11. L. Berger, "Emission of spin waves by a magnetic multilayer traversed by a current," *Phys. Rev. B*, vol. 54, no. 13, pp. 9353–9358, 1996.

12. J. C. Slonczewski, "Conductance and exchange coupling of two ferromagnets separated by a tunneling barrier," *Phys. Rev. B*, vol. 39, no. 10, pp. 6995–7002, 1989.

13. J. C. Slonczewski, "Current-driven excitation of magnetic multilayers," *J. Magn. Magn. Mater.*, vol. 159, no. 1, pp. L1–L7, 1996.

14. A. D. Kent and D. C. Worledge, "A new spin on magnetic memories," *Nat. Nanotech.*, vol. 10, no. 3, pp. 187–91, 2015.

15. K. Garello, F. Yasin, S. Couet, L. Souriau, J. Swerts, S. Rao, S. Van Beek, W. Kim, E. Liu, S. Kundu, D. Tsvetanova, K. Croes, N. Jossart, E. Grimaldi, M. Baumgartner, D. Crotti, A. Fumémont, P. Gambardella, and G. S. Kar, "SOT-MRAM 300mm integration for low power and ultrafast embedded memories," in *2018 IEEE Symposium on VLSI Circuits*, pp. 81–82, June 2018.

16. I. M. Miron, T. Moore, H. Szambolics, L. D. Buda-Prejbeanu, S. Auffret, B. Rodmacq, S. Pizzini, J. Vogel, M. Bonfim, A. Schuhl, and G. Gaudin, "Fast current-induced domain-wall motion controlled by the rashba effect," *Nat. Mater.*, vol. 10, p. 419, May 2011.

17. I. M. Miron, K. Garello, G. Gaudin, P. J. Zermatten, M. V. Costache, S. Auffret, S. Bandiera, B. Rodmacq, A. Schuhl, and P. Gambardella, "Perpendicular switching of a single ferromagnetic layer induced by in-plane current injection," *Nature*, vol. 476, no. 7359, pp. 189–93, 2011.

18. I. M. Miron, G. Gaudin, S. Auffret, B. Rodmacq, A. Schuhl, S. Pizzini, J. Vogel, and P. Gambardella, "Current-driven spin torque induced by the rashba effect in a ferromagnetic metal layer," *Nat. Mater.*, vol. 9, no. 3, pp. 230–4, 2010.

19. L. Liu, C.-F. Pai, Y. Li, H. W. Tseng, D. C. Ralph, and R. A. Buhrman, "Spin-torque switching with the giant spin hall effect of tantalum," *Science*, vol. 336, no. 6081, pp. 555–558, 2012.

20. J. Kim, J. Sinha, M. Hayashi, M. Yamanouchi, S. Fukami, T. Suzuki, S. Mitani, and H. Ohno, "Layer thickness dependence of the current-induced ef-

fective field vector in Ta|CoFeB|MgO," *Nat. Mater.*, vol. 12, no. 3, pp. 240–5, 2013.

21. M. Cubukcu, O. Boulle, M. Drouard, K. Garello, C. Onur Avci, I. Mihai Miron, J. Langer, B. Ocker, P. Gambardella, and G. Gaudin, "Spin-orbit torque magnetization switching of a three-terminal perpendicular magnetic tunnel junction," *Appl. Phys. Lett.*, vol. 104, no. 4, p. 042406, 2014.

22. W. Zhao, Y. Zhang, T. Devolder, J. O. Klein, D. Ravelosona, C. Chappert, and P. Mazoyer, "Failure and reliability analysis of STT – MRAM," *Microelectron. Reliab.*, vol. 52, no. 9, pp. 1848 – 1852, 2012.

23. K. Garello, I. M. Miron, C. O. Avci, F. Freimuth, Y. Mokrousov, S. Blugel, S. Auffret, O. Boulle, G. Gaudin, and P. Gambardella, "Symmetry and magnitude of spin-orbit torques in ferromagnetic heterostructures," *Nat. Nanotech.*, vol. 8, no. 8, pp. 587–93, 2013.

24. J. Sinova, S. O. Valenzuela, J. Wunderlich, C. Back, and T. Jungwirth, "Spin hall effects," *Rev. Mod. Phys.*, vol. 87, no. 4, pp. 1213–1260, 2015.

25. R. Winkler, *Spin-Orbit Coupling Effects in Two-Dimensional Electron and Hole Systems*, book section Origin of Spin Orbit Coupling Effect, pp. 61–67. Springer, Berlin, Heidelberg, 2003.

26. Y. A. Bychkov and E. I. Rashba, "Properties of a 2D electron gas with lifted spectral degeneracy," *JETP Lett.*, vol. 39, no. 78, p. 66, 1984.

27. C.-F. Pai, L. Liu, Y. Li, H. W. Tseng, D. C. Ralph, and R. A. Buhrman, "Spin transfer torque devices utilizing the giant spin hall effect of tungsten," *Appl. Phys. Lett.*, vol. 101, no. 12, p. 122404, 2012.

28. X. Fan, H. Celik, J. Wu, C. Ni, K. Lee, V. O. Lorenz, and J. Q. Xiao, "Quantifying interface and bulk contributions to spin–orbit torque in magnetic bilayers," *Nat. Commun.*, vol. 5, p. 3042, 2014.

29. S. Monso, B. Rodmacq, S. Auffret, G. Casali, F. Fettar, B. Gilles, B. Dieny, and P. Boyer, "Crossover from in-plane to perpendicular anisotropy in Pt/CoFe/AlOx sandwiches as a function of al oxidation: A very accurate control of the oxidation of tunnel barriers," *Appl. Phys. Lett.*, vol. 80, no. 22, pp. 4157–4159, 2002.

30. A. Manchon, S. Pizzini, J. Vogel, V. Uhlîr, L. Lombard, C. Ducruet, S. Auffret, B. Rodmacq, B. Dieny, M. Hochstrasser, and G. Panaccione, "X-ray analysis of the magnetic influence of oxygen in Pt/Co/AlOx trilayers," *J. Appl. Phys.*, vol. 103, no. 7, p. 07A912, 2008.

31. A. Manchon, S. Pizzini, J. Vogel, V. Uhlíř, L. Lombard, C. Ducruet, S. Auffret, B. Rodmacq, B. amnd Dieny, M. Hochstrasser, and G. Panaccione, "X-ray analysis of oxygen-induced perpendicular magnetic anisotropy in Pt/Co/AlOx trilayers," *J. Magn. Magn. Mater.*, vol. 320, no. 13, pp. 1889 – 1892, 2008.

32. A. Manchon, C. Ducruet, L. Lombard, S. Auffret, B. Rodmacq, B. Dieny, S. Pizzini, J. Vogel, V. Uhlíř, M. Hochstrasser, and G. Panaccione, "Analysis of oxygen induced anisotropy crossover in trilayers Pt/Co/MO_x," *J. Appl. Phys.*, vol. 104, no. 4, p. 043914, 2008.

33. B. Rodmacq, A. Manchon, C. Ducruet, S. Auffret, and B. Dieny, "Influence of thermal annealing on the perpendicular magnetic anisotropy of Pt/Co/AlOx trilayers," *Phys. Rev. B*, vol. 79, p. 024423, Jan 2009.

34. H. Garad, L. Ortega, A. Y. Ramos, Y. Joly, F. Fettar, S. Auffret, B. Rodmacq, B. Diény, O. Proux, and A. I. Erko, "Competition between CoOx and CoPt phases in Pt/Co/AlOx semi tunnel junctions," *J. Appl. Phys.*, vol. 114, no. 5, p. 053508, 2013.

35. D. Chiba, S. Fukami, K. Shimamura, N. Ishiwata, K. Kobayashi, and T. Ono, "Electrical control of the ferromagnetic phase transition in cobalt at room temperature," *Nat. Mater.*, vol. 10, p. 853, Oct. 2011.

36. G. Yu, P. Upadhyaya, Y. Fan, J. G. Alzate, W. Jiang, K. L. Wong, S. Takei, S. A. Bender, L. T. Chang, Y. Jiang, M. Lang, J. Tang, Y. Wang, Y. Tserkovnyak, P. K. Amiri, and K. L. Wang, "Switching of perpendicular magnetization by spin-orbit torques in the absence of external magnetic fields," *Nat. Nanotech.*, vol. 9, no. 7, pp. 548–54, 2014.

37. G. Yu, L.-T. Chang, M. Akyol, P. Upadhyaya, C. He, X. Li, K. L. Wong, P. K. Amiri, and K. L. Wang, "Current-driven perpendicular magnetization switching in Ta/CoFeB/[TaO_x or MgO/TaO_x] films with lateral structural asymmetry," *Appl. Phys. Lett.*, vol. 105, no. 10, p. 102411, 2014.

38. U. Bauer, L. Yao, A. J. Tan, P. Agrawal, S. Emori, H. L. Tuller, S. van Dijken, and G. S. D. Beach, "Magneto-ionic control of interfacial magnetism," *Nat. Mater.*, vol. 14, p. 174, Nov. 2014.

39. S. Emori, U. Bauer, S. Woo, and G. S. D. Beach, "Large voltage-induced modification of spin-orbit torques in Pt/Co/GdOx," *Appl. Phys. Lett.*, vol. 105, no. 22, p. 222401, 2014.

40. C. Bi, Y. Liu, T. Newhouse-Illige, M. Xu, M. Rosales, J. W. Freeland, O. Mryasov, S. Zhang, S. G. E. te Velthuis, and W. G. Wang, "Reversible control of Co magnetism by voltage-induced oxidation," *Phys. Rev. Lett.*, vol. 113, p. 267202, Dec 2014.

41. C.-F. Pai, Y. Ou, L. H. Vilela-Leão, D. C. Ralph, and R. A. Buhrman, "Dependence of the efficiency of spin hall torque on the transparency of Pt/ferromagnetic layer interfaces," *Phys. Rev. B*, vol. 92, p. 064426, Aug 2015.

42. M. Akyol, J. G. Alzate, G. Yu, P. Upadhyaya, K. L. Wong, A. Ekicibil, P. Khalili Amiri, and K. L. Wang, "Effect of the oxide layer on current-induced spin-orbit torques in Hf|CoFeB|MgO and Hf|CoFeB|TaOx structures," *Appl. Phys. Lett.*, vol. 106, no. 3, p. 032406, 2015.

43. X. Qiu, K. Narayanapillai, Y. Wu, P. Deorani, D.-H. Yang, W.-S. Noh, J.-H. Park, K.-J. Lee, H.-W. Lee, and H. Yang, "Spin-orbit-torque engineering via oxygen manipulation," *Nat. Nanotech.*, vol. 10, p. 333, Mar. 2015.

44. K.-U. Demasius, T. Phung, W. Zhang, B. P. Hughes, S.-H. Yang, A. Kellock, W. Han, A. Pushp, and S. S. P. Parkin, "Enhanced spin-orbit torques by oxygen incorporation in tungsten films," *Nat. Commun.*, vol. 7, p. 10644, Feb. 2016.

45. Y. Hibino, T. Hirai, K. Hasegawa, T. Koyama, and D. Chiba, "Enhancement of the spin-orbit torque in a Pt/Co system with a naturally oxidized Co layer," *Appl. Phys. Lett.*, vol. 111, no. 13, p. 132404, 2017.

46. H. An, T. Ohno, Y. Kanno, Y. Kageyama, Y. Monnai, H. Maki, J. Shi, and K. Ando, "Current-induced magnetization switching using an electrically insulating spin-torque generator," *Sci. Adv.*, vol. 4, no. 2, p. eaar2250, 2018.

47. H. An, Y. Kanno, A. Asami, and K. Ando, "Giant spin-torque generation by heavily oxidized Pt," *Phys. Rev. B*, vol. 98, p. 014401, Jul 2018.

48. T. Srivastava, M. Schott, R. Juge, V. Křižáková, M. Belmeguenai, Y. Roussigné, A. Bernand-Mantel, L. Ranno, S. Pizzini, S.-M. Chérif, A. Stashkevich, S. Auffret, O. Boulle, G. Gaudin, M. Chshiev, C. Baraduc, and H. Béa, "Large-voltage tuning of dzyaloshinskii–moriya interactions: A route toward dynamic control of skyrmion chirality," *Nano Lett.*, vol. 18, no. 8, pp. 4871–4877, 2018.

49. D. d. S. Chaves, F. Ajejas, V. Křižáková, J. Vogel, and S. Pizzini, "Oxidation dependence of the Dzyaloshinskii-Moriya interaction in Pt/Co/Mo_x trilayers (m = Al or Gd)," *Phys. Rev. B*, vol. 99, p. 144404, Apr 2019.

50. T. H. R. Skyrme, "A non-linear theory of strong interactions," *Proceedings of the Royal Society of London. Series A, Mathematical and Physical Sciences*, vol. 247, no. 1249, pp. 260–278, 1958.

51. A. Fert, V. Cros, and J. Sampaio, "Skyrmions on the track," *Nat. Nanotech.*, vol. 8, p. 152, Mar. 2013.

52. S. S. P. Parkin, M. Hayashi, and L. Thomas, "Magnetic domain-wall racetrack memory," *Science*, vol. 320, no. 5873, pp. 190–194, 2008.

53. S. Zhang, A. A. Baker, S. Komineas, and T. Hesjedal, "Topological computation based on direct magnetic logic communication," *Sci. Rep.*, vol. 5, p. 15773, Oct. 2015.

54. G. Yu, P. Upadhyaya, Q. Shao, H. Wu, G. Yin, X. Li, C. He, W. Jiang, X. Han, P. K. Amiri, and K. L. Wang, "Room-temperature skyrmion shift device for memory application," *Nano Lett.*, vol. 17, no. 1, pp. 261–268, 2017. PMID: 27966987.

55. N. S. Kiselev, A. N. Bogdanov, R. Schäfer, and U. K. Rößler, "Chiral skyrmions in thin magnetic films: new objects for magnetic storage technologies?," *J. Phys. D*, vol. 44, p. 392001, sep 2011.

56. A. Hubert and R. Schäfer, *Magnetic Domains*. Springer, Berlin, Heidelberg, 1998.

57. K. Litzius, I. Lemesh, B. Krüger, P. Bassirian, L. Caretta, K. Richter, F. Büttner, K. Sato, O. A. Tretiakov, J. Förster, R. M. Reeve, M. Weigand, I. Bykova, H. Stoll, G. Schütz, G. S. D. Beach, and M. Kläui, "Skyrmion Hall effect revealed by direct time-resolved X-ray microscopy," *Nat. Phys.*, vol. 13, p. 170, Dec. 2016.

58. O. Boulle, J. Vogel, H. Yang, S. Pizzini, D. de Souza Chaves, A. Locatelli, T. O. Menteş, A. Sala, L. D. Buda-Prejbeanu, O. Klein, M. Belmeguenai, Y. Roussigné, A. Stashkevich, S. M. Chérif, L. Aballe, M. Foerster, M. Chshiev, S. Auffret, I. M. Miron, and G. Gaudin, "Room-temperature chiral magnetic skyrmions in ultrathin magnetic nanostructures," *Nat. Nanotech.*, vol. 11, p. 449, Jan. 2016.

59. C. Moreau-Luchaire, "Additive interfacial chiral interaction in multilayers for stabilization of small individual skyrmions at room temperature," *Nat. Nanotech.*, vol. 11, p. 444, Jan. 2016.

60. S. Woo, K. Litzius, B. Krüger, M.-Y. Im, L. Caretta, K. Richter, M. Mann, A. Krone, R. M. Reeve, M. Weigand, P. Agrawal, I. Lemesh, M.-A. Mawass, P. Fischer, M. Kläui, and G. S. D. Beach, "Observation of room-temperature magnetic skyrmions and their current-driven dynamics in ultrathin metallic ferromagnets," *Nat. Mater.*, vol. 15, p. 501, Feb. 2016.

61. F. Büttner, I. Lemesh, M. Schneider, B. Pfau, C. M. Günther, P. Hessing, J. Geilhufe, L. Caretta, D. Engel, B. Krüger, J. Viefhaus, S. Eisebitt, and G. S. D. Beach, "Field-free deterministic ultrafast creation of magnetic skyrmions by spin-orbit torques," *Nat. Nanotech.*, vol. 12, p. 1040, Oct. 2017.

62. A. Hrabec, J. Sampaio, M. Belmeguenai, I. Gross, R. Weil, S. M. Chérif, A. Stashkevich, V. Jacques, A. Thiaville, and S. Rohart, "Current-induced skyrmion generation and dynamics in symmetric bilayers," *Nat. Commun.*, vol. 8, p. 15765, June 2017.

63. M. A. Marioni, M. Penedo, M. Baćani, J. Schwenk, and H. J. Hug, "Halbach effect at the nanoscale from chiral spin textures," *Nano Lett.*, vol. 18, no. 4, pp. 2263–2267, 2018. PMID: 29543463.

64. D. Maccariello, W. Legrand, N. Reyren, K. Garcia, K. Bouzehouane, S. Collin, V. Cros, and A. Fert, "Electrical detection of single magnetic skyrmions in metallic multilayers at room temperature," *Nat. Nanotech.*, vol. 13, pp. 233–237, Mar. 2018.

65. Y. Dovzhenko, F. Casola, S. Schlotter, T. X. Zhou, F. Büttner, R. L. Walsworth, G. S. D. Beach, and A. Yacoby, "Magnetostatic twists in room-temperature skyrmions explored by nitrogen-vacancy center spin texture reconstruction," *Nat. Commun.*, vol. 9, p. 2712, July 2018.

66. S. Woo, K. M. Song, X. Zhang, M. Ezawa, Y. Zhou, X. Liu, M. Weigand, S. Finizio, J. Raabe, M.-C. Park, K.-Y. Lee, J. W. Choi, B.-C. Min, H. C. Koo, and J. Chang, "Deterministic creation and deletion of a single magnetic skyrmion observed by direct time-resolved X-ray microscopy," *Nat. Electron.*, vol. 1, pp. 288–296, May 2018.

67. W. Jiang, P. Upadhyaya, W. Zhang, G. Yu, M. B. Jungfleisch, F. Y. Fradin, J. E. Pearson, Y. Tserkovnyak, K. L. Wang, O. Heinonen, S. G. E. te Velthuis, and A. Hoffmann, "Blowing magnetic skyrmion bubbles," *Science*, vol. 349, no. 6245, pp. 283–286, 2015.

68. M. Schott, A. Bernand-Mantel, L. Ranno, S. Pizzini, J. Vogel, H. Béa, C. Baraduc, S. Auffret, G. Gaudin, and D. Givord, "The skyrmion switch: Turning magnetic skyrmion bubbles on and off with an electric field," *Nano Lett.*, vol. 17, no. 5, pp. 3006–3012, 2017. PMID: 28437086.

69. W. Legrand, D. Maccariello, N. Reyren, K. Garcia, C. Moutafis, C. Moreau-Luchaire, S. Collin, K. Bouzehouane, V. Cros, and A. Fert, "Room-temperature current-induced generation and motion of sub-100 nm skyrmions," *Nano Lett.*, vol. 17, no. 4, pp. 2703–2712, 2017. PMID: 28358984.

70. X. Zhang, Y. Zhou, and M. Ezawa, "Magnetic bilayer-skyrmions without skyrmion hall effect," *Nat. Commun.*, vol. 7, p. 10293, Jan. 2016.

71. W. Jiang, X. Zhang, G. Yu, W. Zhang, X. Wang, M. Benjamin Jungfleisch, J. Pearson, X. Cheng, O. Heinonen, K. L. Wang, Y. Zhou, A. Hoffmann, and S. te Velthuis, "Direct observation of the skyrmion hall effect," *Nat. Phys.*, vol. 13, p. 162, Sept. 2016.

72. W. Legrand, D. Maccariello, F. Ajejas, S. Collin, A. Vecchiola, K. Bouzehouane, N. Reyren, V. Cros, and A. Fert, "Room-temperature stabilization of antiferromagnetic skyrmions in synthetic antiferromagnets," *Nat. Mater.*, Sept. 2019.

73. R. Juge, S.-G. Je, D. d. S. Chaves, L. D. Buda-Prejbeanu, J. Peña Garcia, J. Nath, I. M. Miron, K. G. Rana, L. Aballe, M. Foerster, F. Genuzio, T. O. Menteş, A. Locatelli, F. Maccherozzi, S. S. Dhesi, M. Belmeguenai, Y. Roussigné, S. Auffret, S. Pizzini, G. Gaudin, J. Vogel, and O. Boulle, "Current-driven skyrmion dynamics and drive-dependent skyrmion hall effect in an ultrathin film," *Phys. Rev. Applied*, vol. 12, p. 044007, Oct 2019.

74. I. Kezsmarki, S. Bordacs, P. Milde, E. Neuber, L. Eng, J. White, H. Ronnow, C. Dewhurst, M. Mochizuki, K. Yanai, H. Nakamura, D. Ehlers, V. Tsurkan, and A. Loidl, "Neel-type skyrmion lattice with confined orientation in the polar magnetic semiconductor GaV4S8," *Nat. Mater.*, vol. 14, p. 1116, Sept. 2015.

75. X. Xu, X.-L. Li, Y. G. Semenov, and K. W. Kim, "Creation and destruction of skyrmions via electrical modulation of local magnetic anisotropy in magnetic thin films," *Phys. Rev. Applied*, vol. 11, p. 024051, Feb 2019.

76. F. Keffer, "Moriya interaction and the problem of the spin arrangements in βMnS," *Phys. Rev.*, vol. 126, pp. 896–900, May 1962.

77. C.-F. Pai, M. Mann, A. J. Tan, and G. S. D. Beach, "Determination of spin torque efficiencies in heterostructures with perpendicular magnetic anisotropy," *Phys. Rev. B*, vol. 93, p. 144409, Apr 2016.

78. S. Emori, E. Martinez, K.-J. Lee, H.-W. Lee, U. Bauer, S.-M. Ahn, P. Agrawal, D. C. Bono, and G. S. D. Beach, "Spin hall torque magnetometry of dzyaloshinskii domain walls," *Phys. Rev. B*, vol. 90, p. 184427, Nov 2014.

79. H. Yang, A. Thiaville, S. Rohart, A. Fert, and M. Chshiev, "Anatomy of dzyaloshinskii-moriya interaction at Co/Pt interfaces," *Phys. Rev. Lett.*, vol. 115, p. 267210, Dec 2015.

80. M. Baumgartner, K. Garello, J. Mendil, C. O. Avci, E. Grimaldi, C. Murer, J. Feng, M. Gabureac, C. Stamm, Y. Acremann, S. Finizio, S. Wintz, J. Raabe, and P. Gambardella, "Spatially and time-resolved magnetization dynamics driven by spin-orbit torques," *Nat. Nanotech.*, vol. 12, no. 10, pp. 980–986, 2017.

81. G. Chen, T. Ma, A. T. N'Diaye, H. Kwon, C. Won, Y. Wu, and A. K. Schmid, "Tailoring the chirality of magnetic domain walls by interface engineering," *Nat. Commun.*, vol. 4, p. 2671, Oct. 2013.

82. J. M. D. Coey, *Magnetism and Magnetic Materials*. Cambridge University Press, 2010.

83. S. Blundell, *Magnetism in condensed matter*. Oxford ; New York : Oxford University Press, 2001., 2001.

84. M. Dyakonov and V. Perel, "Current-induced spin orientation of electrons in semiconductors," *Phys. Lett. A*, vol. 35, no. 6, pp. 459 – 460, 1971.

85. J. E. Hirsch, "Spin Hall Effect," *Phys. Rev. Lett.*, vol. 83, pp. 1834–1837, Aug 1999.

86. A. Hoffmann, "Spin Hall effects in metals," *IEEE Trans. Magn.*, vol. 49, pp. 5172–5193, Oct 2013.

87. A. Manchon, "Spin–orbitronics: A new moment for berry," *Nat. Phys.*, vol. 10, no. 5, pp. 340–341, 2014.

88. V. Edelstein, "Spin polarization of conduction electrons induced by electric current in two-dimensional asymmetric electron systems," *Solid State Communications*, vol. 73, no. 3, pp. 233 – 235, 1990.

89. A. Bose, D. D. Lam, S. Bhuktare, S. Dutta, H. Singh, S. Miwa, and A. A. Tulapurkar, "Observation of anomalous spin-torque generated by a ferromagnet," *arXiv*, vol. preprint, p. arXiv:1706.07245, 2017.

90. C. O. Avci, K. Garello, M. Gabureac, A. Ghosh, A. Fuhrer, S. F. Alvarado, and P. Gambardella, "Interplay of spin-orbit torque and thermoelectric effects in ferromagnet/normal-metal bilayers," *Phys. Rev. B*, vol. 90, no. 22, p. 224427, 2014.

91. M. Hayashi, J. Kim, M. Yamanouchi, and H. Ohno, "Quantitative characterization of the spin-orbit torque using harmonic hall voltage measurements," *Phys. Rev. B*, vol. 89, p. 144425, Apr 2014.

92. C. Onur Avci, K. Garello, I. Mihai Miron, G. Gaudin, S. Auffret, O. Boulle, and P. Gambardella, "Magnetization switching of an MgO/Co/Pt layer by in-plane current injection," *Appl. Phys. Lett.*, vol. 100, no. 21, p. 212404, 2012.

93. M. Hayashi, L. Thomas, C. Rettner, R. Moriya, and S. S. P. Parkin, "Real time observation of the field driven periodic transformation of domain walls in permalloy nanowires at the larmor frequency and its first harmonic," *Appl. Phys. Lett.*, vol. 92, no. 11, p. 112510, 2008.

94. M. Baumgartner, *Time- and spatially-resolved magnetization dynamics induced by spin-orbit torques in thin film devices*. PhD thesis, ETH Zurich, 2018.

95. S. Emori, U. Bauer, S.-M. Ahn, E. Martinez, and G. S. D. Beach, "Current-driven dynamics of chiral ferromagnetic domain walls," *Nat. Mater.*, vol. 12, p. 611, June 2013.

96. C. O. Avci, E. Rosenberg, M. Baumgartner, L. Beran, A. Quindeau, P. Gambardella, C. A. Ross, and G. S. D. Beach, "Fast switching and signature of efficient domain wall motion driven by spin-orbit torques in a perpendicular anisotropy magnetic insulator/pt bilayer," *Appl. Phys. Lett.*, vol. 111, no. 7, p. 072406, 2017.

97. W. Jiang, G. Chen, K. Liu, J. Zang, S. G. te Velthuis, and A. Hoffmann, "Skyrmions in magnetic multilayers," *Phys. Rep.*, vol. 704, pp. 1 – 49, 2017. Skyrmions in Magnetic Multilayers.

98. A. Thiaville, S. Rohart, É. Jué, V. Cros, and A. Fert, "Dynamics of dzyaloshinskii domain walls in ultrathin magnetic films," *EPL (Europhysics Letters)*, vol. 100, p. 57002, dec 2012.

99. S. Rohart and A. Thiaville, "Skyrmion confinement in ultrathin film nanostructures in the presence of Dzyaloshinskii-Moriya interaction," *Phys. Rev. B*, vol. 88, p. 184422, Nov 2013.

100. P. J. Metaxas, J. P. Jamet, A. Mougin, M. Cormier, J. Ferré, V. Baltz, B. Rodmacq, B. Dieny, and R. L. Stamps, "Creep and flow regimes of magnetic domain-wall motion in ultrathin Pt/Co/Pt films with perpendicular anisotropy," *Phys. Rev. Lett.*, vol. 99, p. 217208, Nov 2007.

101. N. L. Schryer and L. R. Walker, "The motion of 180° domain walls in uniform dc magnetic fields," *J. Appl. Phys.*, vol. 45, no. 12, pp. 5406–5421, 1974.

102. S. Lemerle, J. Ferré, C. Chappert, V. Mathet, T. Giamarchi, and P. Le Doussal, "Domain wall creep in an ising ultrathin magnetic film," *Phys. Rev. Lett.*, vol. 80, pp. 849–852, Jan 1998.

103. J. Wesselinowa, T. Michael, S. Trimper, and K. Zabrocki, "Influence of layer defects on the damping in ferroelectric thin films," *Phys. Lett. A*, vol. 348, p. 397–404, Jan 2006.

104. W. Kleemann, J. Rhensius, O. Petracic, J. Ferré, J. P. Jamet, and H. Bernas, "Modes of periodic domain wall motion in ultrathin ferromagnetic layers," *Phys. Rev. Lett.*, vol. 99, p. 097203, Aug 2007.

105. M. Baumgartner and P. Gambardella, "Asymmetric velocity and tilt angle of domain walls induced by spin-orbit torques," *Appl. Phys. Lett.*, vol. 113, no. 24, p. 242402, 2018.

106. C. K. Safeer, E. Jué, A. Lopez, L. Buda-Prejbeanu, S. Auffret, S. Pizzini, O. Boulle, I. M. Miron, and G. Gaudin, "Spin-orbit torque magnetization switching controlled by geometry," *Nat. Nanotech.*, vol. 11, p. 143, Nov. 2015.

107. E. Martinez, O. Alejos, M. A. Hernandez, V. Raposo, L. Sanchez-Tejerina, and S. Moretti, "Angular dependence of current-driven chiral walls," *Appl. Phys. Express*, vol. 9, p. 063008, May 2016.

108. S. Mühlbauer, B. Binz, F. Jonietz, C. Pfleiderer, A. Rosch, A. Neubauer, R. Georgii, and P. Böni, "Skyrmion lattice in a chiral magnet," *Science*, vol. 323, no. 5916, pp. 915–919, 2009.

109. X. Z. Yu, Y. Onose, N. Kanazawa, J. H. Park, J. H. Han, Y. Matsui, N. Nagaosa, and Y. Tokura, "Real-space observation of a two-dimensional skyrmion crystal," *Nature*, vol. 465, p. 901, June 2010.

110. W. Münzer, A. Neubauer, T. Adams, S. Mühlbauer, C. Franz, F. Jonietz, R. Georgii, P. Böni, B. Pedersen, M. Schmidt, A. Rosch, and C. Pfleiderer, "Skyrmion lattice in the doped semiconductor $Fe_{1-x}Co_xSi$," *Phys. Rev. B*, vol. 81, p. 041203, Jan 2010.

111. S. X. Huang and C. L. Chien, "Extended skyrmion phase in epitaxial FeGe(111) thin films," *Phys. Rev. Lett.*, vol. 108, p. 267201, Jun 2012.

112. S. Heinze, K. von Bergmann, M. Menzel, J. Brede, A. Kubetzka, R. Wiesendanger, G. Bihlmayer, and S. Blügel, "Spontaneous atomic-scale magnetic skyrmion lattice in two dimensions," *Nat. Phys.*, vol. 7, p. 713, July 2011.

113. N. Romming, C. Hanneken, M. Menzel, J. E. Bickel, B. Wolter, K. von Bergmann, A. Kubetzka, and R. Wiesendanger, "Writing and deleting single magnetic skyrmions," *Science*, vol. 341, no. 6146, pp. 636–639, 2013.

114. G. Yu, A. Jenkins, X. Ma, S. A. Razavi, C. He, G. Yin, Q. Shao, Q. l. He, H. Wu, W. Li, W. Jiang, X. Han, X. Li, A. C. Bleszynski Jayich, P. K. Amiri, and K. L. Wang, "Room-temperature skyrmions in an antiferromagnet-based heterostructure," *Nano Lett.*, vol. 18, no. 2, pp. 980–986, 2018.

115. A. Soumyanarayanan, M. Raju, A. L. Gonzalez Oyarce, A. K. C. Tan, M.-Y. Im, A. Petrović, P. Ho, K. H. Khoo, M. Tran, C. K. Gan, F. Ernult, and C. Panagopoulos, "Tunable room-temperature magnetic skyrmions in Ir/Fe/Co/Pt multilayers," *Nat. Mater.*, vol. 16, p. 898, July 2017.

116. R. Tomasello, K. Y. Guslienko, M. Ricci, A. Giordano, J. Barker, M. Carpentieri, O. Chubykalo-Fesenko, and G. Finocchio, "Origin of temperature and field dependence of magnetic skyrmion size in ultrathin nanodots," *Phys. Rev. B*, vol. 97, p. 060402, Feb 2018.

117. Q. Shao, Y. Liu, G. Yu, S. K. Kim, X. Che, C. Tang, Q. L. He, Y. Tserkovnyak, J. Shi, and K. L. Wang, "Topological hall effect at above room temperature in heterostructures composed of a magnetic insulator and a heavy metal," *Nat. Electron.*, vol. 2, pp. 182–186, May 2019.

118. F. Büttner, I. Lemesh, and G. S. D. Beach, "Theory of isolated magnetic skyrmions: From fundamentals to room temperature applications," *Sci. Rep.*, vol. 8, p. 4464, Mar. 2018.

119. Y. Tu, "Determination of magnetization of micromagnetic wall in bubble domains by direct minimization," *J. Appl. Phys.*, vol. 42, no. 13, pp. 5704–5709, 1971.

120. W. J. DeBonte, "Properties of thick-walled cylindrical magnetic domains in uniaxial platelets," *J. Appl. Phys.*, vol. 44, no. 4, pp. 1793–1797, 1973.

121. W. Legrand, *Crafting magnetic skyrmions at room temperature : size, stability and dynamics in multilayers*. PhD thesis, Paris Saclay, 2019.

122. N. Nagaosa and Y. Tokura, "Topological properties and dynamics of magnetic skyrmions," *Nat. Nanotech.*, vol. 8, p. 899, Dec. 2013.

123. R. Tomasello, E. Martinez, R. Zivieri, L. Torres, M. Carpentieri, and G. Finocchio, "A strategy for the design of skyrmion racetrack memories," *Sci. Rep.*, vol. 4, p. 6784, Oct. 2014.

124. Y. Hirata, D.-H. Kim, S. K. Kim, D.-K. Lee, S.-H. Oh, D.-Y. Kim, T. Nishimura, T. Okuno, Y. Futakawa, H. Yoshikawa, A. Tsukamoto, Y. Tserkovnyak, Y. Shiota, T. Moriyama, S.-B. Choe, K.-J. Lee, and T. Ono, "Vanishing skyrmion hall effect at the angular momentum compensation temperature of a ferrimagnet," *Nat. Nanotech.*, vol. 14, pp. 232–236, Mar. 2019.

125. J. Müller and A. Rosch, "Capturing of a magnetic skyrmion with a hole," *Phys. Rev. B*, vol. 91, p. 054410, Feb 2015.

126. C. Reichhardt, D. Ray, and C. J. O. Reichhardt, "Collective transport properties of driven skyrmions with random disorder," *Phys. Rev. Lett.*, vol. 114, p. 217202, May 2015.

127. J. E. Greene, "Tracing the recorded history of thin-film sputter deposition: from the 1800s to 2017," *J. Vac. Sci. Technol. A*, vol. 35, no. 5, p. 05C204, 2017.

128. K. Seshan, ed. Oxford: William Andrew Publishing, third edition ed., 2012.

129. P. Kelly and R. Arnell, "Magnetron sputtering: a review of recent developments and applications," *Vacuum*, vol. 56, no. 3, pp. 159 – 172, 2000.

130. Y. Cao and C. Zhou, "Thickness dependence of surface roughness and magnetic properties of FeNiCr thin films," *J. Magn. Magn. Mater.*, vol. 333, pp. 1–7, 2013.

131. A. Dua, V. George, and R. Agarwala, "Characterization and microhardness measurement of electron-beam-evaporated alumina coatings," *Thin Solid Films*, vol. 165, no. 1, pp. 163 – 172, 1988.

132. Y. Nagano, "Standard enthalpy of formation of platinum hydrous oxide," *J. Therm. Anal. Calorim.*, vol. 69, pp. 831–839, Jul 2002.

133. D. D. Wagman, J. D. Cox, and V. A. Medvedev, *CODATA key values for thermodynamics*. Hemisphere Pub. Corp., 1989.

134. R. D. Holmes, H. S. O'Neill, and R. J. Arculus, "Standard gibbs free energy of formation for Cu_2O, NiO, CoO, and Fe_xO: High resolution electrochemical measurements using zirconia solid electrolytes from 900–1400 K," *Geochim. Cosmochim. Acta*, vol. 50, no. 11, pp. 2439 – 2452, 1986.

135. A. Ghosh, K. Garello, C. O. Avci, M. Gabureac, and P. Gambardella, "Interface-enhanced spin-orbit torques and current-induced magnetization switching of $Pd/Co/AlO_x$ layers," *Phys. Rev. Appl.*, vol. 7, no. 1, p. 014004, 2017.

136. M. H. Nguyen, D. C. Ralph, and R. A. Buhrman, "Spin torque study of the spin *h*all conductivity and spin diffusion length in platinum thin films with varying resistivity," *Phys. Rev. Lett.*, vol. 116, no. 12, p. 126601, 2016.

137. N. Nagaosa, J. Sinova, S. Onoda, A. H. MacDonald, and N. P. Ong, "Anomalous hall effect," *Rev. Mod. Phys.*, vol. 82, no. 2, pp. 1539–1592, 2010.

138. S. L. Zhang, J. Teng, J. Y. Zhang, Y. Liu, J. W. Li, G. H. Yu, and S. G. Wang, "Large enhancement of the anomalous Hall effect in Co/Pt multilayers sandwiched by MgO layers," *Appl. Phys. Lett.*, vol. 97, no. 22, p. 222504, 2010.

139. F. Zhang, F. S. Wen, Y. F. Lü, W. Li, Y. F. Lu, Z. Y. Liu, B. Xu, D. L. Yu, J. L. He, and Y. J. Tian, "Proper scaling of the anomalous hall effect in the Co/Pt multilayers," *J. Appl. Phys.*, vol. 110, no. 3, p. 033921, 2011.

140. X. Kou, J.-M. Schmalhorst, V. Keskin, and G. Reiss, "Magnetic anisotropy and anomalous hall effect of ultrathin Co/Pd bilayers," *J. Appl. Phys.*, vol. 112, no. 9, p. 093915, 2012.

141. S. L. Zhang, J. Teng, J. Y. Zhang, Y. Liu, J. W. Li, G. H. Yu, and S. G. Wang, "Large enhancement of the anomalous hall effect in Co/Pt multilayers sandwiched by MgO layers," *Appl. Phys. Lett.*, vol. 97, no. 22, p. 222504, 2010.

142. J. Y. Zhang, Z. L. Wu, S. G. Wang, C. J. Zhao, G. Yang, S. L. Zhang, Y. Liu, S. Liu, J. Teng, and G. H. Yu, "Effect of interfacial structures on anomalous hall behavior in perpendicular Co/Pt multilayers," *Appl. Phys. Lett.*, vol. 102, no. 10, p. 102404, 2013.

143. H. X. Yang, M. Chshiev, B. Dieny, J. H. Lee, A. Manchon, and K. H. Shin, "First-principles investigation of the very large perpendicular magnetic anisotropy at fe|mgo and co|mgo interfaces," *Phys. Rev. B*, vol. 84, p. 054401, Aug 2011.

144. W. S. Chung, S. M. Yang, T. W. Kim, and J. P. Hong, "Ultrathin Co-O oxide layer-driven perpendicular magnetic anisotropy in a CoO/[Co/Pd]m multilayer matrix upon annealing," *Sci. Rep.*, vol. 6, p. 37503, Nov. 2016.

145. C. Pan, H. An, T. Harumoto, Z. Zhang, Y. Nakamura, and J. Shi, "Control of the perpendicular magnetic anisotropy and perpendicular exchange bias in CoPt/CoOx thin films," *J. Magn. Magn. Mater.*, vol. 484, pp. 320 – 323, 2019.

146. V. P. Amin and M. D. Stiles, "Spin transport at interfaces with spin-orbit coupling: Phenomenology," *Phys. Rev. B*, vol. 94, p. 104420, Sep 2016.

147. V. P. Amin and M. D. Stiles, "Spin transport at interfaces with spin-orbit coupling: Formalism," *Phys. Rev. B*, vol. 94, p. 104419, Sep 2016.

148. V. P. Amin, J. Zemen, and M. D. Stiles, "Interface-generated spin currents," *Phys. Rev. Lett.*, vol. 121, p. 136805, Sep 2018.

149. F. Freimuth, S. Blügel, and Y. Mokrousov, "Spin-orbit torques in Co/Pt(111) and Mn/W(001) magnetic bilayers from first principles," *Phys. Rev. B*, vol. 90, p. 174423, Nov 2014.

150. T. Ambrose and C. L. Chien, "Dependence of exchange coupling on antiferromagnetic layer thickness in NiFe/CoO bilayers," *J. Appl. Phys.*, vol. 83, no. 11, pp. 6822–6824, 1998.

151. C. Hahn, G. de Loubens, V. V. Naletov, J. B. Youssef, O. Klein, and M. Viret, "Conduction of spin currents through insulating antiferromagnetic oxides," *Europhys. Lett.*, vol. 108, no. 5, p. 57005, 2014.

152. Z. Qiu, J. Li, D. Hou, E. Arenholz, A. T. N'Diaye, A. Tan, K.-i. Uchida, K. Sato, S. Okamoto, Y. Tserkovnyak, Z. Q. Qiu, and E. Saitoh, "Spin-current probe for phase transition in an insulator," *Nat. Commun.*, vol. 7, p. 12670, Aug. 2016.

153. K. Hasegawa, Y. Hibino, M. Suzuki, T. Koyama, and D. Chiba, "Enhancement of spin-orbit torque by inserting CoO_x layer into Co/Pt interface," *Phys. Rev. B*, vol. 98, p. 020405, Jul 2018.

154. H. Wang, J. Finley, P. Zhang, J. Han, J. T. Hou, and L. Liu, "Spin-orbit-torque switching mediated by an antiferromagnetic insulator," *Phys. Rev. Applied*, vol. 11, p. 044070, Apr 2019.

155. M. Harder, Y. Gui, and C.-M. Hu, "Electrical detection of magnetization dynamics via spin rectification effects," *Phys. Rep.*, vol. 661, pp. 1 – 59, 2016.

156. K. Garello, C. O. Avci, I. M. Miron, M. Baumgartner, A. Ghosh, S. Auffret, O. Boulle, G. Gaudin, and P. Gambardella, "Ultrafast magnetization switching by spin-orbit torques," *Appl. Phys. Lett.*, vol. 105, no. 21, p. 212402, 2014.

157. C. Zhang, M. Yamanouchi, H. Sato, S. Fukami, S. Ikeda, F. Matsukura, and H. Ohno, "Magnetization reversal induced by in-plane current in Ta/CoFeB/MgO structures with perpendicular magnetic easy axis," *J. Appl. Phys.*, vol. 115, no. 17, p. 17C714, 2014.

158. J.-C. Rojas-Sánchez, P. Laczkowski, J. Sampaio, S. Collin, K. Bouzehouane, N. Reyren, H. Jaffrès, A. Mougin, and J.-M. George, "Perpendicular magnetization reversal in Pt/[Co/Ni]3/Al multilayers via the spin hall effect of Pt," *Appl. Phys. Lett.*, vol. 108, no. 8, p. 082406, 2016.

159. T. Taniguchi, S. Mitani, and M. Hayashi, "Critical current destabilizing perpendicular magnetization by the spin hall effect," *Phys. Rev. B*, vol. 92, p. 024428, Jul 2015.

160. K.-S. Lee, S.-W. Lee, B.-C. Min, and K.-J. Lee, "Threshold current for switching of a perpendicular magnetic layer induced by spin Hall effect," *Appl. Phys. Lett.*, vol. 102, no. 11, p. 112410, 2013.

161. K.-S. Ryu, L. Thomas, S.-H. Yang, and S. Parkin, "Chiral spin torque at magnetic domain walls," *Nat. Nanotech.*, vol. 8, p. 527, June 2013.

162. O. J. Lee, L. Q. Liu, C. F. Pai, Y. Li, H. W. Tseng, P. G. Gowtham, J. P. Park, D. C. Ralph, and R. A. Buhrman, "Central role of domain wall depinning for perpendicular magnetization switching driven by spin torque from the spin hall effect," *Phys. Rev. B*, vol. 89, p. 024418, Jan 2014.

163. C. Zhang, S. Fukami, S. DuttaGupta, H. Sato, and H. Ohno, "Time and spatial evolution of spin–orbit torque-induced magnetization switching in W/CoFeB/MgO structures with various sizes," *J. Appl. Phys.*, vol. 57, p. 04FN02, feb 2018.

164. T. H. Pham, S.-G. Je, P. Vallobra, T. Fache, D. Lacour, G. Malinowski, M. C. Cyrille, G. Gaudin, O. Boulle, M. Hehn, J.-C. Rojas-Sánchez, and S. Mangin, "Thermal contribution to the spin-orbit torque in metallic-ferrimagnetic systems," *Phys. Rev. Applied*, vol. 9, p. 064032, Jun 2018.

165. N. Mikuszeit, O. Boulle, I. M. Miron, K. Garello, P. Gambardella, G. Gaudin, and L. D. Buda-Prejbeanu, "Spin-orbit torque driven chiral magnetization reversal in ultrathin nanostructures," *Phys. Rev. B*, vol. 92, p. 144424, Oct 2015.

166. M. A. Laguna-Marco, P. Kayser, J. A. Alonso, M. J. Martínez-Lope, M. van Veenendaal, Y. Choi, and D. Haskel, "Electronic structure, local magnetism, and spin-orbit effects of Ir(IV)-, Ir(V)-, and Ir(VI)- based compounds," *Phys. Rev. B*, vol. 91, p. 214433, Jun 2015.

167. S. Pizzini, J. Vogel, S. Rohart, L. D. Buda-Prejbeanu, E. Jué, O. Boulle, I. M. Miron, C. K. Safeer, S. Auffret, G. Gaudin, and A. Thiaville, "Chirality-induced asymmetric magnetic nucleation in $Pt/Co/AlO_x$ ultrathin microstructures," *Phys. Rev. Lett.*, vol. 113, p. 047203, Jul 2014.

168. I. Gross, W. Akhtar, A. Hrabec, J. Sampaio, L. J. Martínez, S. Chouaieb, B. J. Shields, P. Maletinsky, A. Thiaville, S. Rohart, and V. Jacques, "Skyrmion morphology in ultrathin magnetic films," *Phys. Rev. Materials*, vol. 2, p. 024406, Feb 2018.

169. R. Juge, S.-G. Je, D. de Souza Chaves, S. Pizzini, L. D. Buda-Prejbeanu, L. Aballe, M. Foerster, A. Locatelli, T. O. Menteş, A. Sala, F. Maccherozzi, S. S. Dhesi, S. Auffret, E. Gautier, G. Gaudin, J. Vogel, and O. Boulle, "Magnetic skyrmions in confined geometries: Effect of the magnetic field and the disorder," *J. Magn. Magn. Mater.*, vol. 455, pp. 3 – 8, 2018. Magnetic skyrmions as future information carriers.

170. K.-S. Lee, S.-W. Lee, B.-C. Min, and K.-J. Lee, "Thermally activated switching of perpendicular magnet by spin-orbit spin torque," *Appl. Phys. Lett.*, vol. 104, no. 7, p. 072413, 2014.

171. O. Boulle, S. Rohart, L. D. Buda-Prejbeanu, E. Jué, I. M. Miron, S. Pizzini, J. Vogel, G. Gaudin, and A. Thiaville, "Domain wall tilting in the presence of the Dzyaloshinskii-Moriya Interaction in out-of-plane magnetized magnetic nanotracks," *Phys. Rev. Lett.*, vol. 111, p. 217203, Nov 2013.

172. S. Emori, E. Martinez, K.-J. Lee, H.-W. Lee, U. Bauer, S.-M. Ahn, P. Agrawal, D. C. Bono, and G. S. D. Beach, "Spin hall torque magnetometry of dzyaloshinskii domain walls," *Phys. Rev. B*, vol. 90, p. 184427, Nov 2014.

173. C. Garg, A. Pushp, S.-H. Yang, T. Phung, B. P. Hughes, C. Rettner, and S. S. P. Parkin, "Highly asymmetric chiral domain-wall velocities in Y-shaped junctions," *Nano Lett.*, vol. 18, no. 3, pp. 1826–1830, 2018. PMID: 29420900.

174. K. Litzius, I. Lemesh, B. Krüger, P. Bassirian, L. Caretta, K. Richter, F. Büttner, K. Sato, O. A. Tretiakov, J. Förster, R. M. Reeve, M. Weigand, I. Bykova, H. Stoll, G. Schütz, G. S. D. Beach, and M. Kläui, "Skyrmion hall effect revealed by direct time-resolved X-ray microscopy," *Nat. Phys.*, vol. 13, p. 170, Dec. 2016.

175. J. Zázvorka, F. Jakobs, D. Heinze, N. Keil, S. Kromin, S. Jaiswal, K. Litzius, G. Jakob, P. Virnau, D. Pinna, K. Everschor-Sitte, L. Rózsa, A. Donges, U. Nowak, and M. Kläui, "Thermal skyrmion diffusion used in a reshuffler device," *Nat. Nanotech.*, vol. 14, pp. 658–661, July 2019.

176. L. Kong and J. Zang, "Dynamics of an insulating skyrmion under a temperature gradient," *Phys. Rev. Lett.*, vol. 111, p. 067203, Aug 2013.

177. S.-Z. Lin, C. Reichhardt, C. D. Batista, and A. Saxena, "Particle model for skyrmions in metallic chiral magnets: Dynamics, pinning, and creep," *Phys. Rev. B*, vol. 87, p. 214419, Jun 2013.

178. M. Mochizuki, X. Z. Yu, S. Seki, N. Kanazawa, W. Koshibae, J. Zang, M. Mostovoy, Y. Tokura, and N. Nagaosa, "Thermally driven ratchet motion of a skyrmion microcrystal and topological magnon hall effect," *Nat. Mater.*, vol. 13, p. 241, Jan. 2014.

179. R. E. Troncoso and A. S. Núñez, "Thermally assisted current-driven skyrmion motion," *Phys. Rev. B*, vol. 89, p. 224403, Jun 2014.

180. J. Vogel, M. Bonfim, N. Rougemaille, O. Boulle, I. M. Miron, S. Auffret, B. Rodmacq, G. Gaudin, J. C. Cezar, F. Sirotti, and S. Pizzini, "Direct observation of massless domain wall dynamics in nanostripes with perpendicular magnetic anisotropy," *Phys. Rev. Lett.*, vol. 108, p. 247202, Jun 2012.

181. T. Taniguchi, K.-J. Kim, T. Tono, T. Moriyama, Y. Nakatani, and T. Ono, "Precise control of magnetic domain wall displacement by a nanosecond current pulse in Co/Ni nanowires," *Appl. Phys. Express*, vol. 8, p. 073008, jul 2015.

182. J. Torrejon, E. Martinez, and M. Hayashi, "Tunable inertia of chiral magnetic domain walls," *Nat. Commun.*, vol. 7, p. 13533, Nov. 2016.

183. J.-V. Kim and M.-W. Yoo, "Current-driven skyrmion dynamics in disordered films," *Appl. Phys. Lett.*, vol. 110, no. 13, p. 132404, 2017.

184. E. Martinez, O. Alejos, M. A. Hernandez, V. Raposo, L. Sanchez-Tejerina, and S. Moretti, "Angular dependence of current-driven chiral walls," *Appl. Phys. Express*, vol. 9, p. 063008, May 2016.